NAVAL POSTGRADUATE SCHOOL
MONTEREY, CALIFORNIA

THESIS

AIRBORNE LASER MINE DETECTION SYSTEMS

by

Charles J. Cassidy

September, 1995

Thesis Advisor: R.C. Olsen

Approved for public release; distribution is unlimited.

19960403 001

REPORT DOCUMENTATION PAGE		Form Approved OMB No. 0704-0188

Public reporting burden for this collection of information is estimated to average 1 hour per response, including the time for reviewing instruction, searching existing data sources, gathering and maintaining the data needed, and completing and reviewing the collection of information. Send comments regarding this burden estimate or any other aspect of this collection of information, including suggestions for reducing this burden, to Washington Headquarters Services, Directorate for Information Operations and Reports, 1215 Jefferson Davis Highway, Suite 1204, Arlington, VA 22202-4302, and to the Office of Management and Budget, Paperwork Reduction Project (0704-0188) Washington DC 20503.

1. AGENCY USE ONLY *(Leave blank)*	2. REPORT DATE September, 1995	3. REPORT TYPE AND DATES COVERED Master's Thesis

4. TITLE AND SUBTITLE: AIRBORNE LASER MINE DETECTION SYSTEMS	5. FUNDING NUMBERS
6. AUTHOR(S) Cassidy, Charles J.	

7. PERFORMING ORGANIZATION NAME(S) AND ADDRESS(ES) Naval Postgraduate School Monterey CA 93943-5000	8. PERFORMING ORGANIZATION REPORT NUMBER

9. SPONSORING/MONITORING AGENCY NAME(S) AND ADDRESS(ES)	10. SPONSORING/MONITORING AGENCY REPORT NUMBER

11. SUPPLEMENTARY NOTES The views expressed in this thesis are those of the author and do not reflect the official policy or position of the Department of Defense or the U.S. Government.

12a. DISTRIBUTION/AVAILABILITY STATEMENT Approved for public release; distribution is unlimited.	12b. DISTRIBUTION CODE

13. ABSTRACT *(maximum 200 words)*

Mine detection has moved to the forefront as a concern for the United States Navy. The mine threat imposed by other nations has lead to the development and evaluation of relatively fast, efficient, and effective mine detection systems. Airborne laser radar has been suggested as a possible technique for minehunting. This paper analyzes data collected from two developmental systems. These systems were tested for the purpose of exploiting shallow water regions optically. These systems were Ocean Water Lidar (OWL), developed by NAWC, Warminster, Pennsylvania, and Magic Lantern Adaptation [ML(A)], developed by the Kaman Corporation, Bloomfield, Connecticut. The OWL system was analyzed by carefully examining each individual lidar scan from four separate system passes conducted off Eglin Air Force Base in September, 1994. Excellent bathymetry data was obtained, but the laser spot sizes used (one meter and twelve meters) precluded successful detection of mine-like objects. The ML(A) system was analyzed by carefully examining image data obtained from tests conducted off Eglin Air Force Base in December, 1994. Four hundred and sixty three images were analyzed, from which thirteen were found to contain mine-like objects. The result of this analysis was that there is a need to combine the advantageous aspects of these individual systems to develop an imaging system that takes more advantage of the benefits of range gating lidar techniques.

14. SUBJECT TERMS Laser, Lidar, Mine detection			15. NUMBER OF PAGES 153
			16. PRICE CODE

17. SECURITY CLASSIFICATION OF REPORT Unclassified	18. SECURITY CLASSIFICATION OF THIS PAGE Unclassified	19. SECURITY CLASSIFICATION OF ABSTRACT Unclassified	20. LIMITATION OF ABSTRACT UL

ii

AIRBORNE LASER MINE DETECTION SYSTEMS

Charles J. Cassidy
Lieutenant, United States Navy
B.S., United States Naval Academy, 1987

Submitted in partial fulfillment
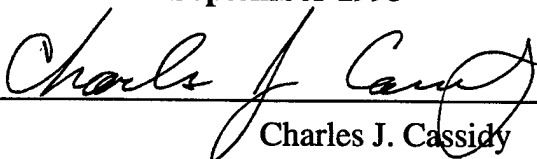of the requirements for the degree of
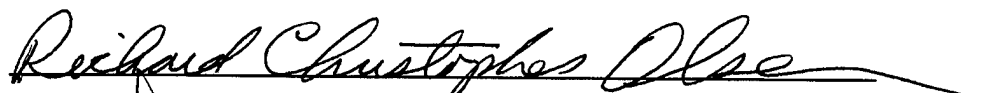
MASTER OF SCIENCE IN ENGINEERING ACOUSTICS

from the

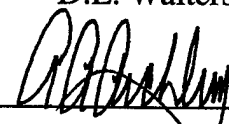## NAVAL POSTGRADUATE SCHOOL
September 1995

Author: _____
Charles J. Cassidy

Approved by: _____
R.C. Olsen, Thesis Advisor

_____
D.L. Walters, Second Reader

_____
A.A. Atchley, Chairman
Engineering Acoustics Academic Committee

iii

ABSTRACT

Mine detection has moved to the forefront as a concern for the United States Navy. The mine threat imposed by other nations has lead to the development and evaluation of relatively fast, efficient, and effective mine detection systems. Airborne laser radar has been suggested as a possible technique for minehunting. This paper analyzes data collected from two developmental systems. These systems were tested for the purpose of exploiting shallow water regions optically. These systems were Ocean Water Lidar (OWL), developed by NAWC, Warminster, Pennsylvania, and Magic Lantern Adaptation [ML)A)], developed by the Kaman Corporation, Bloomfield, Connecticut. The OWL system was analyzed by carefully examining each individual lidar scan from four system passes conducted off Eglin Air Force Base in September, 1994. Excellent bathymetry data was obtained, but the laser spot sizes used (one meter and twelve meters) precluded successful detection of mine-like objects. The ML(A) system was analyzed by carefully examining image data obtained from tests conducted off Eglin Air Force Base in December, 1994. Four hundred and sixty three images were analyzed, from which thirteen were found to contain mine-like objects. The result of this analysis was that there is a need to combine the advantageous aspects of these individual systems to develop an imaging system that takes more advantage of the benefits of range gating lidar techniques.

TABLE OF CONTENTS

vii

ACKNOWLEDGMENT

I. INTRODUCTION

Modern technology has led to great advancements in the development of highly sophisticated military systems and weapons. These programs have been available only to countries with large defense budgets within a relatively small procurement network. There is a weapon, however, readily and cheaply available to anyone in the world that has become one of the most cost-effective force multipliers of naval warfare. This weapon is the mine. Mines have become more and more desirable by belligerents world wide for many reasons: they are small, easily concealed, cheap to acquire, require virtually no maintenance, have a long shelf life, are easy to store in considerable numbers, and can be laid easily and simply from almost any type of platform. Mines can be deployed offensively and defensively to both protect one's own forces or waters, and to prevent an enemy's effective use of their forces or waters. Compared to the cost of a mine, the efforts required to counter and neutralize it are disproportionately huge. In order for the United States to continue to enjoy its present position at the peak of world military power, it must develop an efficient and effective means to deal with the menacing mine.

The United States Navy's policy, to retain the ability to project power forward from the sea (Department of the Navy, 1994), inherently suggests the need to be able to clear a path to high value targets such as ports, anchorages, or offshore structures for amphibious or seaborne attack. In order to be effective, these attacks must be carried out quickly and remain covert for as long as possible. Mines must be located accurately to

1

determine safe routes, or to select a more favorable target. Current developments include an airborne laser radar system for the minehunting task. An aircraft flown along a beach or port entry can relay real-time information about mine locations to the force commanders, while remaining relatively covert and out of harm's way, as opposed to other minehunting techniques which require hours to days close to a hostile area, both tipping off the hostile forces of possible landing areas, and giving them time to fortify those areas. The most crucial area for mine clearance is the shallow water, or littoral, portion of an amphibious landing route. This region has been notoriously difficult to exploit acoustically, and is more amenable to optical searches. This paper will analyze data from two systems that may be developed for this mission.

II. BACKGROUND

A. LASERS

1. A Brief History of the Laser

The key concept underlying a laser's operation, was first proposed by Albert Einstein in 1917. The physics was laid down and the underlying principles were in place as early as 1920 (Laurence, 1986). Considerable technological developments and evolution were required in order for all of the ingredients to be put together in just the right way to allow for the laser to work.

A great deal of work was being done in the 1940's with the development of microwave radars during World War II. Radar sends out microwaves and then looks for reflections of these waves from surrounding objects. The government was seeking sources of higher-frequency, shorter-wavelength radiowaves that could better serve the purpose of radar by traveling longer distances without spreading out and losing their power.

In 1954, Dr. Charles Townes was able to separate excited molecules in gaseous ammonia from the unexcited molecules, amplify them, and oscillate a microwave beam (Laurence, 1986). This became the first maser (Microwave Amplification by Stimulated Emission of Radiation). The microwave wavelength used was a poor beginning because it was absorbed by water vapor in the atmosphere, and the purity of the signal was not sufficient for communication. This idea of using molecules as amplifiers, however, paved the way for lasers.

3

In December, 1958, Dr. Townes and Dr. Arthur Schawlow published the first paper on how a laser might be made (Laurence, 1986). All of the ingredients were now available, and an operating laser followed shortly thereafter.

In May of 1960, Dr. Theodore Maiman, of Hughes Research Laboratories, built and operated the world's first laser (Laurence, 1986). It was a ruby laser that used a very powerful flash lamp to excite the chromium atoms in the ruby crystal, the result of which was an intense pulse of red light. This was the first time it had been possible to amplify a light beam.

Many of the intricacies about the development of the laser are subject to much controversy over exactly who did what, when. However, the Nobel Prize in Physics in 1964 was awarded to Dr. Townes, and, from the Soviet Union, Drs. N.G. Basov and A.M. Prokhorov, for their efforts in leading to the development of masers and lasers (Laurence, 1986). Since the first laser of Dr. Maiman, developments have occurred very rapidly, and the technology has expanded greatly.

2. What is a Laser?

The word laser itself, is an acronym for Light Amplification by Stimulated Emission of Radiation. Radiation , in this case, is electromagnetic energy as illustrated in the electromagnetic spectrum in Figure 1, where visible light represents a very small portion.

A laser is a device that uses a means of excitation to pump energy into the electrons of a lasing medium, which in turn emits and amplifies a light beam formed by

4

mirrors at each end of the lasing medium. The mirror at one end is partially transmitting, which permits the amplified light beam to escape from the laser. The color, or wavelength, of the light is determined by the difference in the energy levels of the excited state and that of the lower state.

There are three basic elements required to make a laser: a lasing medium, some form of excitation source, and an optical resonator. The lasing medium is the substance that actually generates the light. It can be a gas, liquid, or solid. The excitation source provides energy to the lasing medium. This is referred to as pumping. The optical resonator provides feedback into the lasing medium, which enhance the stimulated emission of light (release of photons).

There are many characteristics of laser energy which make it a desirable source of transmission (Hecht, 1982):

1. The electromagnetic radiation is monochromatic.

2. The electromagnetic radiation is coherent.

3. The electromagnetic radiation is collimated (highly directional) - this allows the light to be focused to a spot with a diameter equal to the wavelength of the light.

4. Light is available in a wide range of power levels (microwatts to terawatts).

5. Light can be available continuously or in incredibly short, powerful pulses.

6. Light is available in a wide range of colors (x-rays to microwaves).

The only way to produce strong stimulated emission is to have a population inversion; more excited atoms than unexcited atoms. This condition is created in a laser

by pumping atoms or molecules with energy at the proper wavelength to excite them to higher energy levels. The source of this energy may be electrical, chemical, nuclear, or optical.

As development and research of lasers has continued, many different kinds of lasers and lasing media have been tested and used operationally. Only the kinds used by the systems analyzed in this paper will be described here.

3. Neodymium(Nd) Lasers and Nd/YAG

One of the most common lasers is the neodymium(Nd) laser. It is a solid state laser consisting of an optical crystal with atoms of the lasing material embedded in the crystal. Solid state, in this case, is used to describe the fact that the lasing medium is a solid. The Nd laser has been found to have many advantages over gas lasers. First, it permits a higher density of lasing atoms, which allow it to develop more gain and produce more power output per unit volume. Second, an Nd laser is simpler to build and maintain than a gas laser due to its lack of glass tubes under vacuum and the need for supplies of gas. The Nd laser can operate pulsed or in a continuous mode since the solid-state laser crystals tend to be able to store energy with a reasonably long upper state lifetime (0.25 milliseconds). Pulsed operation results in considerably higher power levels. Also, solid-state lasers are easier and more effective to scale to larger sizes and can be pumped efficiently by semiconducting diodes.

As stated earlier, the Nd laser consists of neodymium ions embedded in a host material. The most popular host is yttrium aluminum garnet (YAG), from the garnet

family of crystals. YAG is chosen because it is transparent at the lasing wavelength and at the optical pumping wavelengths because YAG has a high thermal conductivity, it is able to withstand the high temperatures induced by the flash lamps without distorting, cracking, or changing optical properties. Also, its thermal stability permits continuous operation. It can provide continuous output powers from a few milliwatts to 100 watts or more, and pulse energies of 100 joules in 20 nanoseconds, resulting in power levels of 500 megawatts per pulse (Laurence, 1986). Finally, it can be built to very small scale.

The Nd/YAG laser emits a strong beam at 1.06 microns, which is in the infrared range of the electromagnetic spectrum. Nonlinear optical crystals, such as deuterated potassium phosphate, can be used in conjunction with Nd lasers to double the output frequency to 532 nanometers (the blue- green range of the electromagnetic spectrum).

4. Excimer Lasers

In 1975, J.J. Ewing, while working for AVCO-Everett, developed the excimer laser (Laurence, 1986). Excimer lasers are in the category of gas lasers. The basic operational concept is that energetic electrons from a beam, or discharge, deposit energy in the laser gas. This causes a rare gas (argon,krypton,xenon) to react with a halogen (chlorine, fluorine, bromine, iodine) to form an excimer (Hecht, 1982). An excimer is a molecule that can exist only in an electronically excited state. The excimer emits a photon (by spontaneous or stimulated emission) which causes it to break up into its constituent atoms instead of going to its ground state, of which there is none. This break up automatically ensures that the population of the lower level of the laser transition

remains zero, which simplifies the requirements for obtaining a population inversion. There is no absorption of laser light by the molecules in the ground state. Every excited molecule contributes to the population inversion, although the upperstate lifetime is only a few nanoseconds long.

Excimer lasers emit powerful pulses of light whose wavelengths are mostly in the ultraviolet region of the electromagnetic spectrum. The ultraviolet photons posses more energy for interaction with atoms and molecules, and for excitation of nonlinear processes generating light output at other wavelengths.

5. Dye Lasers

In 1966, Peter Sorokin, at IBM, discovered that dyes could be made to lase (Laurence, 1986). This led to the development of dye lasers, in which the lasing medium is a fluorescent organic compound, called a dye, in a liquid solvent. Because dyes have a broad emission spectrum, they can resonate at many different wavelengths. This aspect gives the laser wavelength tunability, and the wavelength of their output can be scanned over 10 to 40 nanometer ranges. Different types of dyes provide laser output over wavelengths ranging from the near-ultraviolet to the near-infrared.

The tunability of the dye laser arises from the fact that the dye is a complex molecule that has vibrational and rotational energy levels, as well as electronic energy levels. The transitions between energy levels makes it tunable. Two mirrors that form the optical resonator determine the output wavelength. Prisms or gratings in the

8

resonator will favor a high Q at only one particular wavelength at a time. Rotating the prism or grating tunes the laser to the desired wavelength.

Since the dyes used in this laser are liquids, they cannot sustain an electronic discharge, and, therefore, cannot be pumped electrically, but, rather, must be pumped optically. The optical pumping source must be in the green, blue, or near-ultraviolet regions of the electromagnetic spectrum. The molecules of the dye do not absorb light easily. Light tends to pass through without affecting the dye. Therefore, the pump light must be of high power and be very concentrated. This usually leads to the laser being pumped by another laser (e.g. an excimer laser) , which, of course, induces losses in overall efficiency. These losses are deemed acceptable, however, when the aspect of tunability is required or desired.

6. Charged Coupled Devices

The charged coupled device (CCD) was developed around 1970 as an advanced, solid-state, imaging detector to replace vidicon. CCDs have the advantage of small size, low weight, low power consumption, ultra-low noise, linearity, dynamic range, photometric accuracy, broad spectral response, geometric stability, reliability, and durability (Janesick, 1995). They are also better suited to image moving targets and are able to create a high resolution image, even in low-light conditions.

The basic functions a CCD performs in generating an image are: charge generation, charge collection, and charge transfer. Charge generation takes advantage of the photoconductive effect. When photons interact with the silicon of the CCD, they

excite electrons from the valence band to the covalent band. These photoelectrons are then collected in the nearest pixel. Pixels are defined by metal-oxide electrodes, called gates, formed on the surface of the CCD. The image generation process is illustrated in Figure 2, with the buckets representing the pixels of the CCD. The charge is transferred to a horizontal shift register of pixels at the end of each column by manipulating the voltage on the gates in a systematic way so that the signal electrons move down vertically from one pixel to the next in a conveyor-belt-like fashion. This register collects a line at a time and then transports the charge packets in a serial fashion to an output amplifier. An on-chip amplifier converts this charge packet to a useful output voltage that is amplified, processed, and digitally encoded off chip. The digital data is stored in a computer and an image is reconstructed on a television monitor (Janesick, 1995).

7. Applications of Lasers

Since their discovery, lasers have been used in many and varied applications in fields as diverse as medicine, construction, throughout industry, and the military. They have been used for such tasks as cutting steel, surgery, making straight lines, measuring air pollution, aiming rifles, illuminating targets, communicating without wires or radio, and even to guide bulldozers to cut perfectly level fields suitable for irrigation. Perhaps the most dramatic use of lasers was when Apollo Eleven placed a mirror on the surface of the moon so that a laser beam could be shot off the surface of the earth and reflected off the mirror to measure the distance from the earth to the moon to within centimeter accuracy.

B. LIDAR

It can be said that the first military application of using light to search for objects underwater can be traced to the use of searchlights on aircraft during World War II to illuminate the water and, thus, possible enemy submarines close to the surface. To illustrate the concept of lidar, an acronym for Light Detection and Ranging, it can be thought of as a direct extension of conventional radar techniques to the very short wavelengths produced by lasers. The lidar technique operates on the same basic principles as microwave radars.

Since these systems operate at much shorter wavelengths, laser radars are capable of higher range and angular accuracy than microwave radars. Laser systems, however, are more susceptible to the vagaries of the atmosphere and are, thus, generally restricted to shorter ranges in the lower atmosphere than microwave radar. New capabilities, such as tactical range and velocity imaging systems, autonomous missile guidance, precise aircraft navigation and guidance, precision fire control, and remote atmospheric sensing have become feasible with this great shift in wavelength (Jelalian, 1992).

Lidar systems combine the capabilities of radar and optical systems to allow simultaneous measurement of range, reflectivity, velocity, temperature, azimuth, and elevation angle. These six dimensions of target information can be utilized in fire control and weapon systems applications to allow target acquisition, tracking, classification, and imaging. Active lidar techniques have the advantage over passive IR systems in that the IR systems are dependent upon target emissivity and temperature characteristics, while

the laser system is target reflectivity dependent. This allows for reliable target measurement independent of time of day or target operation.

Laser technology allows the combination of coherent light sources, modulable in frequency and amplitude, with signal processing techniques based on radar technology. It extends underwater imaging techniques far beyond the use of standard video cameras for short-distance identification.

The laser's modulation capabilities allow for accurate target measurements and time/frequency gating of atmospheric or terrain background clutter. This has led to the main advantage of a lidar imager, compared to a standard optical system: its ability to gate the return signal versus range thereby separating spurious light backscattered by the medium from that reflected by the target.

III. THEORY

The concept behind an airborne laser radar is that a scanner system in an aircraft sweeps a laser beam consisting of a series of very short, intense pulses of light, in a plane normal to the aircraft's motion. To achieve a contiguous scan on the ocean surface or at a desired depth in the water, requires the selection of the proper pulse repetition frequency, spot size, and angular scan rate. The signal received from the target is superimposed on the background and laser radiation reflected from the surface, and laser radiation backscattered from the water. An optical receiver detects the reflected pulses that travel back to the sensor system. Range gating and filtering enhance the target signal.

Range gated systems synchronize the laser transmitter and signal receiving sensor so that the system receives light from a specific range. Light reflected from the atmosphere, water volume, and objects at any other range is excluded.

A. ENERGY

Optical radiation propagates with wave characteristics, but the creation and detection process involves discrete packets of energy. The energy associated with one photon packet is equal to (hf), where h is Planck's constant ($6.626*10^{-34}$ J·s) and f is the transmitter frequency. The number of photons arriving in an optical receiver in a second is the received energy divided by (hf) (Jelalian, 1992). The number of photons arriving

per second at a specific wavelength times Planck's constant gives the received power.

As the wavelength becomes shorter, the energy of a photon increases.

B. LASER RANGE EQUATION

The laser range equation expresses the received energy (power) as a function of

the transmitter energy (power), output beam divergence, range from the receiver,

optics/atmospheric and sea water transmission, and receiver collection aperture.

As illustrated in Figure 3, the basic form of the laser range equation is:

$$P_r = \{P_t/(R^2 \Omega_t)\}(\rho A_r)\{A_c/(R_r^2 \Omega_r)\}(\eta_t \eta_r) \qquad \text{[Equation 1]}$$

Where: P_r = Received power (energy) from target

P_t = Transmitted laser power (energy)

R = Range from the transmitter to the target

R_r = Range from the receiver to the target

Ω_t = Solid angle of the transmitted beam

Ω_r = Solid angle of the reflected beam

A_r = Cross sectional area of the reflecting target = $\{(\pi/4)R^2 \Omega_t^2\}$

A_c = Receiver clear aperture area

ρ = Average reflectivity of the target

η_t = Transmission coefficient for the transmitted beam
(includes optics as well as atmospheric/water properties)

η_r = Transmission coefficient for the reflected beam
(includes optics as well as atmospherics/water properties)

C. NOISE

In any transmitting and/or receiving system, anything other than the desired signal is considered to be noise.

1. Background Noise

Background noise in optical receivers includes reflections of signals from the earth, the sun, the atmosphere, clouds, or any other source that contributes an undesired signal to the receiver. This effect is analogous to turning on one's headlights on a foggy night. The brighter one's lights are, the more light is scattered back at the vehicle, making it more difficult to see the desired signal: the road. This same problem can occur for ungated laser systems propagating radiation into clear air, haze, and clouds.

2. Thermal Noise

Thermal noise, normally represented as kT, produces blackbody radiation. In this case, k is Boltzman's constant ($1.39*10^{-23}$ J/K), and T is absolute temperature in degrees Kelvin. The Stefan-Boltzman radiation law relates the power emitted from a blackbody radiator to the fourth power of the temperature of the radiator. The total blackbody radiation emitted over a 2π solid angle, P_{bbt}, may be expressed as the product of the radiant emittance, I_e, and the surface area within the field of view, A_s, as in the following equation (Jelalian, 1992):

$$P_{bbt} = I_e A_s = \sigma_t T^4 A_s \qquad \text{[Equation 2]}$$

Where: σ_t = Stefan-Boltzman constant = $5.67*10^{-12}$ Wcm^{-2} K^{-4}

T = Absolute temperature (degrees Kelvin)

A selective optical filter can be used to allow the receiving system to pass only a portion of P_{bbt}, thereby reducing the blackbody background noise contribution.

3. Signal Induced Noise

Signal-induced noise refers to the shot noise caused by the received signal itself coming into a detector. The received signal includes a variance in the number of photons per second received. This variation appears as noise. Often, this is referred to as quantum noise because it is induced by the signal when the signal exists.

4. Noise Power Spectral Density

The relationship between the wavelength and the dominant noise of a system may be demonstrated in the noise power spectral density referred to the input (ψ) in Watts/Hertz as in the following equation (Jelalian, 1992):

$$\psi(f) = ((hf)/\{(\exp[(hf)/(kT)])-1\})+ hf, \qquad \text{[Equation 3]}$$

where all terms are defined as previously.

From this equation, it can be determined that at wavelengths lower than 10^{-4} meters (visible light), thermal noise is the minimum discernible noise source. In the region of the electromagnetic spectrum from 10^{-4} meters toward shorter wavelengths, the minimum detectable signal is actually the photon noise (signal-induced noise). This is also illustrated in Figure 4, which is a plot of the noise power spectral density versus wavelength.

D. SEA-WATER AS A TRANSMITTING MEDIUM

Most lidar work has been done with the atmosphere as the sole propagation medium. Air is not a perfect homogeneous medium, and internal induced density fluctuations alter the index of refraction. In addition, particulates must be considered when predicting, and accounting for, the energy propagation. An airborne lidar system for use as a sea-water searching device must consider not only the atmosphere, but also the air/water interface, the water itself, and the sea bed from which the energy is reflected.

The shape of the lidar return signal provides information about the state of the medium. Interpretation of the results of this process, in sea water, is quite a difficult problem. Since sea-water is a multicomponent medium, it is both an absorbing and scattering medium. Absorption and scattering are mainly due to the presence of organic or mineral particles suspended in the sea-water, the size of which are generally larger than the laser wavelength. Multiple interactions of radiation with these scattering and absorbing particles distorts the signal shape. Atmospheric scattering and the interaction with the air-water interface can modify the pulse shape (Shamanaev, 1994).

1. Particle Density

Particle density may vary greatly from one type of water to another, but regardless of particle density, the spectral window of least attenuation for sea-water is in the blue-green range of the electromagnetic spectrum between 410 nanometers and 550 nanometers. Minimum absorption varies with the water particle load, and shifts to the

17

yellow range when the particle load increases (Kervern, 1992). In the blue-green region

of minimum absorption, underwater optical properties are quite different from acoustical

properties. Figure 5 reveals the weakness of optics in effective propagation, which may

vary greatly from one body of water to another, or from season to season, but it also

reveals optic's unique advantage of high potential resolution and efficient crossing of the

air/water interface (Kervern, 1992).

2. Attenuation, Absorption, and Scattering

The attenuation coefficient of sea-water includes contributions from radiation

scattering and absorption by water, suspended particles, and dissolved organic

components.

The beam attenuation coefficient, denoted c, is the attenuation for a narrow beam

of laser energy, and is one of three coefficients used to model sea-water optical

characteristics with reasonable accuracy. The other two are the absorption and scattering

coefficients, denoted a and b respectively, such that $c = a+b$ (Kervern, 1992). Figure 6 is

a graph of the attenuation coefficient for pure filtered water as a function of wavelength.

The effective range of the lidar system depends on the transmitted optical power and the

attenuation of the sea-water. Attenuation varies from one type of water to another and

leads to an exponential decrease of the transmitted power. For wide field of view laser

systems, it is more valuable to measure the diffuse attenuation coefficient as opposed to

the beam attenuation coefficient. Most current models assume the water is homogeneous

in depth and lateral range. However, in seawater, an appreciable gradient in the diffuse

attenuation coefficient has actually been observed. Figure 7 illustrates the differences in the diffuse attenuation coefficient as a function of wavelength for different water types. This gradient can be accounted for in explicit numerical integrals which require the specification of an assumed or measured diffuse attenuation coefficient profile.

The inverse of the attenuation coefficient is the attenuation length. The attenuation length is the distance where the intensity of a parallel light beam declines by a factor of e (natural log base), or about 4 decibels.

In shallow water, using aircraft at relatively low altitudes, the dominating factor determining the effectiveness of a lidar system, is the scattering coefficient for the sea-water, referred to as b above. The sea-water volume backscatter coefficient as a function of angle, denoted $\beta(\theta)$ (in meters^{-1} steradians^{-1}) is very difficult and time consuming to measure accurately, but vital in determining an accurate b value, and, thus, the probabilities of detection for the system. This term changes drastically from one region of coastal waters to the next due to both organic and inorganic particles and substances suspended and mixed within the water volume. This same variability has been witnessed on a scale of mere meters between successive laser pulses.

Coastal Systems Station, Panama City, Florida, has sampled waters off the Florida and California coasts in conjunction with airborne laser system tests. Figures 8 through 13 are plots of values received from CSS, Panama City, which provide an illustration of the variability of the volume backscatter coefficient from one coastal region to another. Figure 8 shows values for measurements taken along the coast of San Nicholas Island off

the Southern California coast on 11 August, 1995, at 0823 in the morning. This Figure illustrates not only the variability of the backscatter coefficient with depth, but also the high values associated with the California coastal region. Figure 9 shows, once again, the backscatter variability with depth in the same region and on the same day as Figure 8, but this survey was done in the early afternoon. Comparison between Figures 8 and 9 illustrates how backscatter values change with time of day. This variability with time of day reveals the effects of tidal transport of particulates to the coastal regions. Figure 10 is a plot of values from 12 August, 1995, at 0655 in the morning for the same region surveyed for Figures 8 and 9. This figure is a more telling example of how the backscatter coefficient can change on a time scale of approximately one day. Tidal effects are illustrated, once again, upon comparison of Figures 10 and 11. Figure 11 shows data for the same region on the same day as Figure 10, but later in the morning. Figure 12 is a plot of backscatter coefficient values for the coastal region of Okaloosa Island, off the Northwest Florida coast. The relative clarity of the water of this region, when compared to that of the California coast, is evident by the drastically reduced backscatter coefficient values. Notice, however, variability with depth remains a factor. Figure 13 is a plot of values taken approximately twelve nautical miles off the shore of Northwest Florida. These values dramatically show the difference between clear open water and the near shore regions of the previous figures. Daily variability, however, is still evident.

As stated by Brett Cordes, Electronics Engineer working as lead analyst for Magic

Lantern programs at Coastal Systems Station Panama City, Florida:

The key environmental results of these tests has been the sharp gradient in optical degradation as one approaches the surf zone due to increased particulates stirred by wave action. The other significant result was that the majority of the total loss was due to scattering. Direct attenuation did not dramatically increase. System results backed the environmental measurements. Relatively low laser pulse energy returned adequate return from the bottom. High power did not produce better results since receivers were not photon limited. Scattering reduced the target contrast and dominated the return through blur effects.

The volume scattering function, shown in Figure 14, represents the radiation

pattern of energy scattered by the sea-water volume unit (Kervern, 1992). It has been

shown experimentally that the shape of the volume scattering function varies little from

one sea-water region to another.

3. Optical Density

The abrupt change in index of refraction between air and water produces a 2%

reflection at the air/water interface. This leads to the signals from the water and from the

atmosphere and air/water interface entering a detector simultaneously. In the design and

performance of lidar measurements, this effect must be taken into account (Shamanaev,

1994).

An increase in the optical density of sea-water causes a decrease of the relative

contribution of the atmospheric component to the signal. It has been found through

bathymetric application of lidar that the depth of sounding coastal water is limited by its

optical density, not the atmosphere (Shamanaev, 1994).

4. Effect of Wind-Driven Sea Waves

The energy of the lidar signal coming from a subsurface water layer decreases with an increase in wind velocity. Increasing wind velocity causes an increase of wind driven sea waves, which induce a nonstationary interface, which, in turn, results in an intensification of reflection and re-reflection of radiation scattered by the interface.

Surface wave focusing effects the apparent brightness of the backscattered radiation. This effect is time-varying, and this modulated return causes a large scatter in the signal-to-noise ratio and target signature. Although this effect cannot be totally eliminated, it can be mitigated by increasing the transmitter energy, increasing the receiver sensitivity, Increasing the transmitter and receiver field of view, or by formulating an algorithm that accounts for the surface focusing.

In the case of very high sea states or shallow water where there may be breaking waves, other factors are induced. First, there will be a higher presence of aerosols in the atmosphere just above the sea surface caused by the sea spray, increasing the optical density of the atmosphere, and, thus, the scattering effects of the atmosphere. Second, the presence of bubbles, foam, and mixed particulates caused by the breaking waves may scatter the incident radiation so severely that it may become virtually unreceivable by the system.

5. Effect of The Sea Bottom

In different coastal regions, or along a single coastal region, there are large variations in bottom color, brightness, and texture over distance. In some areas these

distances can be just a few meters. These variations are a function of depth, vegetation, sand waves, coral heads, channels, and other such factors.

Differences such as these lead to rapid changes in the pulse width and amplitude of the energy reflected from the bottom, and, thus, large variations in data about the bottom structure, and the depth of the water itself.

For imaging systems that depend on the relative difference in the reflectivity of the target and the bottom, an inhomogeneous bottom makes it difficult to identify a target. If the target has the same reflectivity as the bottom, or at least approximately so, the job of differentiating between the target and the bottom is greatly exacerbated.

IV. AN APPLICATION OF AIRBORNE LIDAR

A. AIRBORNE LASER BATHYMETRY

Airborne laser bathymetry is a relatively new tool that allows very rapid hydrographic surveys to be conducted in shallow waters without the common marine navigation difficulties. This technique offers the advantages of being fast, allowing low cost surveys of coastal areas, and is especially useful when these areas are spread out, difficult to reach, or require repetitive surveys (Kervern, 1992).

Figure 15 shows the results from the test of a French system conducted in Cameret in November, 1986 (Kervern, 1992). This figure shows that the achievable accuracy of a laser system is comparable to, if not better than, that of existing acoustic systems.

The basic operating principles of airborne laser bathymetry systems are that a pulsed laser on board an aircraft sends an ultra-short (5-10 nanosecond) luminous pulse to the sea bed. This pulse is located in the blue-green spectrum where, as previously stated, sea-water is least absorptive. This pulse travels through the atmosphere, experiencing practically no attenuation, to the air/sea interface. Once the pulse hits the water, the first echo is retransmitted to the receiver due to the difference between the air's and the water's index of refraction. Air's index is one, while water's is approximately 1.333 (Kervern, 1992). As this pulse continues through the water column, suspended particles of organic origin (plankton) or mineral origin (sediment) diffuse the transmitted light, and produce a diffuse echo due to volume reverberation or

25

backscattering. The amount of this backscattering depends upon the concentration of these particles. The sea bed produces a final echo. The amplitude of this echo depends on the bottom type.

The time difference between the sea surface echo and the bottom echo (Δt) provides the water depth (h) using the following formula (Kervern, 1992):

$$h = (c*\Delta t)/2 \qquad \text{[Equation 4]}$$

where: c = velocity of light in water $\cong$ 225000 kilometers/second

B. AN EXAMPLE: LARSEN 500 (CANADIAN)

1. System Concept/Description

The feasibility of measuring water depth with an airborne lidar system was first demonstrated in the 1960's. The Canadian Larsen 500 system represents approximately ten years of work that started in the 1970's (Banic, 1986). This scanning, airborne hydrographic surveying lidar bathymeter has a depth penetration capability of four optical diffuse attenuation lengths with an accuracy of $\mp$.3 meters (Banic, 1986). At its nominal altitude of 500 meters, the swath is about 270 meters. It incorporates a uniform sounding density on a 35 meter grid spacing with a positioning accuracy of about 15 meters (Banic, 1986).

This system uses a Q-switched, frequency doubled Nd/YAG laser. Q-switching forms a higher level of population inversion. Frequency doubling produces a short pulse of infrared (1064 nanometers) and green (532 nanometers) laser radiation. The average repetition rate is approximately 20 pulses per second. The laser generates two megawatts

of peak power in a five nanosecond pulse at 532 nanometers and approximately five megawatts in eight nanoseconds at 1064 nanometers (Banic, 1986).

The high attenuation coefficient of water at 1064 nanometers prevents the infrared pulse from penetrating more than a few centimeters. Thus, the water surface scatters the infrared pulse while the green pulse penetrates the water column and is scattered from the bottom. The receiver in the aircraft detects both scattered pulses, and the elapsed time between the two is used to measure the water depth.

A beam expanding telescope, and two beam steering mirrors, direct the laser output beam toward the water by way of a scanning mirror. Laser firing control allows a specific and highly uniform grid pattern to be generated on the water. The accuracy of the grid is determined from calibrated laser beam exit angles relative to the optical sensor frame, together with aircraft position, altitude, and attitude information.

The relatively low repetition rate of the laser requires a uniform scan pattern in order to provide efficient ground coverage. A constant scan angle will minimize the amount of corrections to raw depths in the data processing since underwater propagation path depends on the beam incidence angle. A scan angle of 15 degrees minimizes the depth bias over the entire range of water parameters (Banic, 1986).

A quasi-conical scanner, rotating mirror, and staggered-time laser fire control produce an elliptical scan on the ground, displaced relative to the aircraft that has a nearly constant scan angle over the swath width. The proper sounding pattern is achieved by firing the laser, through a time code generator, once per rotation of the

scanning mirror, to provide nine equally spaced points across the swath. The result is a series of nine parallel tracks.

The operator sets the range gate in the receiver to prevent false triggering of the receiver system from aerosol scattering or low-lying haze or fog. The operating altitude determines the range gate.

The receiver includes a telescope with a .2 meter aperture and a 1.4 meter focal length, for a three degree total field of view (Banic, 1986). It also incorporates a five milliradian spatial block to attenuate water surface return in the green channel, while allowing subsurface scattered light to pass unattenuated. The optical path includes baffles between the focusing lens and the green receiver. The green channel detector is a photomultiplier operated at low gain to prevent saturation during high ambient light conditions.

The data acquisition system records the digitized lidar waveform, the orientation of the optical sensor, the aircraft position and altitude (also used to provide real-time guidance information to the pilot), slant range to the water surface, and the velocity data from the aircraft's inertial reference system. A high resolution nadir-looking video camera provides a visual image of the scanned region.

2. Brief Discussion of Test Results

Flight tests took place in the summer and fall of 1984, and again in the spring of 1985 over Ottawa River, Lake Ontario, and Lake Huron. Dissimilar sites provided diversity in water clarity, depth and surface wave structure, and ambient light conditions. Lidar data was compared to that obtained from a previous high density acoustic survey. The standard deviation of the lidar measurement error was .26 meters (Banic, 1986).

The Larsen 500 deployed on its first hydrographic survey mission in August 1985 in the Canadian arctic for the purpose of producing navigation charts. This involved 200 flightlines covering an area of 2000 square kilometers with 30 hours of recorded data (Banic, 1986). Figure 16 shows samples of sequential lidar waveforms recorded in the arctic. The narrow peak of constant width and amplitude at the beginning of each trace is the infrared surface marker pulse. The second peak is the volume backscatter from the water, and the last peak is the bottom return, both of which are from the green lase pulse . The final result was that the system demonstrated the ability to meet the requirements of the Canadian Hydrographic Service by successfully completing a major operational survey.

V. AIRBORNE LIDAR AS A MINEHUNTING TOOL

Laser technology and its application in exploiting sea-water as a medium has given rise to the possibility of its use as a minehunting tool. Whether mines are floating in the sea-water volume or laying on the sea bed in shallow water areas, examining the electromagnetic radiation scattered by them can provide for positive detection, and, with high resolution, classification.

This paper will analyze data collected from two systems considered as possible airborne laser mine detection systems: Ocean Water Lidar, and Magic Lantern. Ocean Water Lidar (OWL), developed by the Naval Air Warfare Center (NAWC), Aircraft Division, Warminster, Pennsylvania, was used to conduct an airborne lidar bathymetric survey of Hamlet's Cove Test Range. Magic Lantern is a lidar-based mine detection system developed by Kaman Corporation, Bloomfield, Connecticut. The variant of the Magic Lantern system applicable to this paper is the Magic Lantern Adaptation, referred to as ML(A), and has been adapted for detection of small mine-like objects (anti-invasion mines which are smaller and lay closer together than most other mines) in the region from water depths of approximately ten feet to the high-water-mark on the beach.

The data presented in this paper are from flights of the two individual systems conducted over the waters off the coast of Northwest Florida. Although these flights were conducted at different times of the year, times of day, and different water conditions, the basic principles and physics behind the concepts of operation are comparable.

A. OCEAN WATER LIDAR (OWL)

1. System Concept/Description

The OWL system was developed originally for anti-submarine warfare purposes, but has also been used for lidar bathymetric survey purposes. Figure 17 is a conceptual system diagram of a laser sounder similar to the OWL system. The weight of the system is approximately 6000 pounds, and requires 25 KVA of three phase 400 Hertz power. These size, weight, and power consumption requirements necessitated a dedicated aircraft to support the flight testing. The lidar system was designed, fabricated, and installed aboard a P-3A, BuNo. 152150, aircraft by the Naval Air Warfare Center (NAWC), Aircraft Division, Warminster, Pennsylvania. As illustrated in Figure 18, extensive modification of the aircraft was required to satisfy program requirements.

The system utilizes two XeCl excimer lasers to pump a dye laser operating at a nominal pulse repetition frequency (PRF) of 500 Hertz as the transmitter. A 26.5 inch diameter Galilean telescope focuses the lidar return signal onto a six-stage gated photomultiplier tube (PMT). The transceiver uses a coaxial design with the transmitted pulses circularly scanned, 15 degrees from nadir, to achieve a 30 degree full angle scan pattern. Four VME based computers perform the data acquisition and system control.

The system consists of three major subsystems: the transmitter, the receiver scanner, and the data acquisition/control. Figure 19 is a block diagram that shows, in conceptual form, the interconnection between the various system components.

2. OWL System Specifications and Parameters

a. Excimer Laser(Dye Laser Pump Source)

Wavelength	308 nanometers
Pulse energy	200 millijoules
PRF	250 Hertz (approximately)
Average power	50 Watts
Pulsewidth	22 nanoseconds
Pulse to pulse stability	±3%
Pulse size	10x23 millimeters
Jitter	±2 nanoseconds
Adjustable time delay	1-3.5 microseconds
Beam divergence	.4 milliradians

Table 1. Excimer laser parameters.

b. Dye Laser

Wavelength (with Coumarin 102)	470-510 nanometers
Pulse energy	30-40 millijoules (typical)
Average power	15-20 Watts (typical)
Pulsewidth	18-20 nanoseconds (typical: full width half maximum)

Table 2. Dye laser parameters.

c. Receiver (Telescope)

Type	Refractive Galilean
Aperture	.29 meters^2
Diameter	26.5 inches
Field of view	1.0-10.1 degrees full angle
Detector	ITT F4084 (six stage)
Bandwidth	300 Megahertz
Photocathode	S-20
Quantum efficiency	12% at 480 nanometers

Table 3. Receiver parameters.

d. Scanner

Transmitter	Rotating optical wedge
Receiver	Rotating fresnel wedge
Scan angle	15 degrees
Scan rate	1.2, 1.5, 2.3, 3.1, 4.6, 6.1, 7.7, 9.1 (Hertz)

Table 4. Scanner parameters.

e. Analog to Digital Converter

Sample interval	1-10 nanoseconds
Number of samples	1024
Bit accuracy	5.2-8.2 bits (depending on bandwidth)

Table 5. Analog to digital converter parameters.

f. System

Jitter	1.6 nanoseconds
Beam divergence	.03-8.8 degrees

Table 6. System parameters.

3. Subsystem Descriptions

a. Laser Transmitter Subsystem

The laser transmitter subsystem consists of two Lambda Physik Model EMG 203 XeCl excimer pump lasers and a customized dye laser. These lasers had to be ruggedized and converted to operate on 400 Hertz power aboard a P-3 aircraft. This was done by NAWC. The excimer lasers generate ultraviolet light at 308 nanometers used to pump a tunable dye laser. The dye laser converts the ultraviolet light to the blue-green region of the visible spectrum and is tunable between 470 and 510 nanometers. Coumarin 102 is the lasing medium. Each excimer laser operates at a maximum PRF of 250 Hertz and sequentially pumps the dye laser to achieve a 500 Hertz system PRF.

b. Receiver/Scanner Subsystem

Figure 20 is a block diagram of the transceiver. The system uses a coaxial transmitter and receiver arrangement, with the receiver telescope mounted vertically over a 36 inch square by two inch thick Plexiglas window put in the underside of the aircraft as part of the extensive modifications. Laser pulses are directed from the transmitter subsystem to the scanner mounted below the aircraft floor by the output optics. The optics components consist of three mirrors, two lenses, transmitter optical wedge, and the aircraft window. Also illustrated by Figure 19, at the telescope enclosure, mirror one (1) directs the laser output below the aircraft floor to the longitudinal axis of the scanner and mirror two (2) directs the beam to the center of the receiver telescope. Mirror three (3)

directs the beam to the optical wedge, which in turn bends the light 15 degrees from

nadir before exiting the aircraft through the aircraft window.

A diverger assembly consisting of lenses one (1) and two (2) controls the

laser spot size. Lens two is fixed, while lens one is adjustable under servo control from

the Data Acquisition/Control Subsystem(DACS). The distance between these two lenses

and the altitude of the aircraft determines the transmitter spot size on the water surface.

The receiver telescope utilizes six lenses, an iris, and an interference filter,

which focus the lidar return onto a gateable photomultiplier tube (PMT) as illustrated in

Figure 21. A PMT provides the desired dynamic range (approximately 10^6). The iris is

used to control the field of view of the receiver, and has an adjustable diameter of .5 to

6.1 inches (1.0-10.1 degrees full angle field of view). A DACS controls the iris. An

index matching fluid between the final collecting lens and the PMT minimizes the total

internal reflection losses at the front surface of the PMT. Interference filters are used

only during daylight flight operations.

The scanner is mounted in front of the receiver objective lens and contains

the transmitter optical wedge and the receiver Fresnel wedge, which collects light 15

degrees off nadir. These components are rigidly connected and rotate simultaneously to

achieve a 30 degree full angle circular scan pattern and insure that the receiver and

transmitter remain in alignment. The scanner rotation is counterclockwise viewed from

the top of the aircraft. The orientation of the laser beam shape does not change with

scanner rotation.

The receiver consists of the gated PMT, high voltage power supply, and analog signal processing electronics. The PMT is an ITT model F4084 with a 1.5 inch aperture, utilizing six dynodes, an S-20 type photocathode, and a grid gate control. The signal detected by the PMT is split, processed through one of four analog circuits, and sent by a line driver/line receiver to a Tektronix 2000 digitizer.

c. Data Acquisition/Control Subsystem

The Data Acquisition/Control Subsystem(DACS) provide computer control of the lidar hardware. The DACS consists of four VME-bus based computer systems, which perform four separate tasks: system control and data recording, navigation data collection, data read back and display, and transceiver control. Return laser pulses are digitized at a 500 Hertz rate by the Tektronix 2000 digitizer and recorded on the High Density Digital Recorder (HDDR) with sufficient ancillary data to calculate the number of photons returned from a given depth slice of ocean water at a given time. In particular, this subsystem performs the following nine tasks:

1. Control transmitter parameters (beam divergence, PRF, scan rate).

2. Control receiver parameters (field of view, PMT gain).

3. Digitize and record laser return pulses at 500 Hertz.

4. Display laser waveforms to verify system operation (at one Hertz rate).

5. Interface to the aircraft Inertial Navigation System and a Global Positioning System and record aircraft position, attitude, and altitude.

6. Record lidar sensor parameters on a shot-by-shot basis.

38

7. Record the output of the optical angle sensor which measures the beam angle on the final mirror as well as the transceiver platform inertial information such as linear and angular acceleration.

8. Record system timing information associated with each laser shot.

9. Provide operator interface to change system parameters inflight.

The Tektronix 2000 digitizer contains four channels, each of which can store up to 1024 samples, with a minimum sample time of two nanoseconds per sample. Default sampling rate is two nanoseconds, but this can be varied between two and ten nanoseconds in one nanosecond steps.

A Fairchild Model 85, 28 track, HDDR, records the data at a tape speed of thirty inches per second, at a clock rate of 800 Kilohertz.

4. Description of Experiment

The Naval Air Warfare Center (NAWC), Aircraft Division, Warminster, Pennsylvania, conducted an airborne lidar bathymetric survey of the Hamlet's Cove Test Range off Eglin Air Force Base in northwest Florida. The survey was performed using NAWC's Ocean Water Lidar (OWL) system operating from a NAWC P-3A fixed wing aircraft. Missions were flown over the range on 07 and 08 September, 1994.

Six sets of passes were flown in a northerly direction from deep water toward the shoreline. One set of passes was flown in a westerly direction parallel to the shoreline. Laser spot size varied between these sets of passes and had values of one meter, six meters, and twelve meters. The laser pulse width had values of eight nanoseconds or 4.5 nanoseconds. The total number of passes flown was sixty two, and a subset of these

consisting of eight passes with a twelve meter spot size were selected to form the bathymetric database. A sample by sample processing of the database determined the difference between the surface and the bottom reflections. The ancillary data were used to position the sample in the aircraft reference frame. Sample position compensation included: scan angle, roll, pitch, and drift. A differential Global Positioning System provided the aircraft position.

The data analyzed in this report are of two of the northerly passes and a westerly pass with the aircraft flying at an altitude of approximately 600 feet. The northerly passes were chosen to allow for an observation of the change in lidar waveform as the system transitioned from a region with no bottom, to the shallow water region, to the beach, with laser spot sizes of one meter and twelve meters. The westerly pass, with a laser spot size of one meter, provided a signal consistently within the difficult region of shallow water.

In order to effectively analyze these waveforms, a computer program was developed to allow stepping through each subset of data to observe the levels of lidar return within the water columns searched by the system. The laser return included a strong signal from the air/sea interface and the sea bottom. The portion of the waveform between these two regions contains the desired signal that would indicate the presence of a mine-like object either within the water volume, or close to the bottom.

B. MAGIC LANTERN ADAPTATION [ML(A)]

1. System Concept/Description

The general ML(A) system is a wide area lidar system developed by the Kaman Aerospace Corporation of Bloomfield, Connecticut, to detect, classify and localize floating, moored, and bottom mines, and provide real time imagery of the beach and/or the bottom in the surf zone. Figure 22 is a conceptual diagram of the system provided by Coastal Systems Station, Panama City Florida. It incorporates a solid state blue-green laser and uses a frequency doubled output wavelength of 532 nanometers with nanosecond pulse widths. It has been tested on the SH-2F helicopter, but may be adapted for use on a number of other airborne platforms. Figure 23 shows the system configuration on an SH-2F with its three major components: the pod, the equipment rack, and the operator station. The total Magic Lantern equipment weight is 1139.40 pounds. Six intensified charge coupled device (ICCD) cameras capture reflected energy from a gated slice of a water column. The intensified charge coupled device works the same as a basic CCD, but is designed to allow for better low light imaging capabilities. The computer processed image displays mine-like objects (reflections/shadows) with rough approximations of shape and relative location to the system operator. Figure 24 is a functional diagram of the system. Each detected object is also logged in a data base. A tactical display is available showing the aircraft position and location of all detections. An onboard global positioning system is used for position accuracy. An Ampex tape system records the display for post mission analysis.

ML(A) uses a nine nanosecond long pulse of green light at a 40 Hertz pulse repetition frequency (PRF) to illuminate a portion of the water volume as the helicopter moves forward. This volume becomes a strip bounded in the cross track direction by the system's field of view, and in depth by the critical depth gate chosen for target detection. The aircraft's radar altimeter is used to determine altitude. The system has low, medium, and high active power settings, and can be used passively as well.

The system scans from left to right, oriented to the front of the aircraft, in thirteen equal steps. There are then two dead pulses to return to position one, for a total of fifteen pulses per sweep. Scan position one is farthest left, seven is nadir, and thirteen is farthest right. There is also a stare mode at any one of the thirteen scanner positions (not to be confused with a steer mode). In the passive mode, the laser is off. The system has a polarizer to reduce surface glint. Synchronously with the laser firing, a roll axis scanner is sequentially driven to thirteen predetermined positions so that the sensor line of sight is stepped along rows.

ML(A) has been adapted for use in shallow water (i.e. the surf zone) from a water depth of about ten feet, to the high water mark on the beach, and must be able to image relatively small objects, on the order of six inches to approximately one foot, on the bottom. It is for this reason, that the receiver cameras are gated and configured to cover a predetermined area as opposed to gating to cover various depth slices within a deep water volume.

The systems depth gate is set just above the bottom, necessitating the incorporation of a bottom follower to update the bottom location. For the portion of the scan on the beach, the cameras are gated just above the beach to minimize glint. The bottom follower locates the bottom, surf, or beach to within one foot (approximately two nanoseconds). It estimates the total round-trip time for the next shot by using current measured bottom data with past measurements to provide an estimate for gating the next shot. A Kalman filter is used for this process.

Magic Lantern uses a unique type of lidar called range gated imaging. In range gated imaging, the optical receiver is a type of camera and the signal is displayed as an actual image capable of being displayed on a video monitor. Figure 25 is a space-time diagram for an imaging lidar system.

In summary, first, a pulse timing generator triggers the pulsed laser to fire. Then, the laser pulse is sent through optics which spread out the pulse to illuminate a patch on the water. The laser pulse penetrates the water and illuminates both the water and any objects in the water. The pulse is backscattered from the water and the object and travels back to the six intensified charge coupled device cameras. The pulse timing generator sends gating signals to each camera at the precise moment when the pulse returns from the desired range, and a very short exposure is made by the camera. The resulting images are either sent to an Image Processing Computer (IPC) for automatic target detection, or is sent to the operator's video display for manual viewing. Figure 26 shows the path of light as it is processed by the system.

2. Subsystems Descriptions

Figure 27 shows the arrangement of the various subsystems within the Magic Lantern sensor pod.

a. Scanner Subsystem

The scanner has two mirrors attached to a single shaft that is driven by a torque motor. A small laser scan mirror deflects the high peak power laser pulse. The second mirror is larger, and steers the lines of sight of the six boresighted, gated, intensified charge coupled device receivers. The timing of the electronic shutters for each of the six receivers is adjusted independently by the computer using programmable time delay generators. Each receiver gate can be set independently. The aircraft's radar altimeter determines the exact distance to the water surface to allow for compensation of the laser pulse time of flight from the sensor pod to the water surface.

To ensure the absence of gaps in the scan pattern, the scanner provides overlap between scans. The nominal crosstrack (footprint to footprint) overlap is twenty eight pixels, while the minimum along track (scan line to scan line) overlap is seventy four pixels.

b. Laser Transmitter Subsystem

ML(A) uses an Nd:YAG laser whose fundamental frequency is in the infrared range of the electromagnetic spectrum at 1.06 microns. The beam is then sent through a harmonic generator which converts the infrared light to green at 532 nanometers. The conversion efficiency from infrared to green is nominally 50%. The output pulse energy

in the green wavelength is 0.5 Joules/pulse at the operating PRF. The pulse is less than ten nanoseconds long and the beam diameter before laser optics is approximately one centimeter. Figure 28 is a schematic of the ML(A) Nd:YAG laser.

After conversion to green light, the pulsed beam is sent into the laser optics section. The laser optics expand the small diameter beam and send it out into a fixed cone angle. The input laser has a Gaussian (bell) shape. To compensate for this, the laser passes through a beam homogenizer, which scatters the beam in a solid channel such that the output is rectangular, non-coherent, and evenly distributed across the field.

At a nominal altitude of four hundred feet, the beam field of illumination of a single shot is 8.46 degrees along track, and 3.61 degrees cross track. This equates to each set of six camera images representing a rectangular area of 25.2 feet wide by 59.5 feet long. The full thirteen shot pattern represents an area 300 feet wide by 59.5 feet long. Figure 29 illustrates this projected illumination pattern.

The laser operating parameters are as follows:

Laser output wavelength	532.1 nanometers
Laser pulse repetition rate	40 Hertz
Beam diameter	7 millimeters
Beam transverse profile	Circular Gaussian
Coherence length	.66 centimeters
Beam pointing stability	56.84 microradians full angle, peak to peak
Beam divergence	1.18 milliradians full angle
Beam energy	525 millijoules/pulse
Linear beam polarization	.76 degrees off perpendicular to optical bench. Degree of polarization - 99.58%

Table 7. ML(A) laser operating parameters.

c. Receiver Subsystem

The ML(A) receivers consist of an intensified charge coupled device with readout electronics, a linear polarizer, a lens assembly, a narrow spectral bandpass filter (NBPF), and support electronics. Energy received is filtered by the NBPF so that only a narrow spectral range around the laser wavelength of 532 nanometers passes through. Other light, such as sunlight, outside the bandpass is filtered out.

The filtered light then passes through the lens assembly forming an image of the illuminated scene at the sensitive surface of the ICCD. ML(A) utilizes a 172.5 millimeter, F/1.92 lens. The lens assembly also determines the field of view for the system. The receiver field of view is 2.72 degrees by 1.78 degrees with a pixel format of

256 by 168 as illustrated in Figure 30. Pixel resolution is 185 microradians/pixel. The amplified image is read out by the associated readout electronics.

The ICCD controls the exposure of the camera. The intensifier used in the ML(A) system is a single stage Gen III intensifier tube, with a variable gain of 10 to 5000. Figure 31 illustrates the Gen III intensifier. Automatic gain control of the ICCD, exposure by exposure, maintains a constant video level presentation to the operator. Sensor dynamic range is 60 decibels.

Exposure control, or gating, circuitry controls the precise timing delay between laser firing and camera exposure, as well as the length of the exposure, or gate.

The two dimensional image from each receiver represents the laser light backscattered from a single range gate. The combination of the six receiver images from different adjacent portions of the water volume result in a three by two tiled receiver footprint, and represent an image of the illuminated area and of targets that may be contained within the search volume. An onboard computer automatically detects, classifies, and localizes mine-like objects, providing selected subimages for operator review. Figure 32 is a sensor block diagram.

d. Bottom Follower Subsystem

The bottom follower consists of the detector and associated electro-optics, along with its signal processing subsystem.

The bottom follower parameters are as follows:

Field of view	0.88 degrees (ten feet at 650 foot altitude)
Sensor rise time	≤3 nanoseconds
Detector dynamic range	60 decibels
Operating dynamic range	48 decibels
Electronic bandwidth	150 Megahertz
Filters	3 nanometer full width half maximum bandpass. Linear polarizing.
Gain	Automatic gain control
Signal Processor:	
Sampling frequency	500 Megahertz
A/D resolution	8 bits minimum
Data recorder capacity	150 Megabytes

Table 8. ML(A) bottom follower parameters.

e. Instrument Control Computer (ICC)

The instrument control computer interfaces with the image processing computer and display monitor. It also acts as the system control platform for the sensor control indicator, pilot control indicator, scanner servo, camera automatic gain control and gating, digital tape recorder, VCR, and the laser. The ICC controls the central input/output processing of aircraft data and target database management. It is also the bottom follower processor interface.

48

3. Description of Experiment

The Coastal Systems Station (CSS), Panama City , Florida, was tasked by Naval Sea Systems Command (NAVSEASYSCOM), Program Executive Office, Mine Warfare (PMO 210) to evaluate the ML(A) demonstrator system. The objective of the ML(A) program was to demonstrate a technology that can rapidly detect, classify, and localize objects in the surf zone. The CSS program is to include an extensive test and real world data collection effort based on government testing at up to four test ranges. These ranges are to display increasing degrees of clutter, obstacle, and water clarity values.

The data presented in this paper are from the first contractor test (CT-1) of the ML(A) technology demonstrator conducted at Eglin Air Force Base Gulf Test Range, Test Site A-15A on Okaloosa Island, Florida, during the period 08-14 December 1994. The test field was approximately 550 feet wide by 800 feet long, encompassing an area from sand dunes to a fifteen foot depth contour line. Targets were located in the dune vegetation and on two, five, ten, and fifteen foot water depth contour lines. The aircraft flew directly over the test field at altitudes of 400, 500, and 650 foot altitudes. The data in this report are from the 650 foot altitude pass. Simulated mines were round six inch and twelve inch bottom targets. The specified reflectance of these targets were 8% and 23% at the system wavelength of 532 nanometers. A bottom reflectance of 45% was assumed at 532 nanometers. This combination of reflectances yielded a target-to-background contrast of 0.82 for the 8% reflectance targets, and 0.49 for the 23% reflectance targets. The targets were painted olive or gray by the government to meet

these specifications. Also in the field were specified non-mine-like objects (NMLO) such as one foot by two foot rectangular objects, railroad ties, wheel barrows, and two foot circular objects, as well as resolution panels, to test the systems ability to classify detected objects accurately.

VI. OBSERVATIONS AND ANALYSIS

A. OCEAN WATER LIDAR (OWL)

Each of the three system passes analyzed here, will henceforth be referenced by its respective alphanumeric title. These titles are: D0534, D0511, and D0519. Selected plots have been chosen from each pass to illustrate a desired aspect of the observations. The data were examined on a line by line basis for each individual system pass to search for the presence of a mine-like object.

The first plot for each pass is an overview of the entire data set for a specified period of system operation. The direction of aircraft flight is along the direction of increasing row numbers. Plots for each of the system's gain settings (low, medium, and high) are arranged adjacent to each other within an arbitrarily set sample range corresponding to the set of range gates captured by the system. The thickness and darkness of the plot features are a function of the analysis program used. A thick black band is an indication that the plot is saturated, not necessarily the system instrument.

The overview plot is followed by a series of plots of selected subsets of the data. These subsets essentially allow for a magnified look at a small segment of the data. This relatively small segment, or panel, consists of one hundred and eight rows of the overview plot. Once again, aircraft direction of flight is along increasing row numbers, and plots for the three gain settings are arranged adjacently with subsets of the range gates selected to include measurements from just above the surface to beyond the sea

bottom. Panels are labeled with data alphanumeric titles followed by the row values from which the plot was selected. These row values correspond to those of the overview plot. The sinusoidal pattern of these plots is a product of the system's circular scan pattern. It is within these magnified representations of laser return that a target would first be evident if detectable by the system.

Following each panel plot is at least one line plot. These line plots represent a single row of data from within the associated panel plot as indicated in the plot's title. The plot's title indicates the alphanumeric title for the data from which it was selected as well as the specific row it represents. These line plots illustrate the return waveform intensity versus range gate values increasing to the right of the plot. The system intensity had an analog range of zero to one volt, digitized to zero to 1024 bits. The high gain channel typically saturates over a broad range of gates. Each range gate was approximately two nanoseconds. The laser pulse traveled approximately one foot, round trip, every two nanoseconds. Therefore, the approximate water depth, in feet, can be calculated by determining the number of range gates between the leading edge of the surface return peak and the leading edge of the bottom return peak, and dividing that number by two. The top subplot uses a logarithm vertical axis, the bottom subplot uses a linear scale. Low, medium, and high gain values appear congruently on each scale. If a target was detected in the panel plot, the line plot could than be analyzed for the increased intensity of laser return associated with that target.

Surface and bottom returns are distinguishable because of their steep rise times in conjunction with their high intensity values. Electronic ringing is present in some of the data sets, particularly for waveforms with strong surface returns.

The data contains variability in surface return, volume backscatter, and bottom return signals. Based on knowledge of the effects of the air/sea interface return amplitude as a function of wind speed and beam off nadir angle, and volume backscatter amplitude as a function of water clarity parameters, under normal working conditions the surface returns are a mixture of interface reflections and volume backscatter peaks. The line plots presented here show how the origin of the surface return varies depending on the dominance of these parameters. In actuality, many of the surface returns represent linear combinations of these parameters, resulting in an interface return with an initial rapid rise to some level followed by a stretched volume return.

1. Pass D0534

This set of data was collected while the aircraft was flying in a northerly direction over an area ranging from deep water toward the beach, on 07 September, 1994. A twelve meter laser spot size was used for this pass.

Figure 33 shows the overview of this pass. The dark band in the center of the plots for the different gain settings represents surface return. As the aircraft approaches the beach and, thus, transitions to shallower water, the bottom return appears on the right of the plots. As the system gain increases, the bottom return is detectable at correspondingly greater depths (earlier row numbers). The twelve meter laser spot size

illuminates a large area of the water column, and, therefore, causes a dense accumulation of laser return. This effect is observed in these plots by the darkness and thickness of the plotted return values.

Figures 34 through 50 show the system's varying return as the transition is made from deep water, to shallow water, to the beach.

Figure 34 is a plot of rows 540 to 647. The bottom can be seen in the high gain plot, and is barely visible in the medium gain plot, but has yet to become evident in the low gain plot. The system's circular scan pattern not only causes the sinusoidal shape of the plot, but also results in the return signal's apparent light and dark regions along the row axis. When the beam is received at nadir, the surface return appears darker than at angles off nadir because of the specular reflection of the laser pulse off the air/sea interface. The converse is true for the bottom return, it appears more intense at angles off nadir.

Figure 35 is the line plot for row 564. The zero range gate value of the line plots correspond to a panel plot sample value of 145 for low gain, 427 for medium gain, and 757 for high gain. The high gain values are off scale for the linear plot and barely in range for the log plot. The strong interface reflection of the surface return is seen, however, in the low and medium gain values. Bottom return is best observed in the linear plot of the medium gain values. This return is not as sharp as may be expected from the bottom because of the depth of the water sounding. The approximate water

depth for this sample is fifty feet. Figure 36 shows the panel plot for rows 1620 through 1727. In this region, the bottom is becoming more evident in the medium gain plot.

The line plots of Figure 37 not only illustrate the effects of ringing on the down slope of the surface return, but also an increase in the contribution of volume backscatter. When compared to Figure 35, the pulse width of the surface return is greater in Figure 37, indicating that the surface return has more backscatter components than strictly interface related components. Approximate water depth is forty feet.

Figure 38 shows the continuing trend of laser return with aircraft motion. Subtle features in the bottom return appear more clearly in Figure 39, where a sharper bottom return is beginning to take form in the medium gain plot.

As the bottom return becomes stronger in the low gain plots, the high gain plots become more saturated. This effect is illustrated in Figure 40, where the bottom is now very clear in the medium gain plot, faint in the low gain plot, and the high gain plot has become obscured. Figure 41 shows how there may be a sharp bottom return in one gain level, in this case medium gain, while the lower gain level reveals the lower bottom return resolution. Approximate water depth is thirty five feet.

Figures 42 and 43 illustrate the increasing waveform intensity in the various gain levels with decreasing water depth. The approximate water depth for this sample is twenty five feet.

Figure 44 shows, once again, varying waveform intensity with scan angle off nadir as well as decreasing water depth. Figures 45 and 46 are waveforms from an

approximate water depth of twenty feet that demonstrate the possibility of great bottom return amplitude variations from pulse to pulse. The difference between these figures is one of phase in the angular sweep. Figure 45 shows the strong surface return associated with laser return near nadir, while Figure 46 shows more equivalent surface and bottom return associated with laser return off nadir. In Figure 46, the high gain data are saturated for all range gates.

In water depths of less than twenty feet, the low gain level becomes the only one containing usable target information. This is illustrated in Figure 47. Decreasing water depth brings the surface and bottom return waveforms so close together that the line plots also become difficult to draw useful information from. Figure 48 shows that the down slope of the surface return has not been minimized before the upslope of the bottom return. If there were a target in the region between the surface and the bottom it would be difficult to extract target identification information from the noise associated with waveform returns in this region.

As a final illustration of the difficulties induced by the shallow water environment, Figures 49 and 50 are from an approximate water depth of twelve feet. The low gain panel plot is the only source of useable information about possible targets in this region. The line plot illustrates how the bottom return becomes the dominant feature in this region.

2. Pass D0511

This set of data was collected while the aircraft was flying in a northerly direction over an area ranging from deep water toward the beach, on 08 September, 1994. A one meter laser spot size was used for this pass.

Figure 51 is the overview for this pass. It is interpreted in the same way as the overview plot of Figure 33. The major difference between this set of data and that of D0534, is that now a one meter laser spot size is being used as opposed to the twelve meter laser spot size of D0534. The effect of using this smaller spot size is to illuminate a smaller area of the water column and allow for higher resolution of smaller targets. Unfortunately, the sweep pattern could not be adjusted in such a way as to allow complete coverage, so the one meter spot size data suffer from gaps in the sampling of the target area. While reasonable for bathymetry measurement, adjustment would obviously need to be made for a true minehunting system. This smaller area of illumination, when plotted, results in a less dense laser return plot. This decrease in laser return density results in the plot of Figure 51 having finer and more faint lines than Figure 33 indicating the surface and bottom returns.

Figures 52 through 58 highlight portions of the pass to illustrate, once again, aspects of the system operated over areas with water depths ranging from off shore to the beach. Figures 52 and 53 show the occurrence of bottom return in the high gain plot, while it is still not detectable in the medium or low gain plots. The one meter spot size results in the surface return plots of this panel not being as wide or as intense as those of

the D0534 data. Figure 53 is the line plot for row 545. When compared to the line plots of D0534, this line plot has sharper rise times due to the decreased laser spot size of D0511. These sharper rise times allow for more accurate spatial determination of the surface, the bottom, and any possible targets located between the two. These plots, however, also indicate the presence of more noise in the signal. This increase in noise is due to the fact that the narrower beam experiences more effects of the sea surface scattering the light out of the receiving element field of view. The zero range gate value of the line plots correspond to a panel plot sample value of 130 for the low gain plot, 412 for the medium plot, and 742 for the high gain plot. The approximate depth of the water in this region is thirty five feet. The twelve meter laser spot size of D0534 allowed for bottom detection at depths of approximately fifty feet.

Figure 54 shows the bottom return as it starts to become visible in the low gain plot. As expected, it is already quite strong in the medium and high gain plots. The line plots for row 2762, in Figure 55, show the strong bottom return associated with a region approximately twenty feet deep. Again, the noise in this region is accentuated in the medium and low gain plots, but so too are the short rise times of the surface and bottom returns. As previously stated, this shorter rise time indicates an increase in the system's ability to resolve (detect) smaller objects.

As a final illustration of the system's use as a tool with which to search the bottom in a shallow water region, Figure 56 shows the intense bottom return associated with this region when using the one meter laser spot size. More separable surface return

intensities are also illustrated which indicate that if there was a target in this region, the probability of detecting it would be greater than if the twelve meter laser spot size were used.

Figures 57 and 58 illustrate the variability in bottom return between pulses as well as the noise associated with exploiting the shallow water region optically. Within this region, the amplitude of the bottom return becomes consistently greater than the amplitude of the surface return. The approximate water depth in this region is between five and ten feet.

3. Pass D0519

This set of data was collected while the aircraft was flying in a westerly direction parallel to the shoreline on 08 September, 1994. The water depth remained consistently between five and ten feet. A one meter laser spot size was used for this pass.

Figure 59 is the overview plot for this pass. This plot is interpreted in the same way as the previous overview plots with the exception of the observance of the bottom return as a feature that comes in slowly from the right side of the plot. In D0519, the surface and bottom returns are intertwined throughout the entire extent of the rows plotted. In the region between row two thousand and row four thousand, the surface and bottom returns become more separable from each other presumably because of a change in the bottom contour.

Figure 60 is a panel plot of rows 3240 through 3347. Although the overview plot of Figure 59 indicates a surface and bottom return that may be separable in this region,

Figure 60 shows that this remains difficult in a shallow water environment. Figure 61 is the line plot for row 3258. The zero range gate value of the line plots correspond to a panel plot sample value of 140 for the low gain plot, 472 for the medium gain plot, and 752 for the high gain plot. In order to better facilitate the ability to distinguish the plots for the various gains, the medium gain plot is indicated by a line with dots at the data values. This figure illustrates the weak surface return, and strong bottom return associated with the shallow water region. Also noticeable, is the high noise associated with this region.

Figures 62 and 63 are provided to further emphasize the strong bottom return characteristic of this set of data. The line plot for row 4249 in Figure 63 illustrates the near absence of a surface return as, in this region, bottom return clearly dominates.

B. MAGIC LANTERN ADAPTATION [ML(A)]

Figures 64 through 68 are plots of data collected from one of the ML(A) test flights conducted at the Eglin Air Force Base Test Range in December, 1994. The flight shown here was flown at an approximate altitude of 600 feet, heading east , parallel to the shore line. It was difficult to compare the flight results with ground truth; however, the water depth searched is known to be between five and fifteen feet.

Figure 64 is an overview of the data taken as the aircraft moved along its search path. Five full system scans are plotted as rows along the axis of aircraft motion. The numbers along the scan axis represent the number of the tiled footprint of the six cameras, starting from the number along the aircraft motion axis. Each individual square

represents the image from a single camera. There are fifteen of these tiled scan patterns per row. The dark footprint at either end of each row represents the two dead pulses per system sweep. The dark bands that appear consistently in the bottom of the camera images along the right side of each tiled footprint were caused by a misalignment that existed between the transmitter and receiver during this system test.

Upon close examination of Figure 64, a target can be seen to appear in rows two and three (marked on the vertical axis by the beginning scan numbers 20 and 35 respectively). In row two, the image for scan twenty six shows a target in the upper left square of the two by three system footprint. This square will be referred to as that representing the image for camera two. In row three, the image for scan forty one shows a target in the middle left square of the two by three system footprint. This square will be referred to as that representing the image for camera four. These two images are of the same target being imaged by different cameras in different scans as the helicopter moves along its search path. The target appears as a dark spot on a relatively lighter background because of the difference in reflectivity of the target as compared to the sand on which it lays.

Figure 65 illustrates the two by three footprint of scan twenty six. This figure more clearly shows the target in the upper left square for camera two. In actual system operation, this is the image that would be presented at the operator station's viewing monitor.

Figure 66 illustrates the two by three footprint of scan forty one. Once again, the target appears clearly in the middle left square representing camera four. The smaller black spot to the right of the target image is an artifact caused by a bad pixel in the receiver.

Figure 67 shows the single camera image of scan twenty six containing the target. The line plot shows pixel intensity values for one of the rows that contain the target, in this case, row 130. The target can be located in the line plot by locating the area of minimum pixel value.

Figure 68 shows the single camera image of scan forty one containing the target. As in Figure 66, the bad pixel can also be seen. The line plot is interpreted in the same way as that for Figure 67.

VII. SUMMARY

The data presented here are from systems that are vastly different in the form of the output presented to the operator, but identical in the physical parameters and effects of the environment that need to be addressed when designing an airborne laser system to search a designated water volume.

The analysis of the data from the Ocean Water Lidar system used a computer program that allowed for stepping through the data one line at a time. Three sets of data from three separate flights were examined in this manner. The panel plots consisting of one hundred and eight rows were first examined visually for the possible presence of a mine like object. The individual lines of that panel were then examined one at a time to look for possible evidence of a target within the line plots. No obvious targets were detected through this analysis. The one meter laser spot size presented a clearer panel plot for investigation, and sharper rise times of the returns in the line plots. There was, however, a loss in depth penetration with a decrease in laser spot size. The twelve meter laser spot size data demonstrated a strong bottom return at depths up to approximately fifty feet, while the one meter laser spot size did not give a strong bottom return until the water depth decreased to approximately thirty five feet.

The Magic Lantern Adaptation data were analyzed in a similar manner. The data output was in the form of actual images that needed to be arranged in the proper scan footprint format. Once each tile of six images was properly arranged, each image was

examined individually for the presence of a mine like object. Numerous targets were detected, and a representative example of these were chosen to be illustrated in this paper.

The most obvious obstacle to the illumination of targets in the water by an airborne system is the need to overcome the effects of the air/water interface. The advantage of observing the data collected by the Ocean Water Lidar system, is that it presents the opportunity to examine a raw waveform as it is collected by an optical receiver. It is in this way that a true appreciation of the interface effects on the surface return can be realized.

As a fully time resolved system, Ocean Water Lidar also allowed for the observation of varying environmental effects on a received waveform. Any lidar system will have to overcome these effects, or at least account for them, as an attempt is made to image objects in shallow water regions. Neither vertical nor horizontal water homogeneity can be assumed, and water clarity data should be obtained for as close to actual operating conditions as possible.

Along with water surface and water volume effects, variability in the characteristics of the bottom is significant. Differing bottom conditions yielded differing bottom returns in the ML(A) data. Often, it is within this region close to the bottom that a target will most likely lay. If this target is to be detected accurately, its return must be distinctly differentiable from that of the bottom.

Parameters such as the air/water interface, environmental effects and water volume effects are difficult to deal with even in deep water lidar applications. As these systems search for their place in exploiting the littoral environment, these effects become greatly accentuated. It will never be possible to eliminate these effects fully, but by observing them and being aware of their existence it will be more likely that they can be accounted for properly, thus reducing their detrimental impact on possible target detection.

VIII. CONCLUSION

The proliferation of highly destructive sea mines by emerging military forces has underscored the need for an effective, accurate, and rapid mine detection system. Of particular interest are minehunting systems that utilize airborne or satellite platforms since they offer the potential of rapid assessment. This thesis analyzed data from two minehunting systems that utilized lidar techniques to search a water volume from an airborne platform: the Ocean Water Lidar (OWL) system, and the Magic Lantern Adaptation [ML(A)] system.

Ocean Water Lidar is a fully time resolved system that allows for a search of a large volume of water. The entire waveform received from the laser pulse used to search this volume offers a potentially high vertically resolved view of targets within this volume. The problem in analysis is to locate fluctuations in the signal that correspond to bright or shadowed returns, rather than the many environmental factors. Range gated images are needed, and adaptations in the gating system such as those employed by ML(A), are the obvious next step.

Magic Lantern Adaptation is a system specifically designed to image targets in the shallow water environment. It is still subject to all the environmental vagaries common to all other lidar systems. It is unique in that it provides a "snap-shot" of a potentially high spatial resolution image at a specific depth. The data presented here, for the area searched on the day of the system test, show that it can obtain highly resolved

images of targets merely six to twelve inches in diameter. The system, however, would benefit from the addition of range-gated images from multiple depths (a characteristic of the other Magic Lantern variants).

The system was tested again off the coast of Southern California in August, 1995. I was able to participate in this test as an observer. The large number of particulates suspended in the waters of this coastal region on the day I was present apparently degraded system performance. An important, if somewhat obvious, lesson is that optical systems are not well suited to highly turbid littoral regions.

The job of minehunting is not an easy one no matter what technique is used. The ability to use an airborne platform offers the advantages of high area coverage rate, relative covertness, and real-time, over-the-horizon data transfer and data processing. The search for the most effective means to accomplish this task, however, should not be directed toward the expectation that a single system will be the panacea. Rather, minehunting systems should be considered analogous to tools in a tool box. The right one must be chosen to accomplish the job at hand effectively under the conditions which present themselves at that moment, both OWL and ML(A) could each potentially find their place in this minehunting tool box.
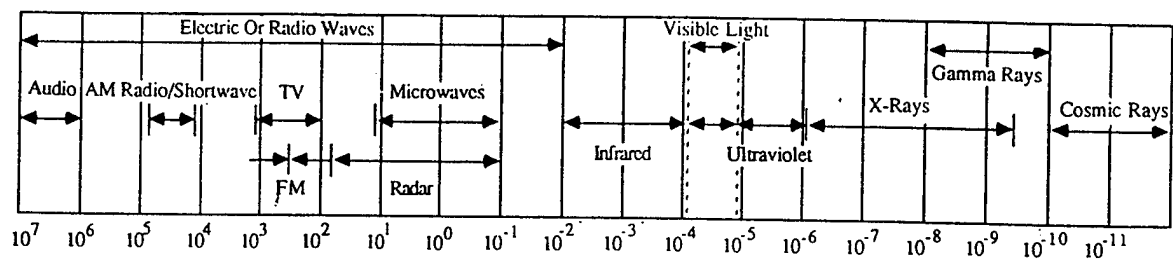
Figure 1: The electromagnetic spectrum, from long wavelength audio and AM radio signals to ultra-short gamma and cosmic rays. The visible band is a relatively small section of the spectrum. (Laurence, 1986)
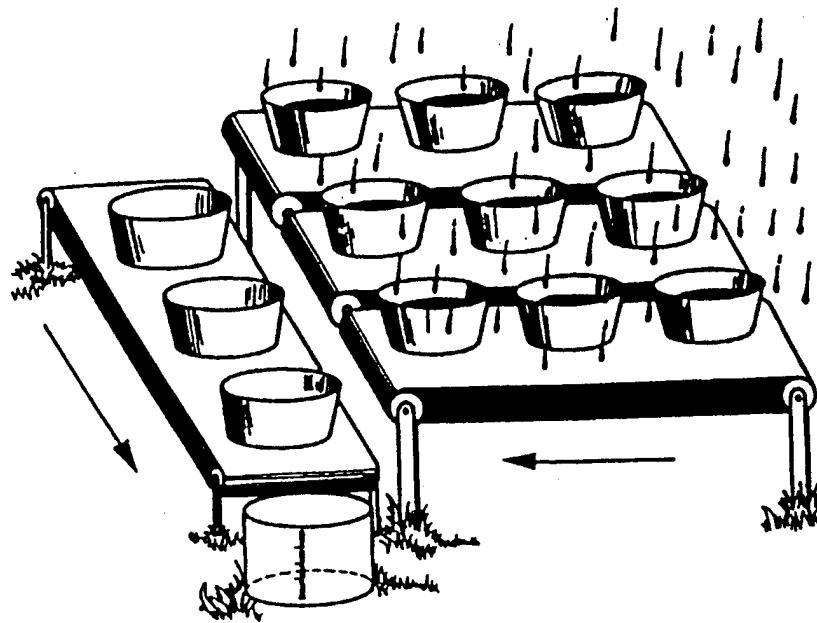
Figure 2: An analogy often used to explain how a CCD operates. A 3x3 bucket (pixel) array is shown with vertical and horizontal conveyor belts (CCD registers) that transfer water(electrons) to a measuring device (amplifier). (Janesick, 1995)

$$P_R = \frac{P_T}{R^2\Omega_T}\ (\rho A_r)\ \frac{A_c}{R_R^2\Omega_r}\ \eta_T\eta_R$$

$$A_c < R^2\Omega_r$$

$$\Omega = AREA/RANGE^2$$

WHERE

P_R = RECEIVED POWER

P_T = TRANSMITTED POWER

ρ = TARGET REFLECTANCE

A_r = TARGET AREA

A_c = RECEIVER CLEAR APERTURE AREA

Ω_T = TRANSMIT SOLID ANGLE BEAMWIDTH

Ω_r = TARGET SOLID ANGLE SCATTERED BEAMWIDTH

η = ONE-WAY SYSTEM TRANSMITTANCE

RANGE = R

(E_T) TRANSMITTER

(E_R) RECEIVER

Ω_T

Ω_r

TARGET IRRADIANCE

$(\frac{w}{m^2})$ AT RANGE, R, IS $\dfrac{P_T\,\eta_T}{\Omega_T R^2}$

POINT TARGET

TARGET RADIANT INTENSITY (w/sr) IS $\left(\dfrac{P_T}{\Omega_T R_R^2}\right) A_R\,\rho$

IRRADIANCE AT RECEIVER IS $= \dfrac{REFLECTED\ POWER}{\Omega_r R_R^2}\ \eta_R$
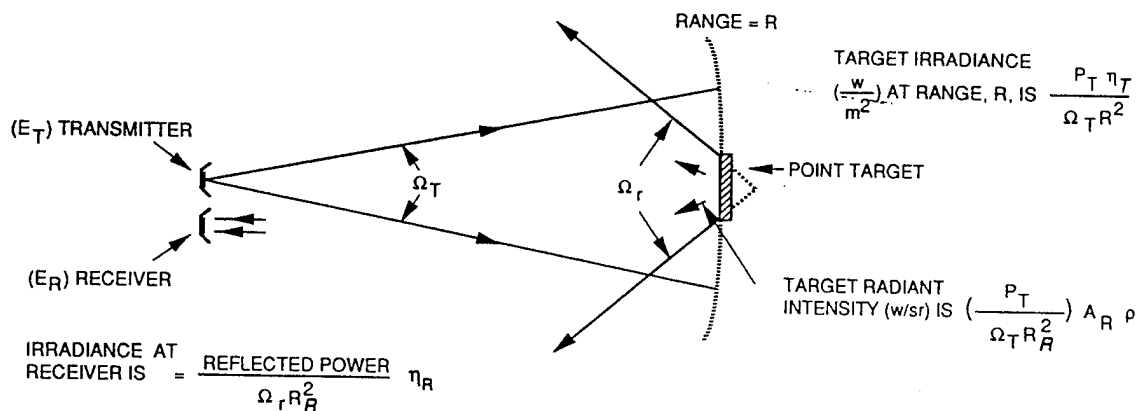
Figure 3. The laser range equation. (Jelalian, 1992)
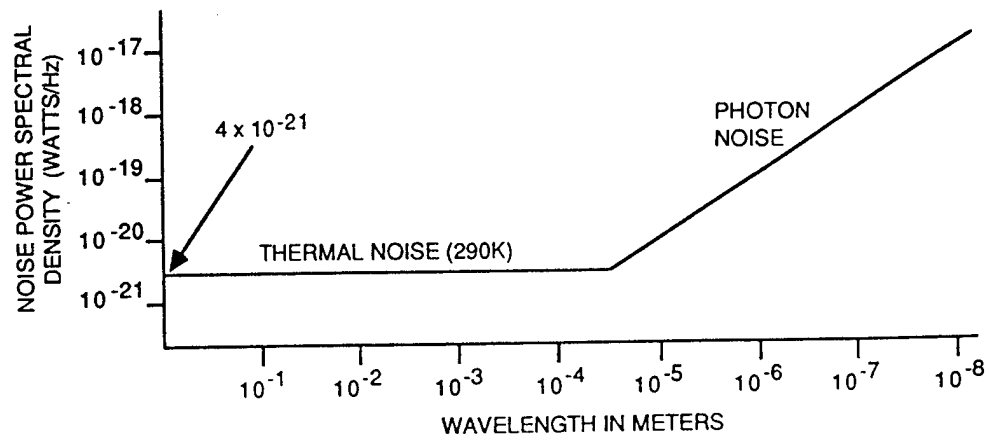
Figure 4: Plot of noise power spectral density versus wavelength.(Jelalian, 1992)

Properties/characteristics		Optical	Acoustical
Physical	Wavelength	450nm–550nm Blue–green transverse wave	1MHz–>100kHz 2 to 15mm (longitudinal wave)
	Speed	~ 225000 km/s	~ 1,5 km/s
	Air/water impedance break	Weak (T90° ~ 98%)	Strong
Technical	Energy per pulse for a typical transmitter with the resolution length $l = c\tau / 2 \sim 1m$	1Mw; 10ns → 10mJ	1Kw; 1,3ms → 1,3J
	Beamforming or directivity	Natural, 2D $\theta \sim \lambda/d < 5.10^{-6}$rd	Electronic, 1D usually $\theta \sim \lambda/d < 5.10^{-3}$rd
	Coherence	Average, (today, not in the future)	Good
	Usable bandwidth on carrier	Wide : several GHz	Narrow : several 10 kHz
Medium and target	Attenuation	Variable: 5 to .2dB/m ($c>0,03m^{-1}$) + scattering effects	~ 60dB/km at 200 kHz
	Homogeneity of refractive index	Undoubtedly	No
	Target	Point target if lobe is narrow Specular, lambertian, polarization effects	– Distributed target – Specular

Figure 5: Comparison between HF acoustical and optical underwater detection. (Kervern, 1992)
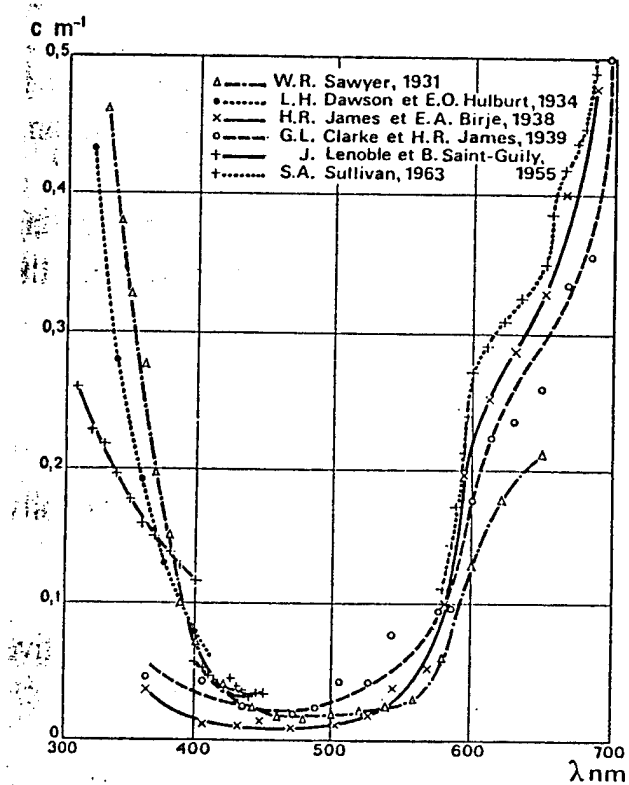
Figure 6: Attenuation coefficient for pure filtered water. (Kervern, 1992)
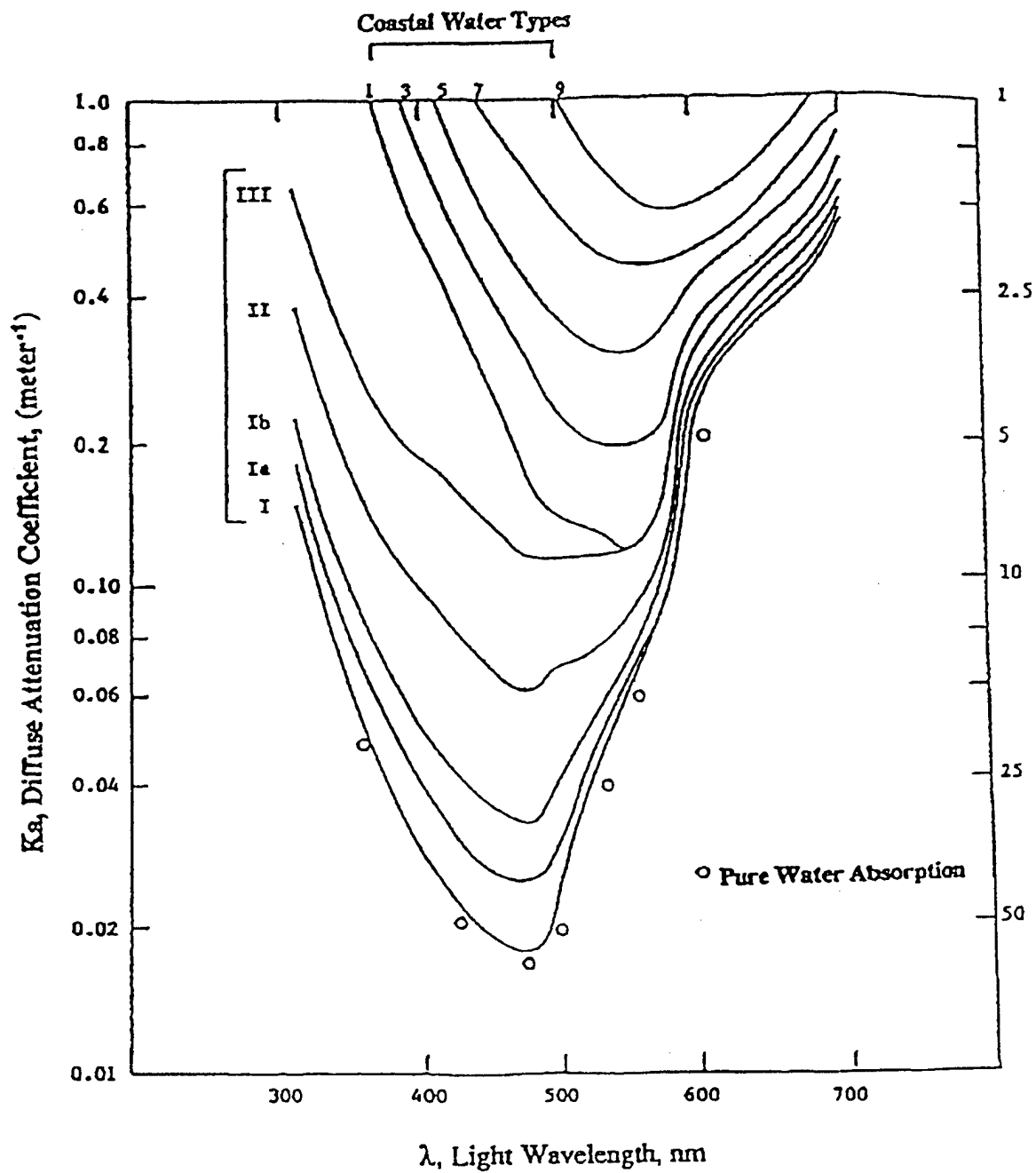
Figure 7: Diffuse attenuation coefficient for different water types. Especially note the appreciable increase in coastal areas.(Keeler, 1994)

Volume Backscatter Coefficient (San Nicholas Island)

11 August, 1995   Time: 0823

Beta(170) for 532nm (e–4m–1sr–1)

Depth(meters)
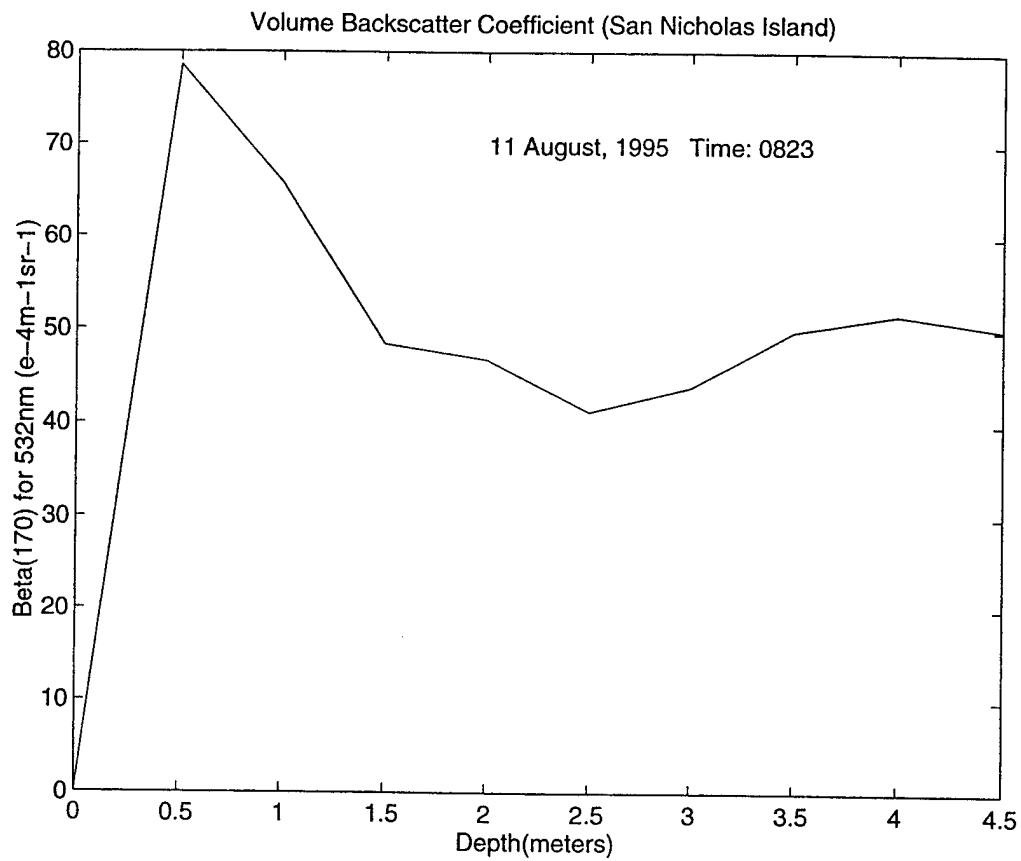
Figure 8: Plot of values received from CSS, Panama City, Florida, for the coastal region of San Nicholas Island off the Southern California coast. Note this survey was done in the early morning hours.
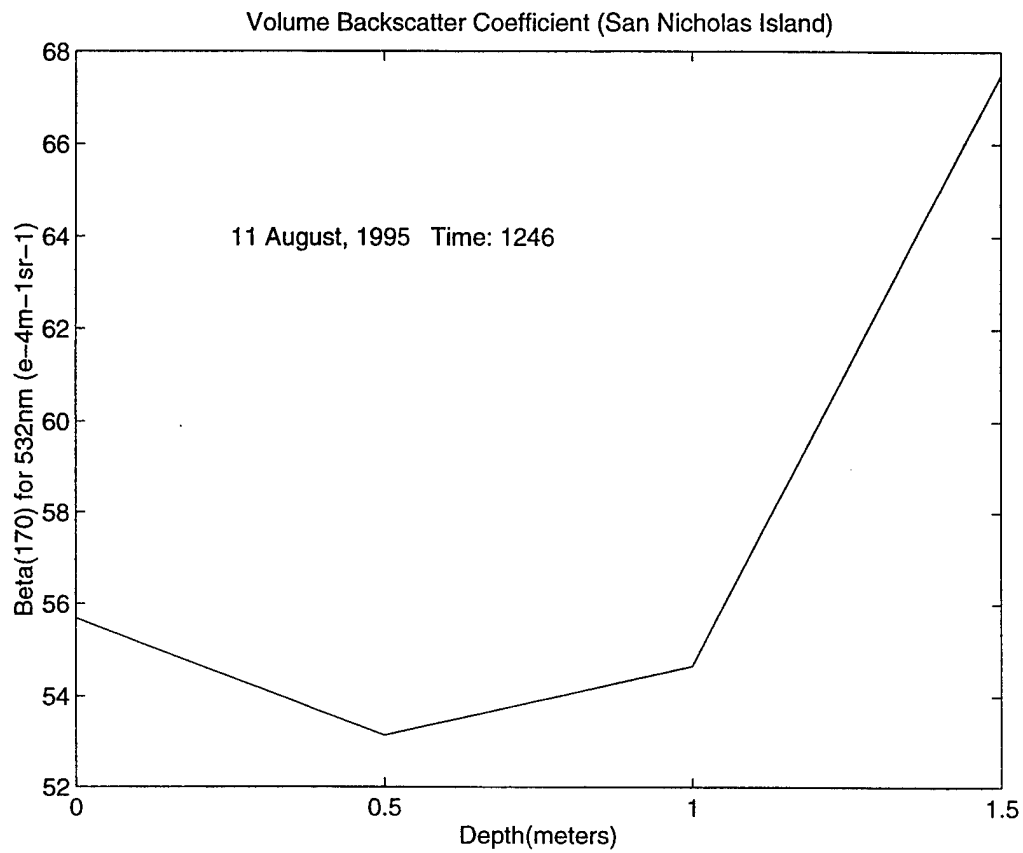
Figure 9: Plot of values received from CSS, Panama City, Florida, for the coastal region of San Nicholas Island off the Southern California coast. These values from early afternoon reveal the effects of tidal transport of particulates to the coastal regions of California.
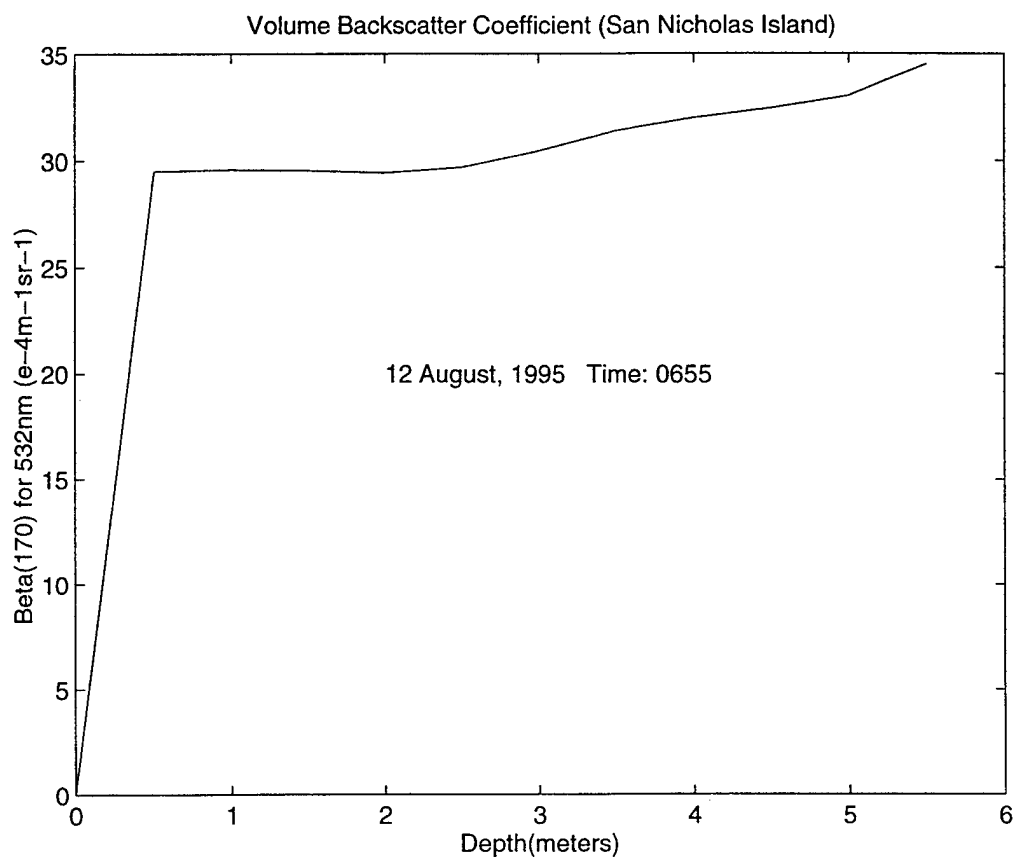
Figure 10: Plot of values received from CSS, Panama City, Florida, for the coastal region of San Nicholas Island off the Southern California coast.

Volume Backscatter Coefficient (San Nicholas Island)

12 August, 1995   Time: 1108

(x-axis: Depth(meters); y-axis: Beta(170) for 532nm (e−4m−1sr−1))
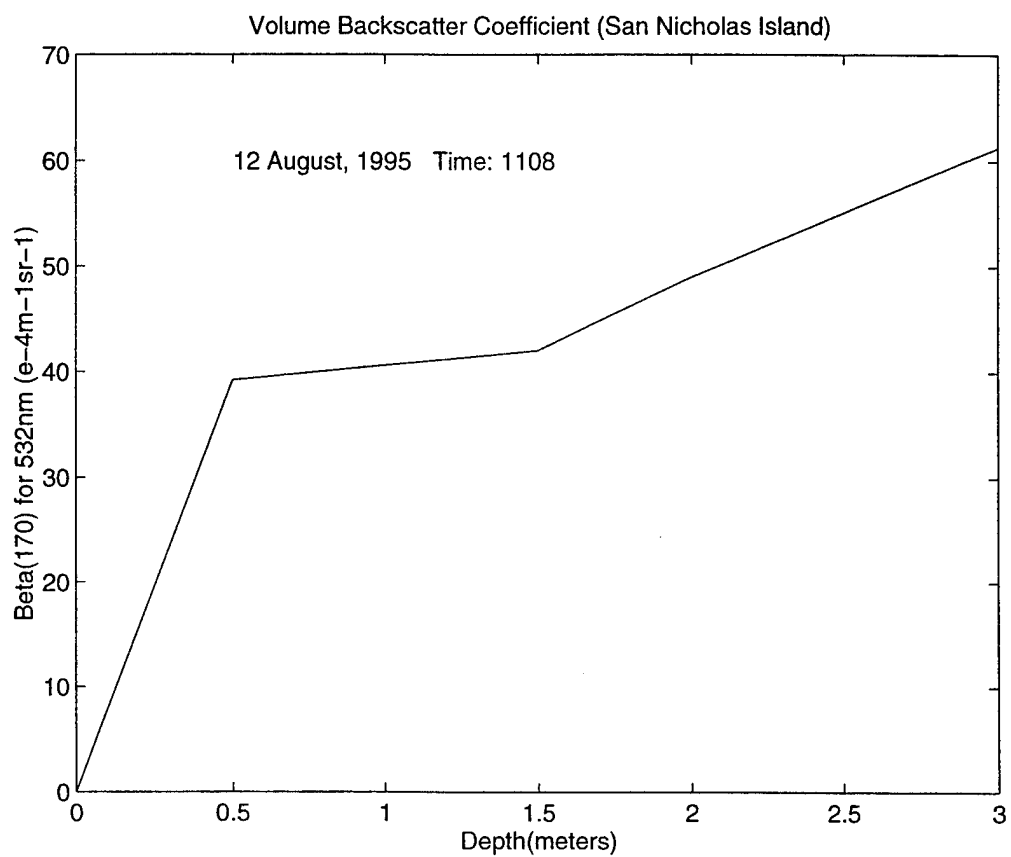
Figure 11: Plot of values received from CSS, Panama City, Florida, for the coastal region of San Nicholas Island off the Southern California coast.
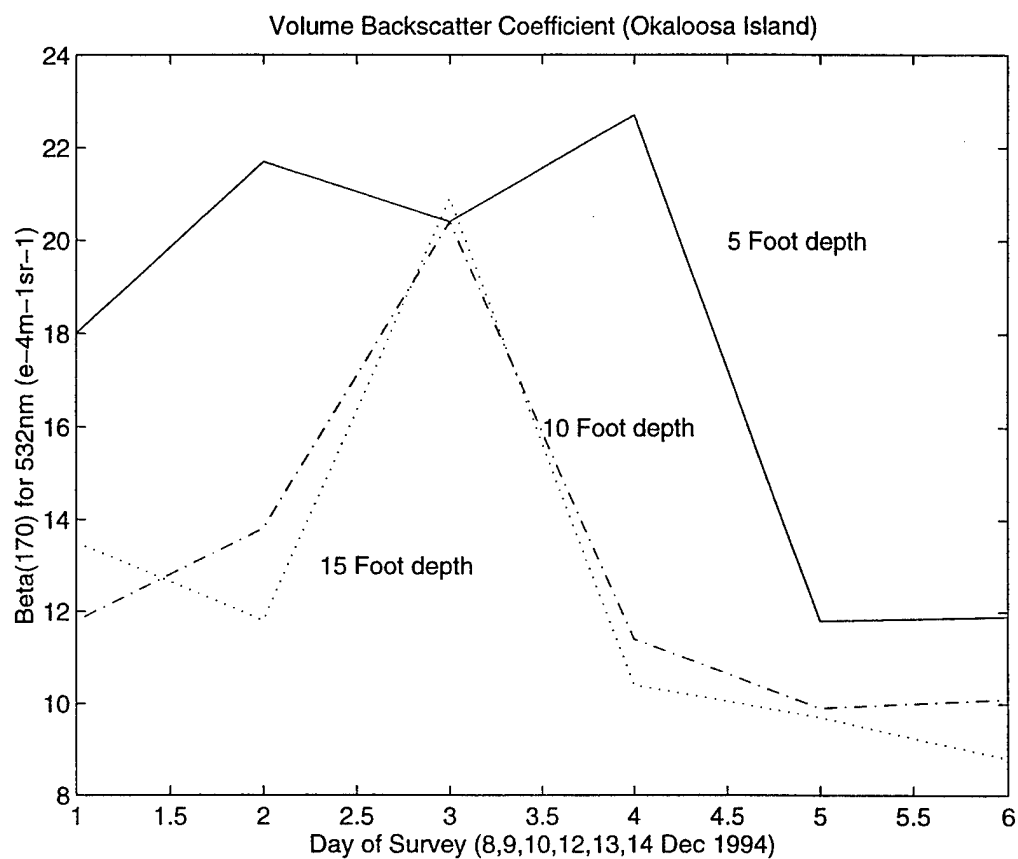
Figure 12: Plot of values received from CSS, Panama City, Florida, for the coastal region of Okaloosa Island off the Northwest Florida coast.
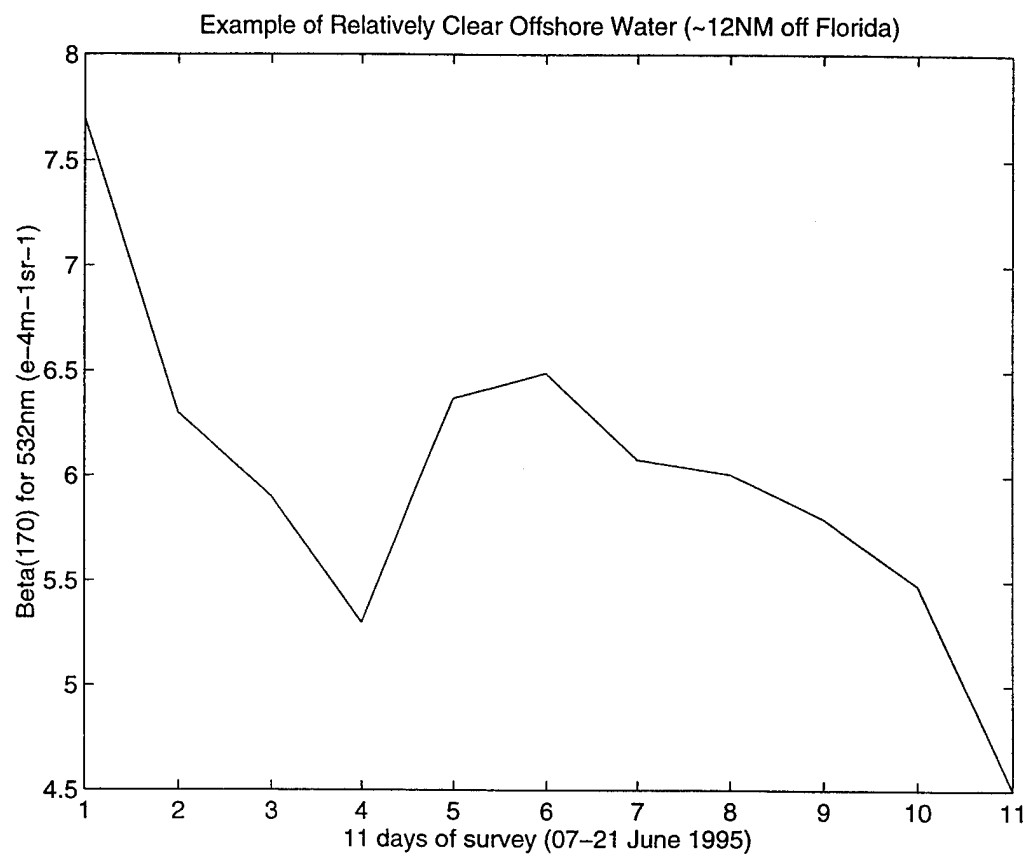
Figure 13: Plot of values received from CSS, Panama City, Florida, for the offshore region of the Northwest Florida coast. These values are from approximately twelve nautical miles off shore.
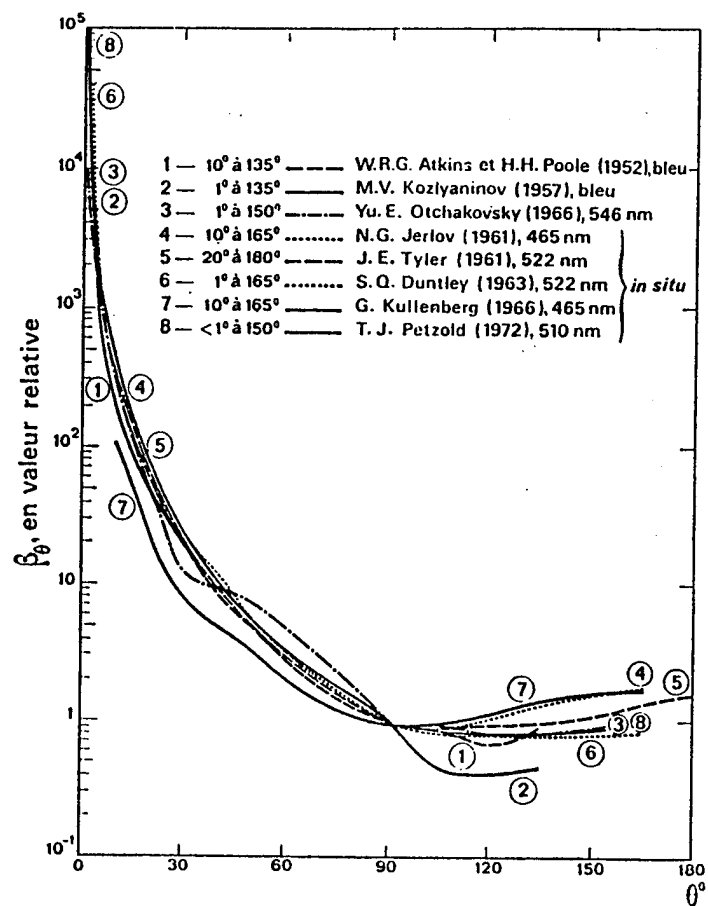
Figure 14: Example of volume scattering function normalized to θ = 90 degrees (Kervern, 1992)

82
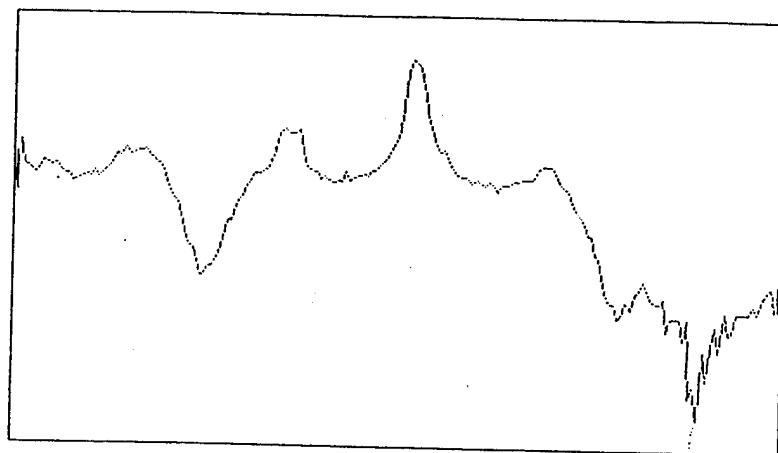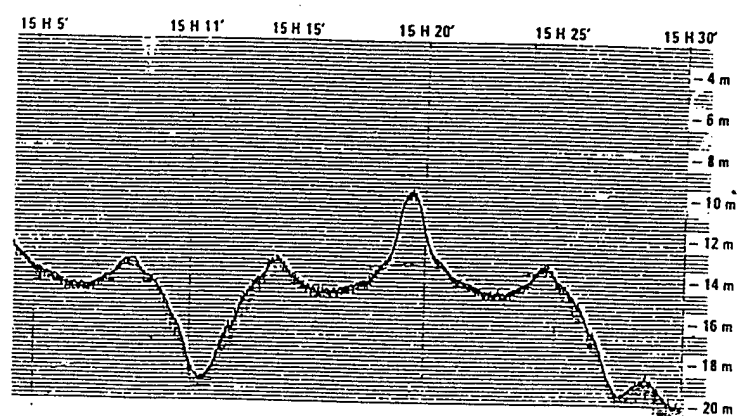
OPTICAL SURVEY

ACOUSTIC SURVEY

Figure 15: Comparison of optical and acoustic surveys of Cameret - November 1986. (Kervern, 1992)
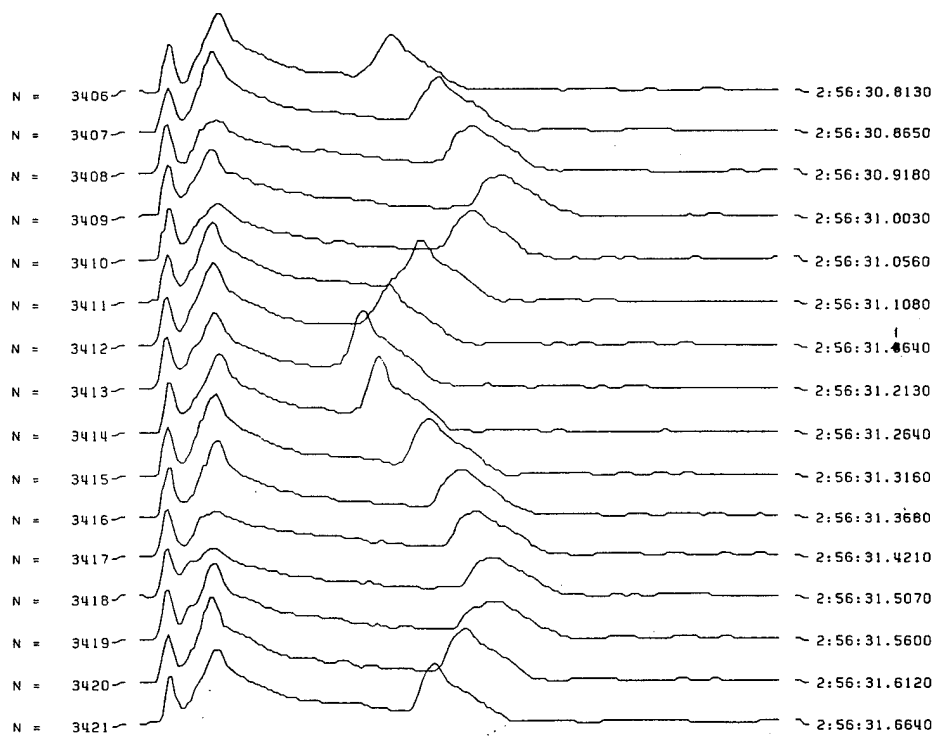
Figure 16: Sample lidar waveforms from the Canadian Larsen 500 system. (Banic, 1986)
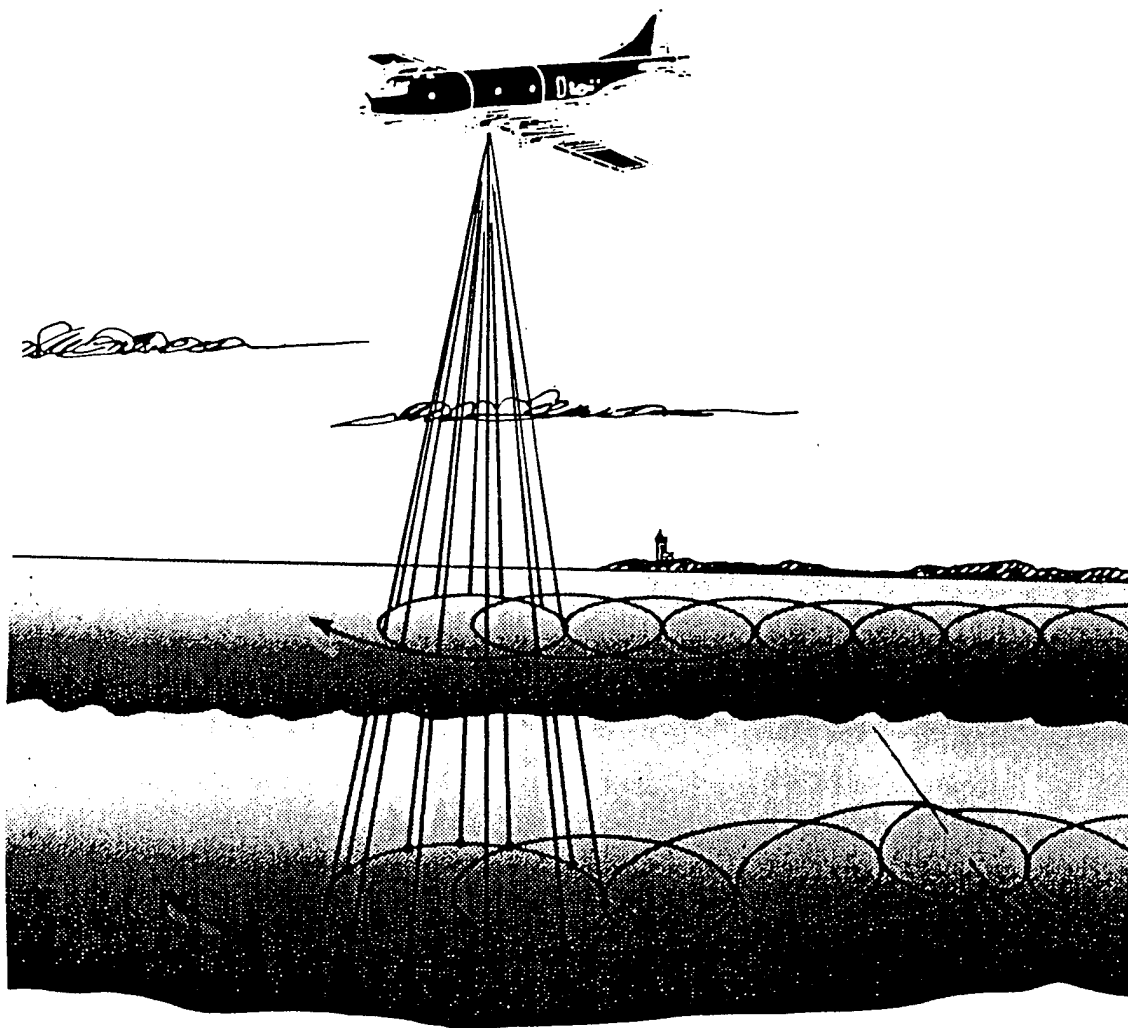
Figure 17: Conceptual system diagram of a laser scanner similar to that of the OWL system. The laser is fired in a circular scan pattern to search the water volume. (Curran, 1988)
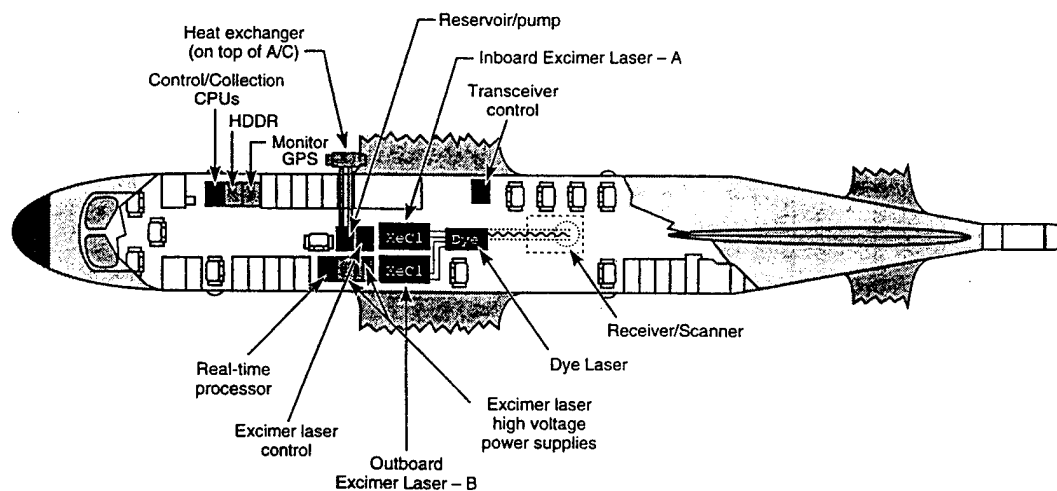
Figure 18: Layout of lidar equipment in the P-3A aircraft. Extensive modifications were necessitated for installation of system equipment. (Pacific-Sierra Research Corporation, 1995)
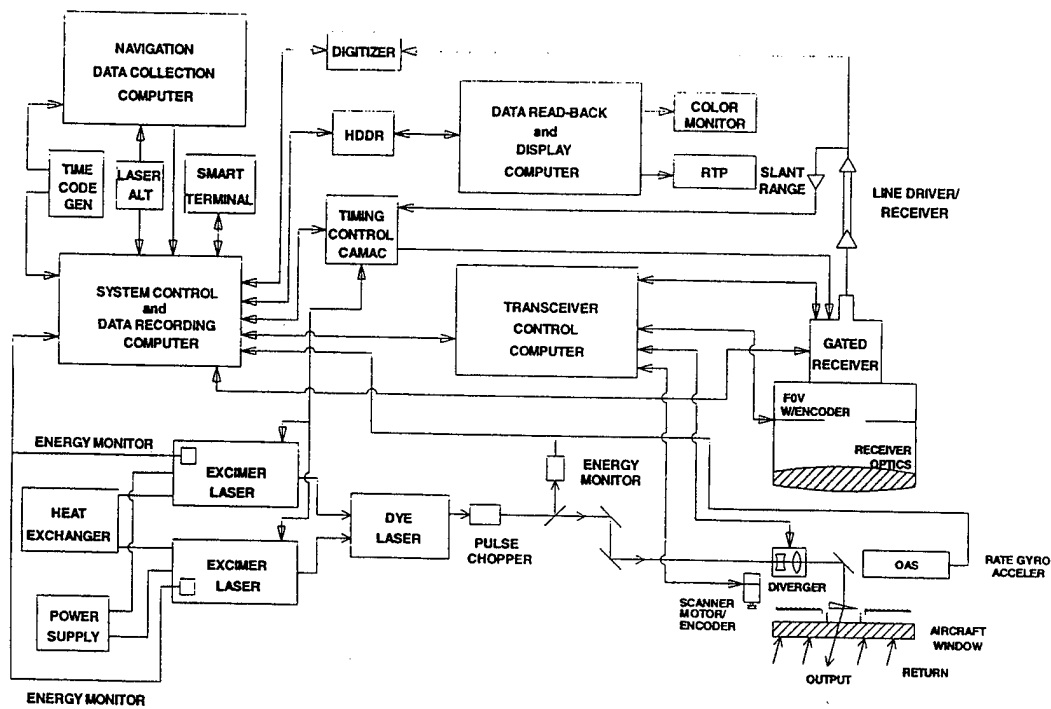
Figure 19: Ocean Water Lidar system block diagram. (Pacific-Sierra Research Corporation, 1995)

PMT HOUSING

RECEIVER
TELESCOPE

XeCl
EXCIMER LASER

DYE LASER

A

MIRROR
1

AIRCRAFT FLOOR

BLUE MONITOR

SIDE VIEW

MIRROR
2

DIVERGER   MIRROR
3

OAS SENSOR PACKAGE

LENS 1

LENS 2

TRANSMITTER OPTICAL WEDGE
RECEIVER
FRESNEL WEDGE

AIRCRAFT
WINDOW

B
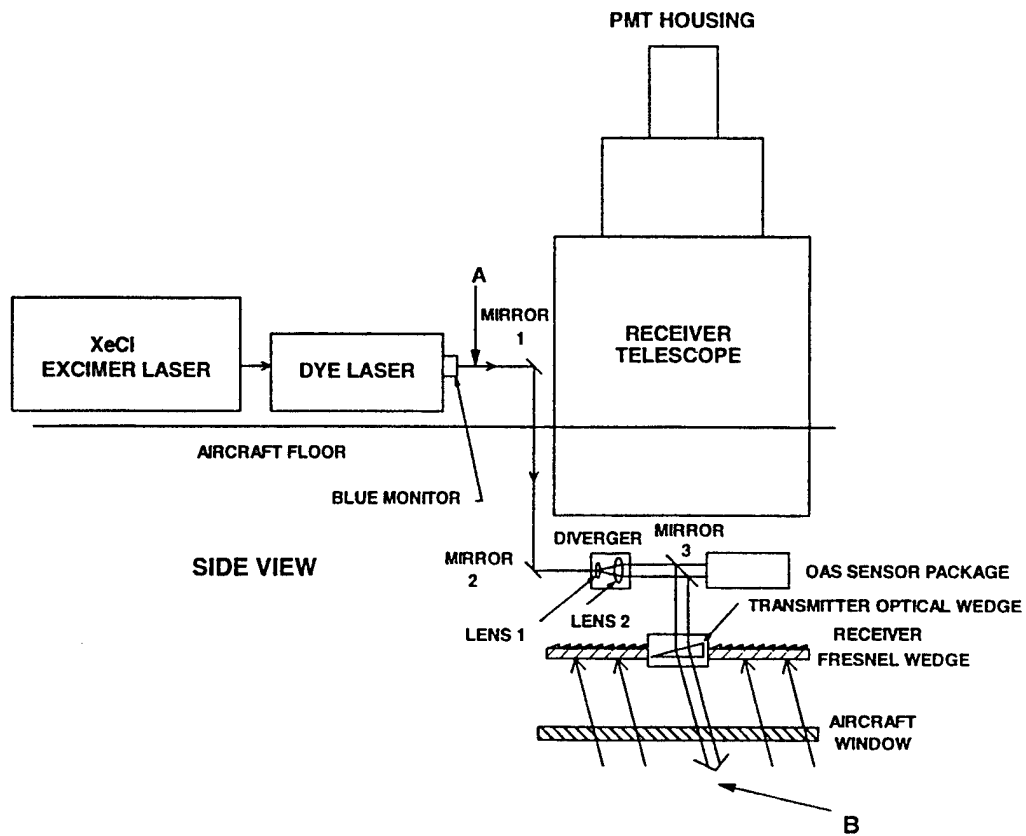
Figure 20: Block diagram of the transceiver system for Ocean Water Lidar. (Pacific-Sierra, 1995)
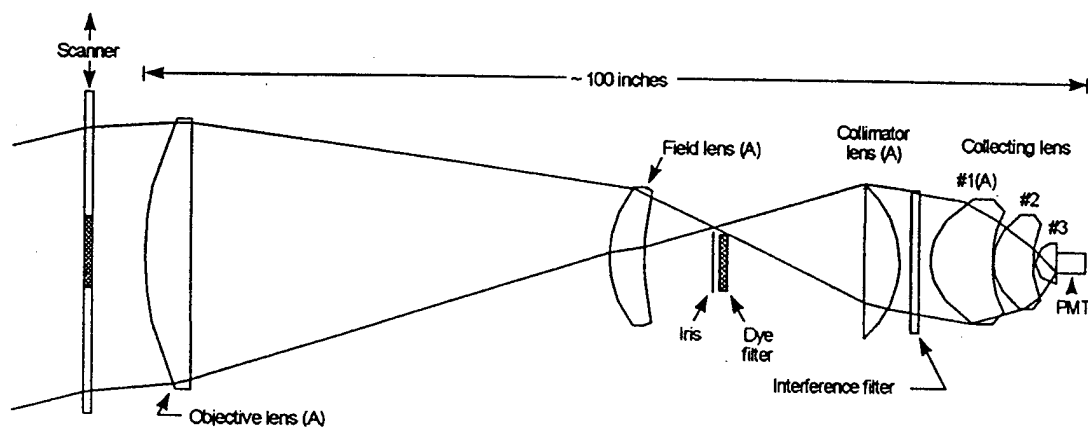
Figure 21: Diagram of the Ocean Water Lidar system's receiver optical train. (Pacific-Sierra, 1995)
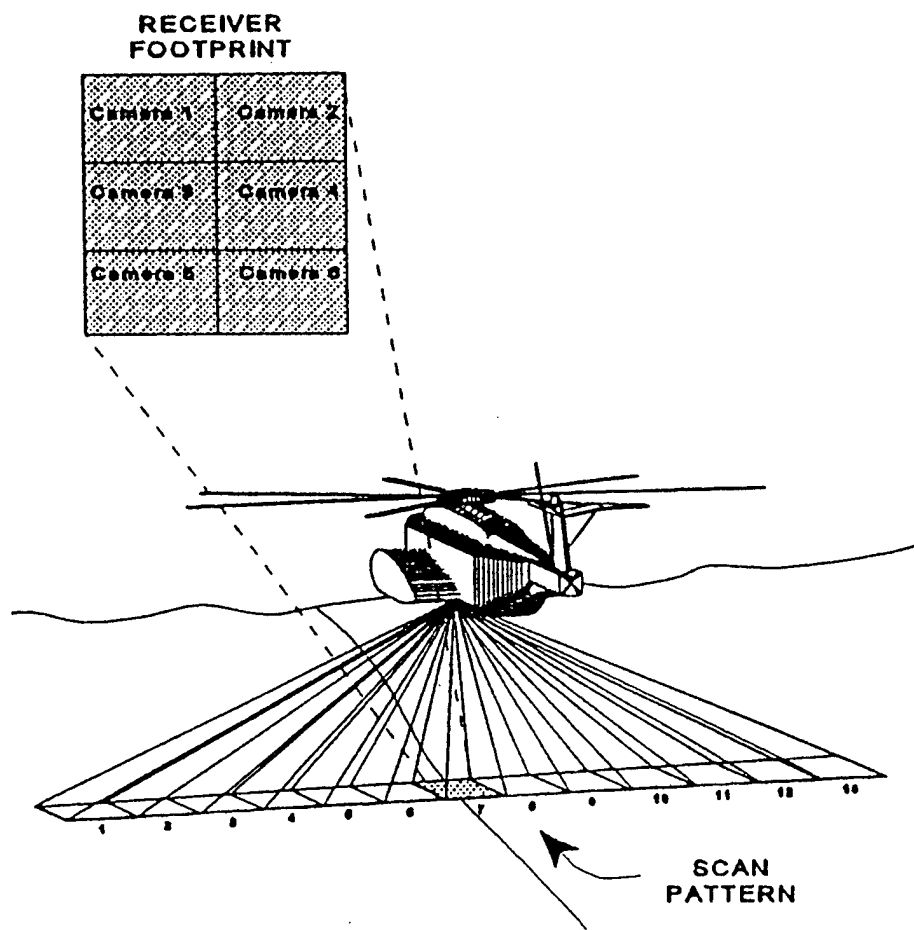
Figure 22: Conceptual diagram of the Magic Lantern Adaptation [ML(A)] system. (CSS, Panama City, 1995)
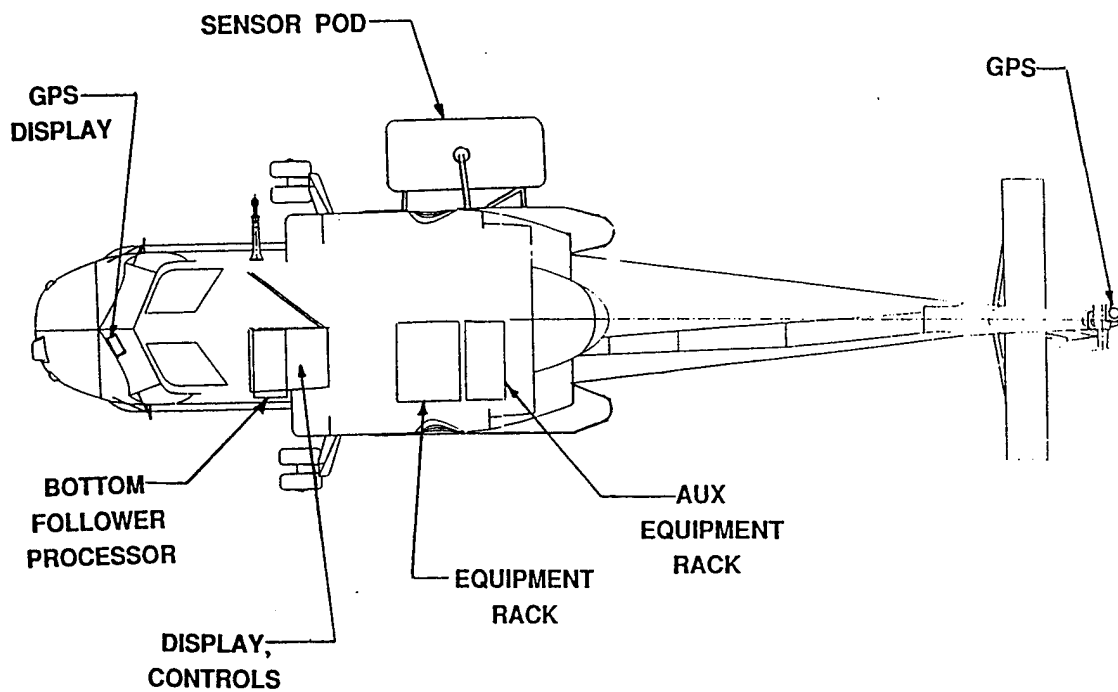
Figure 23: Layout of ML(A) system installed on board an SH-2F helicopter. (Kaman, 1993)
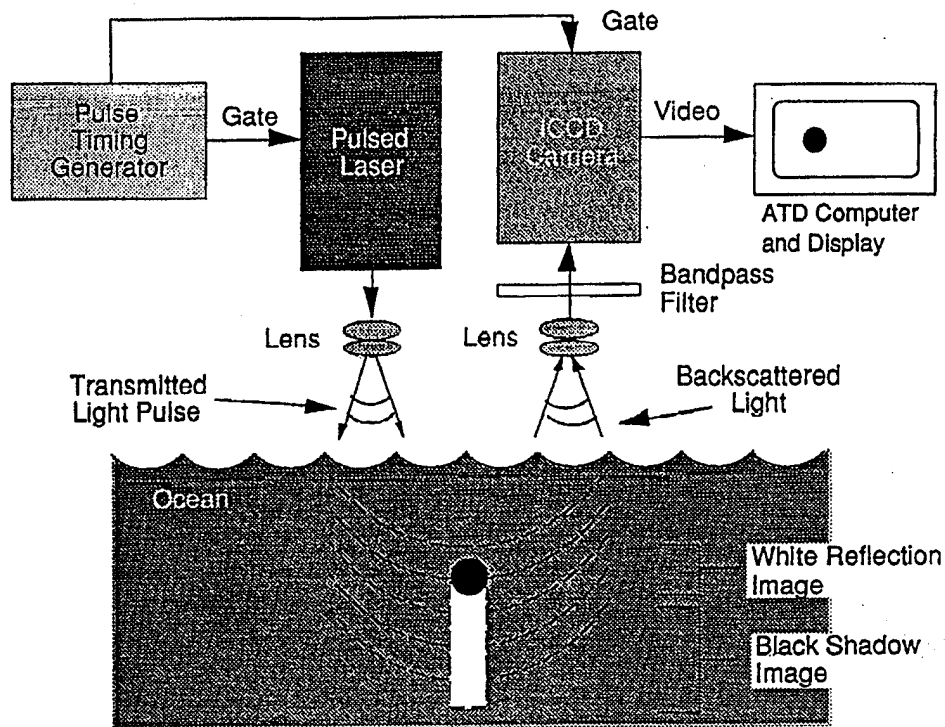
Figure 24: Magic Lantern functional diagram. (Kaman, 1993)
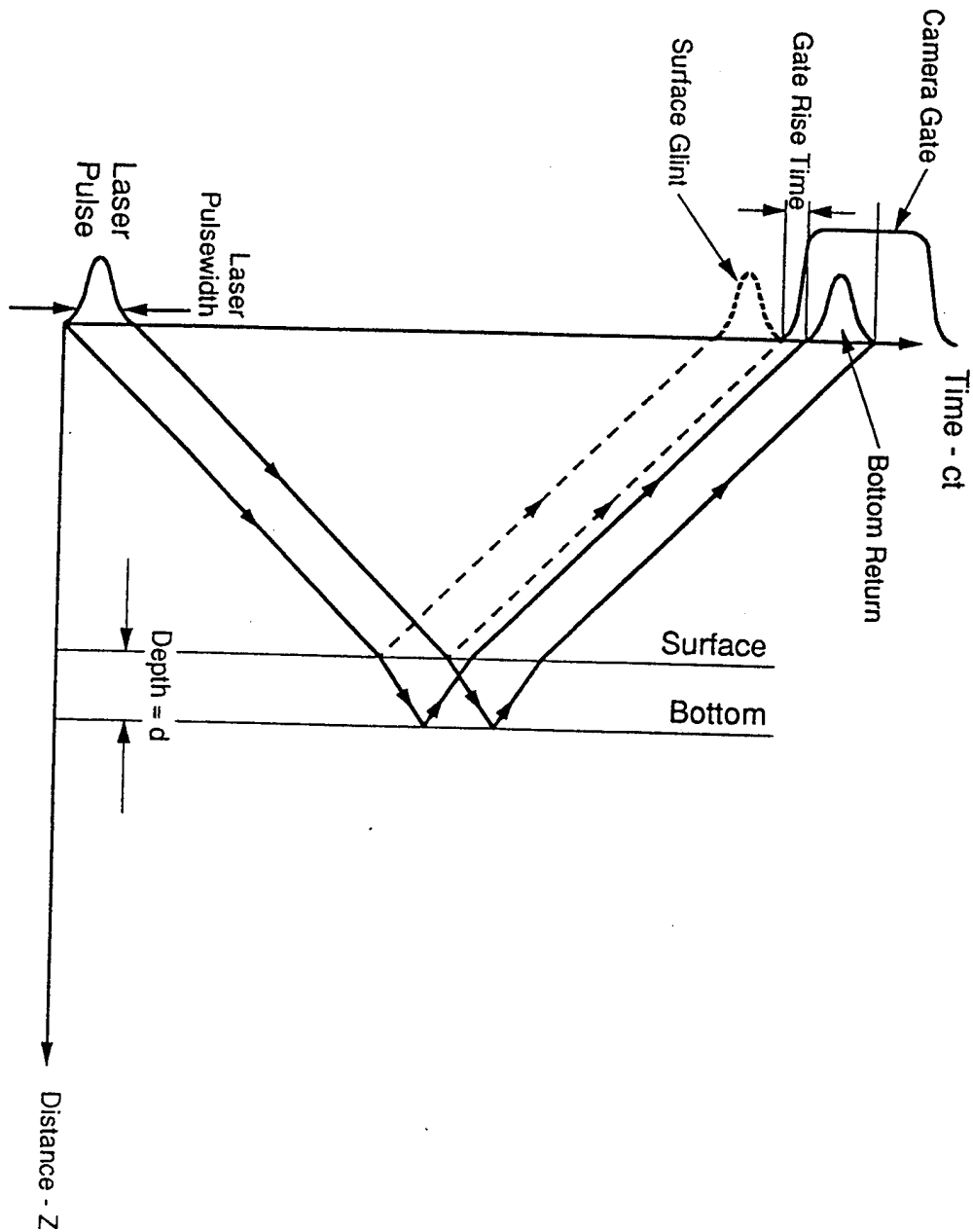
Figure 25: Imaging lidar space-time diagram. (Kaman,1993)
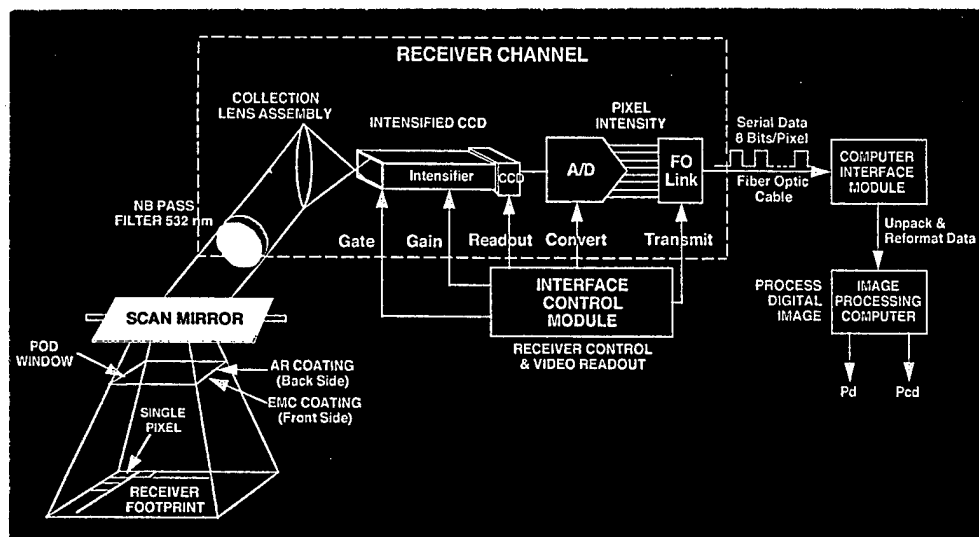
Figure 26: ML(A) receiver light path. (Kaman, 1993)
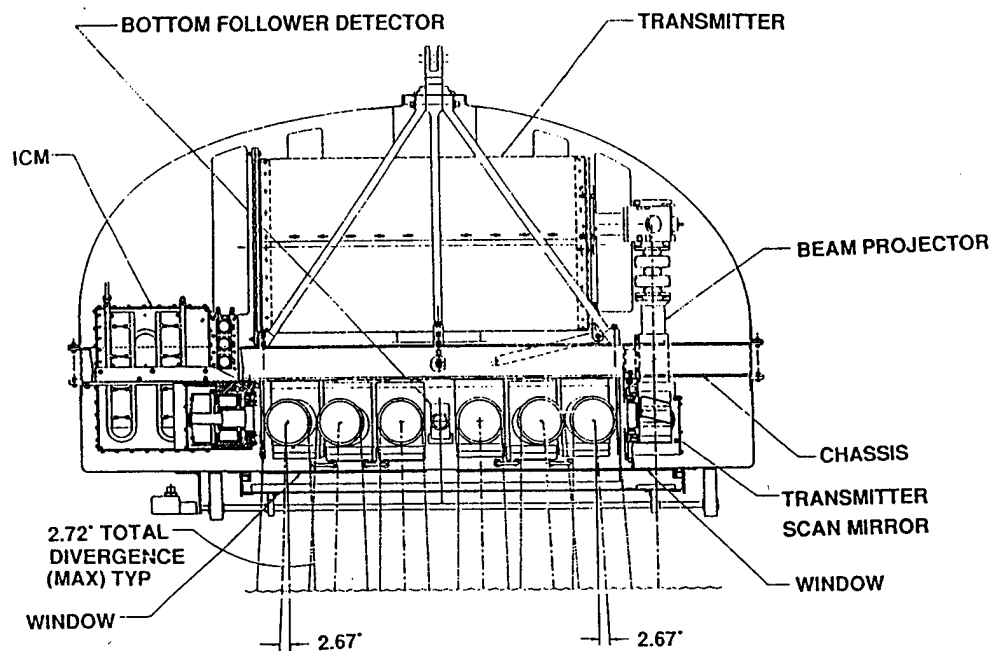
Figure 27: View of components within the pod of the ML(A) system, from the side looking in. (Kaman, 1993)
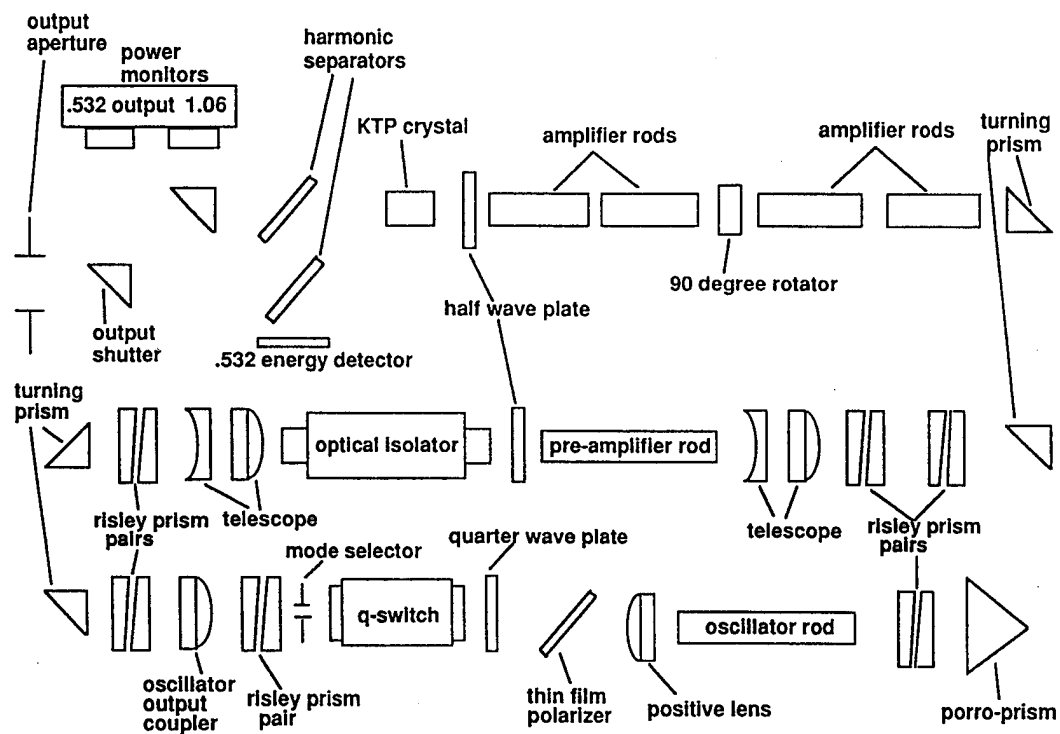
Figure 28: ML(A) Nd:YAG laser schematic. (Kaman, 1993)
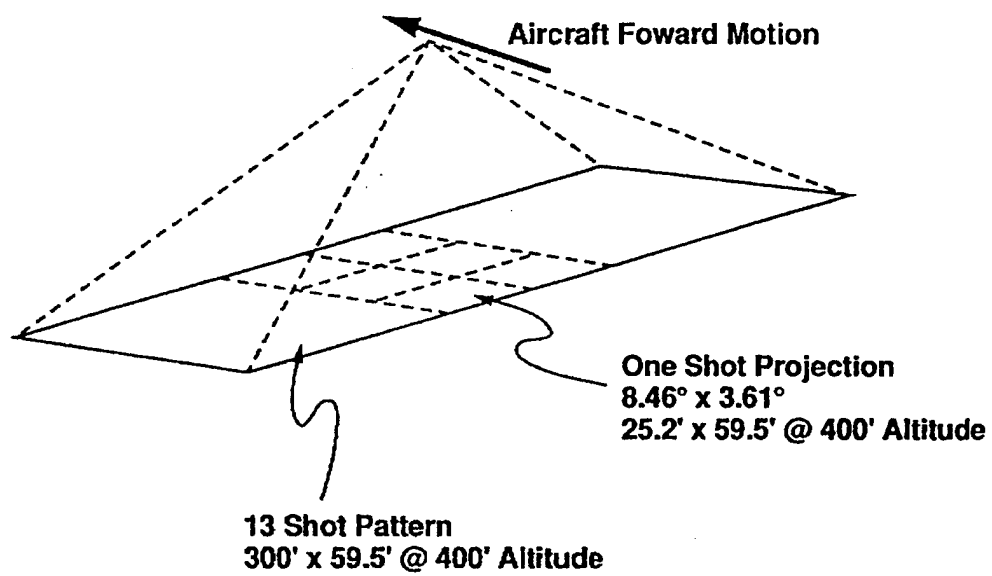
Figure 29: Projected illumination pattern of the ML(A) system. (Kaman, 1993)

2.72°
256 pixels
19 ft @ nadir
@ 400 ft. alt

Pixel on bottom
at max scan angle

0.97"

1.03"

1.78°
168 pixels
12.5 ft @ nadir @ 400 ft. alt
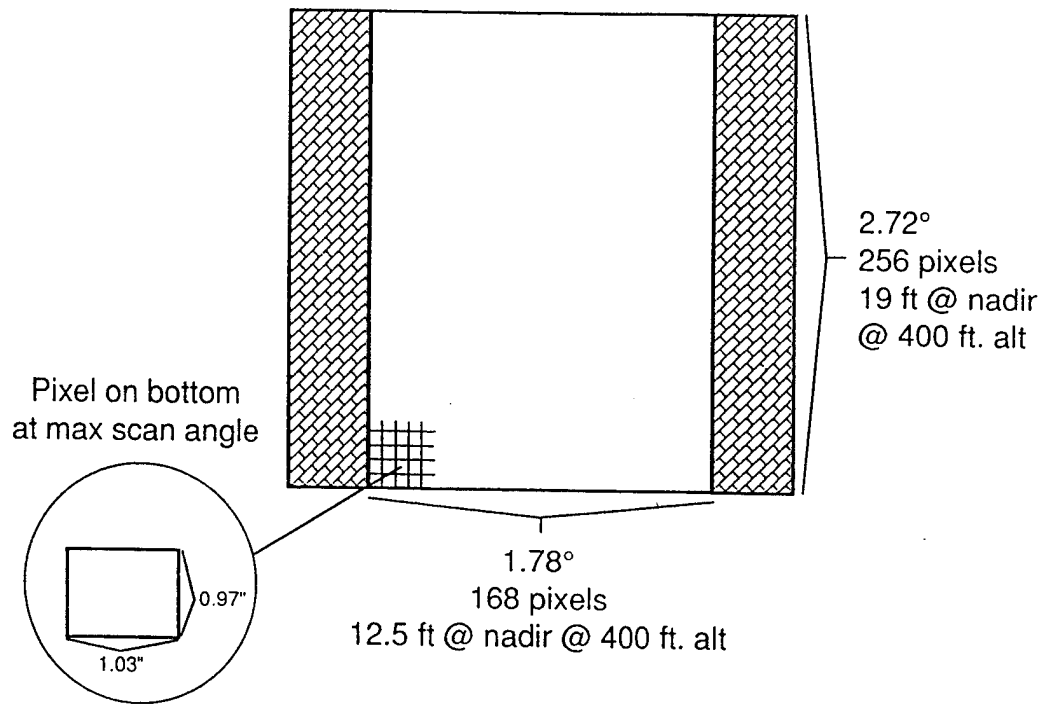
Figure 30: ML(A) receiver field of view. (Kaman, 1993)
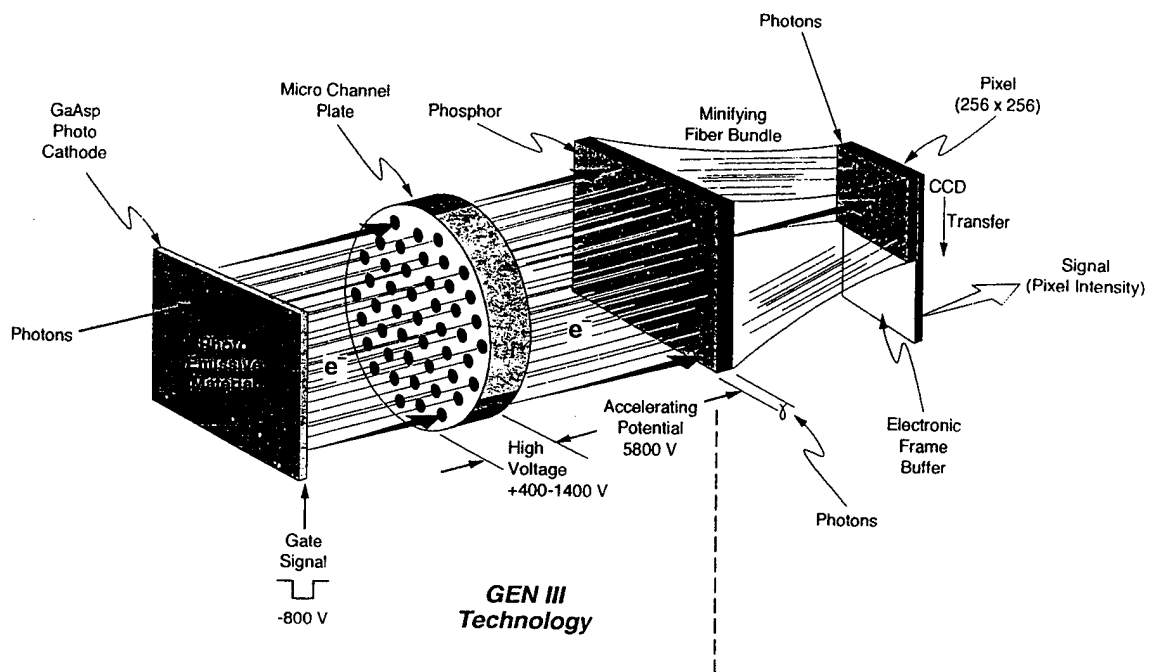
Figure 31: ML(A) system's Gen III intensified charge coupled device. (Kaman, 1993)
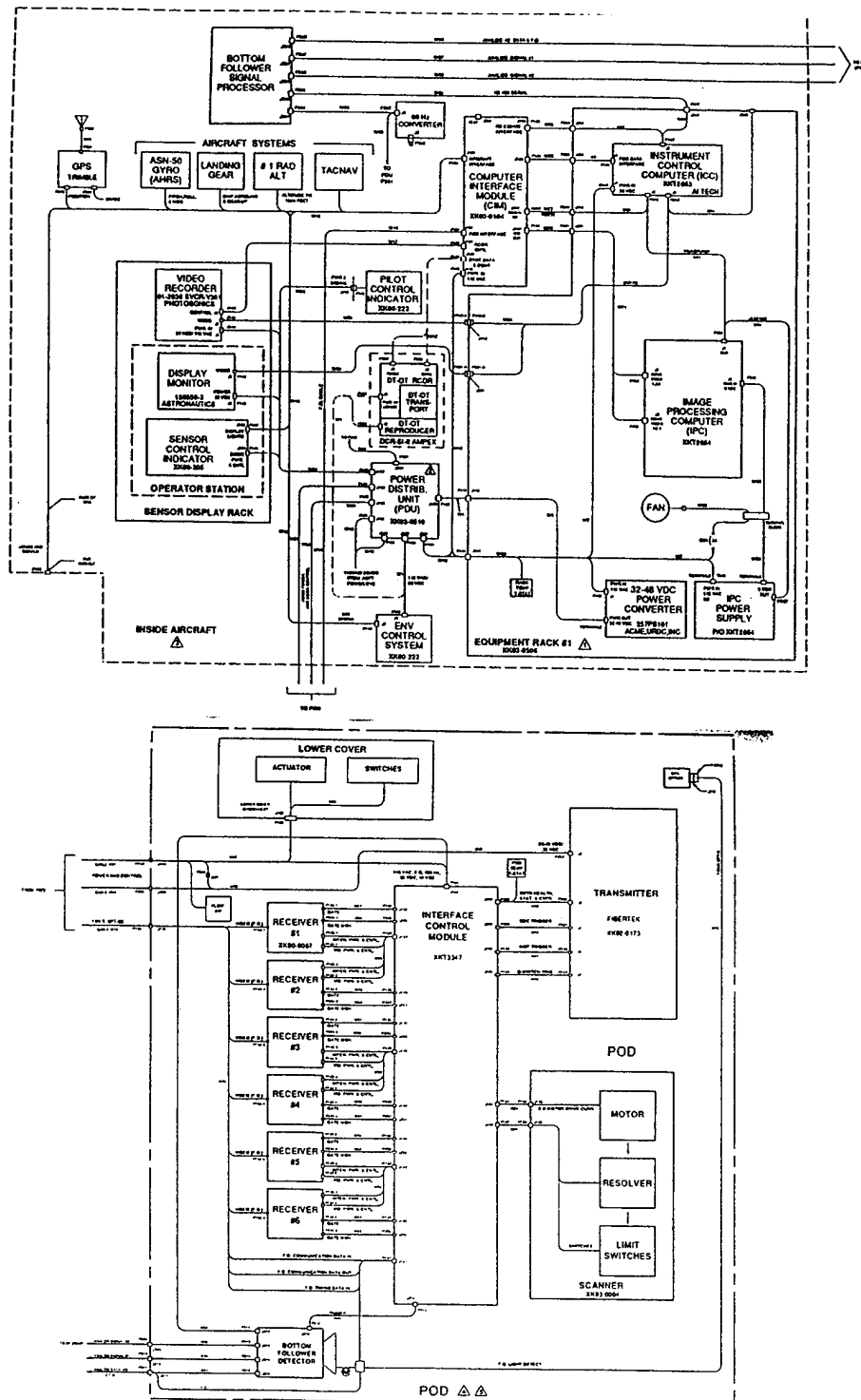
Figure 32: ML(A) sensor block diagram. (Kaman, 1993)
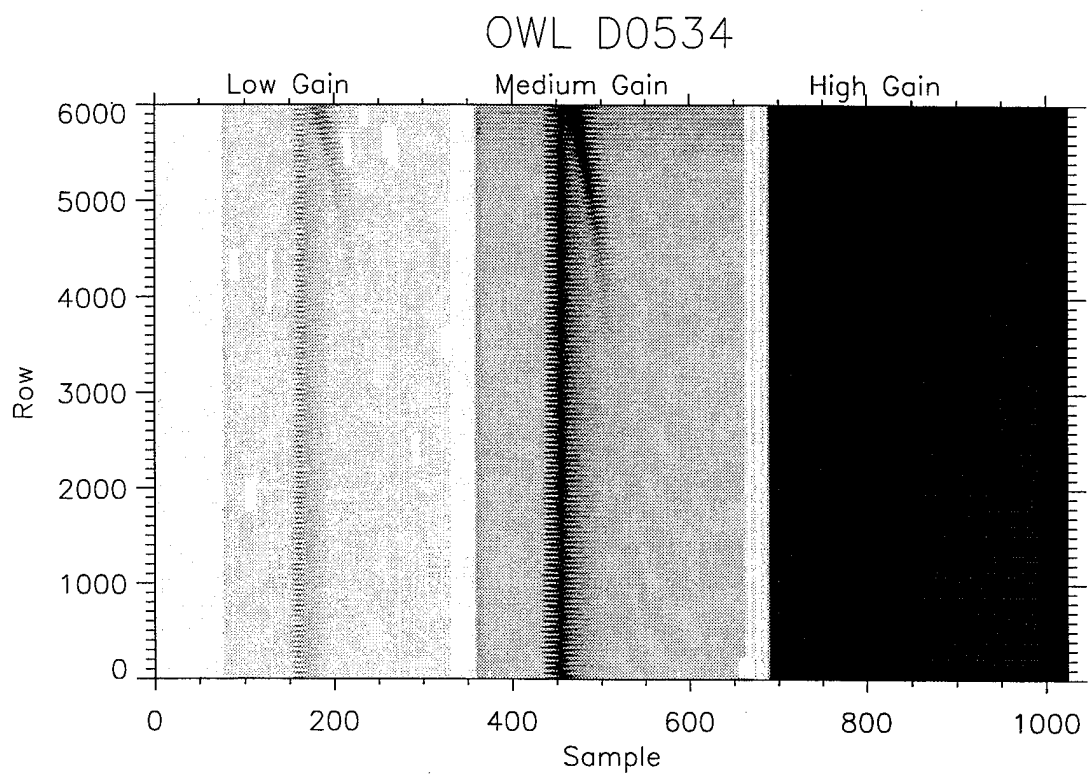
Figure 33: Overview plot of OWL data set D0534.

101

Figure 34: Panel plot of selected rows within OWL data set D0534.
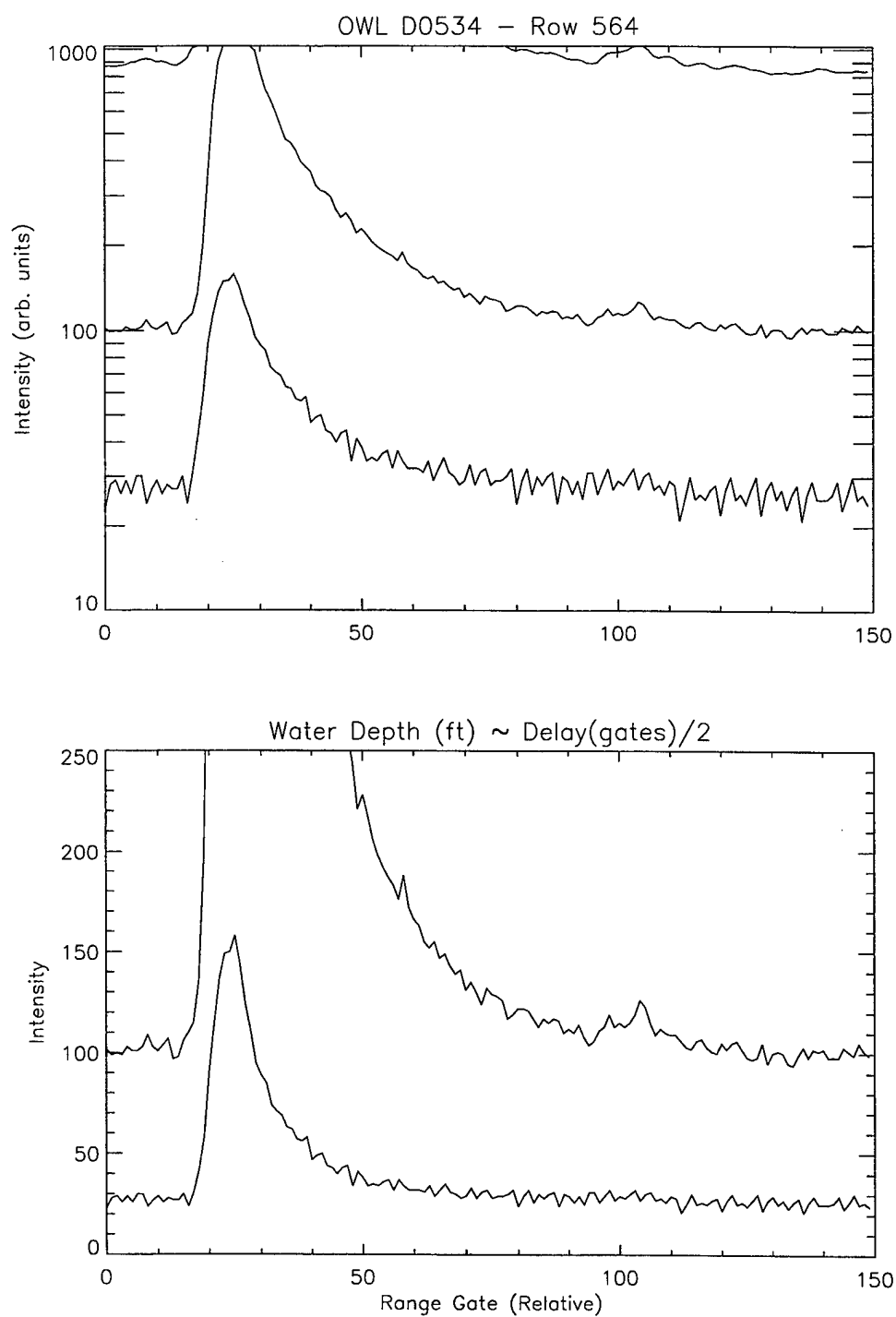
Figure 35: Line plot of row 564, OWL data set D0534.
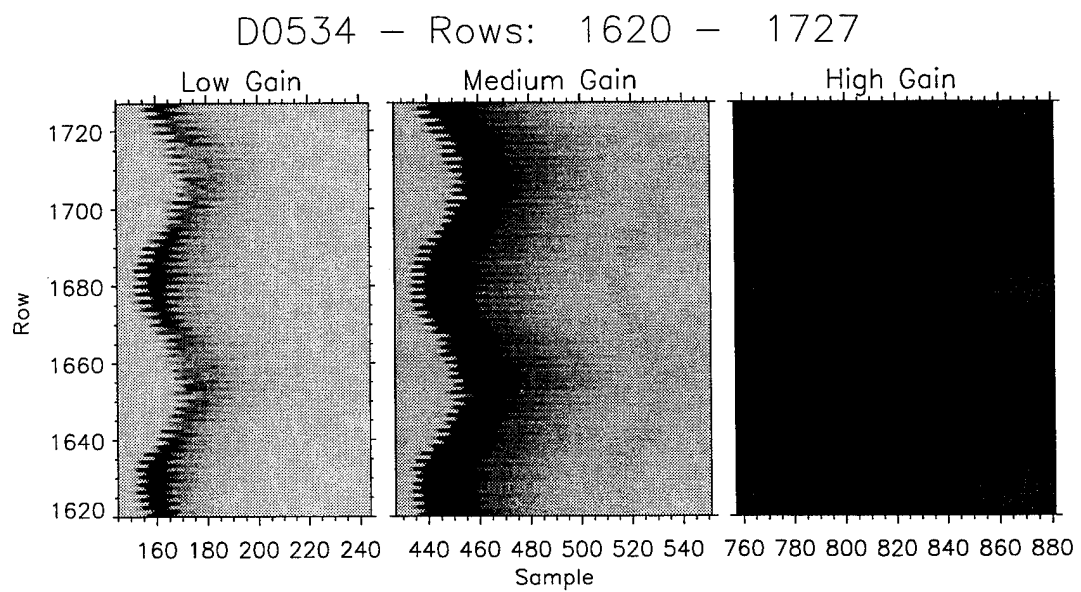
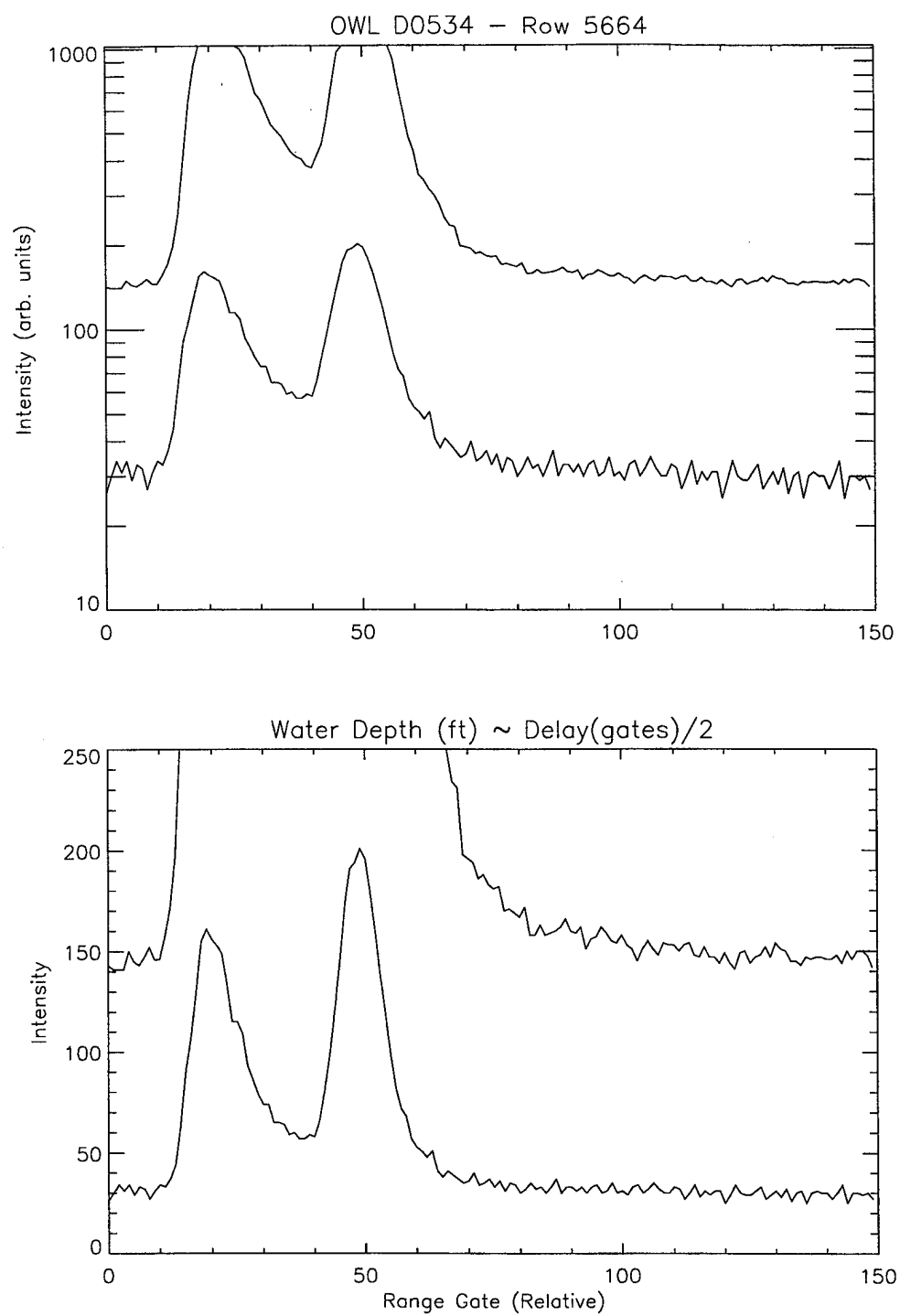Figure 36: Panel plot of selected rows within OWL data set D0534.
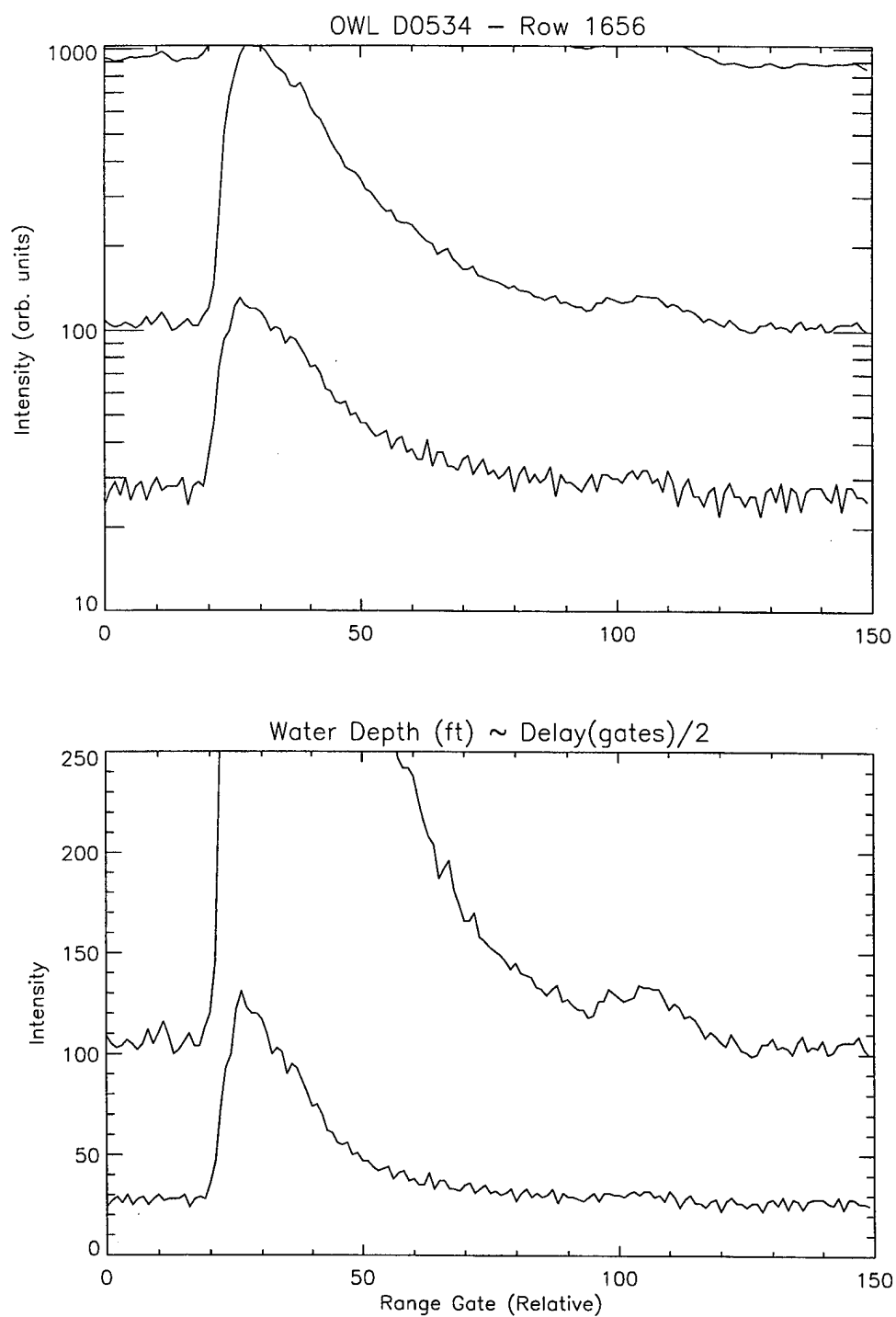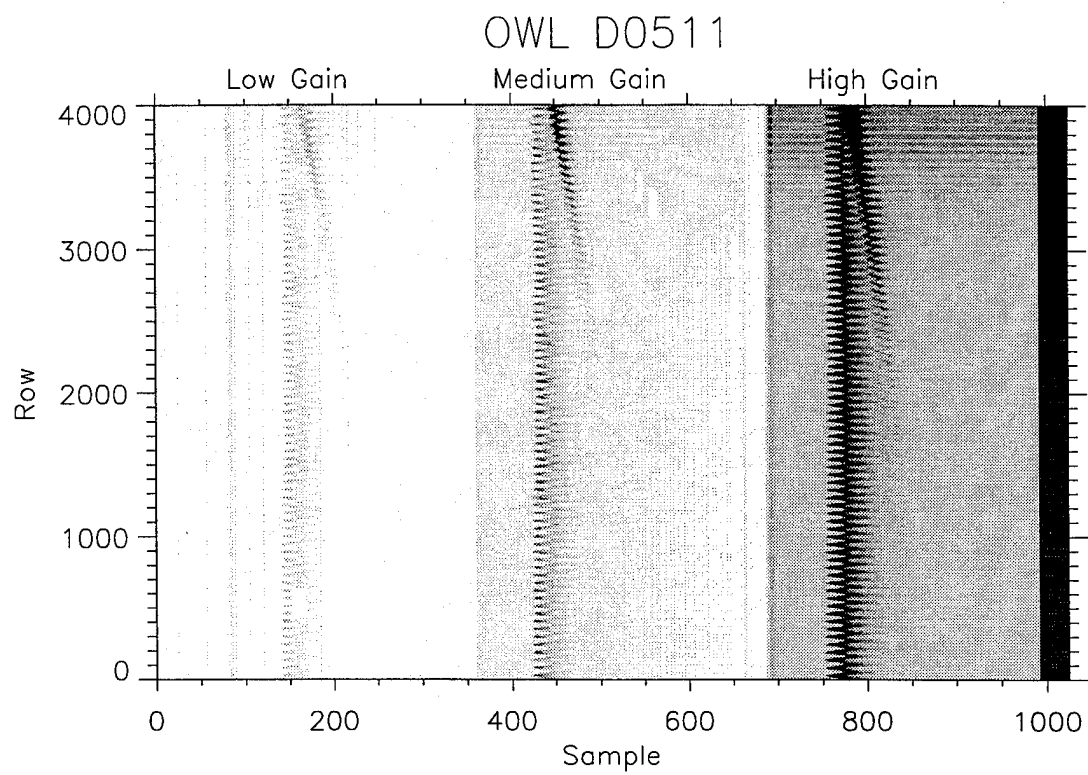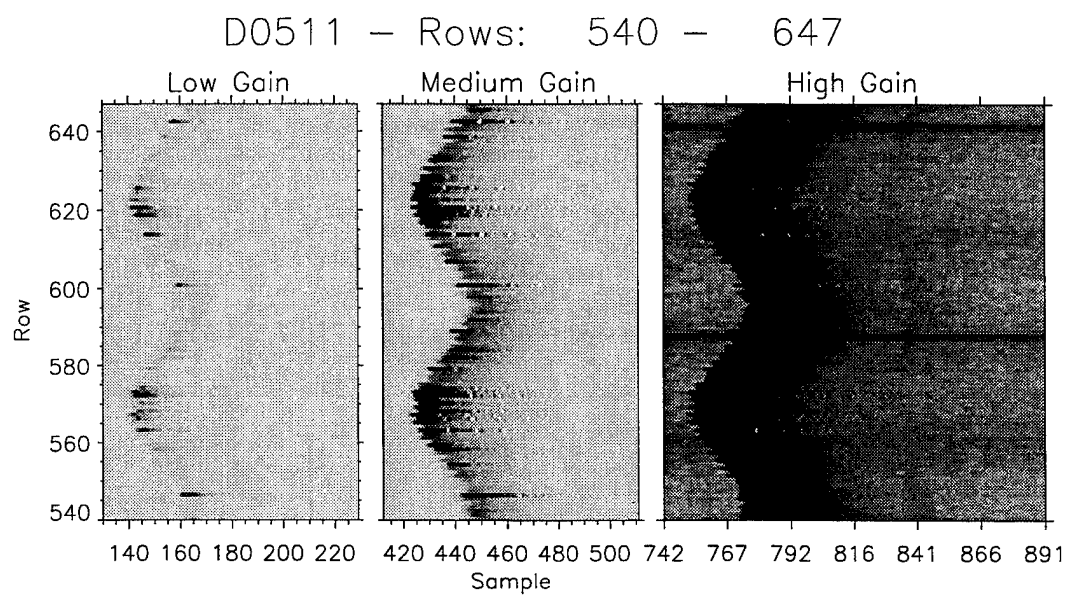
Figure 37: Line plot of row 1656, OWL data set D0534.
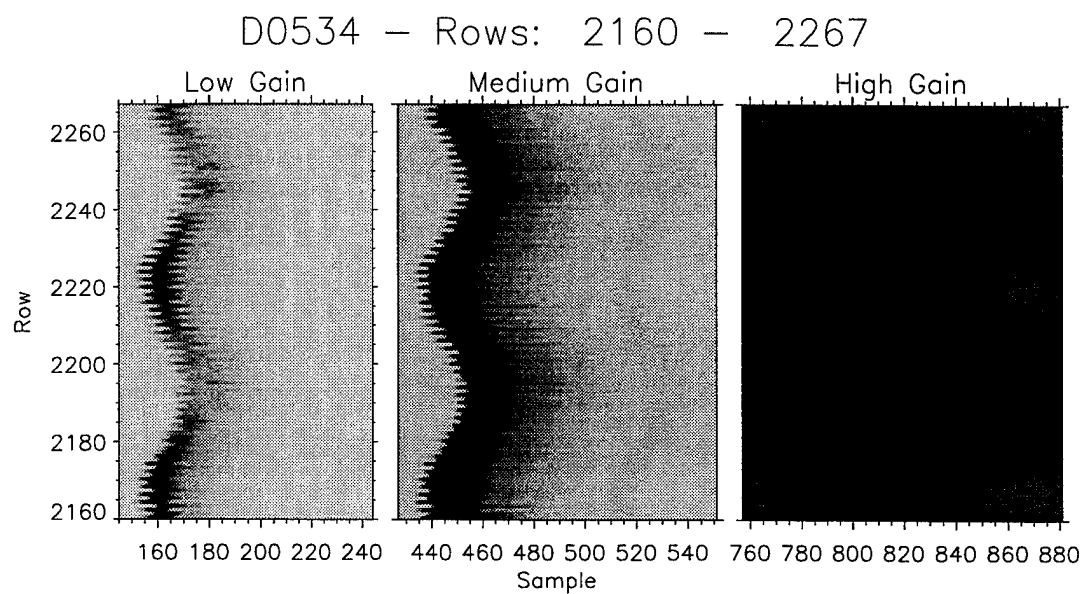
Figure 38: Panel plot of selected rows within OWL data set D0534.
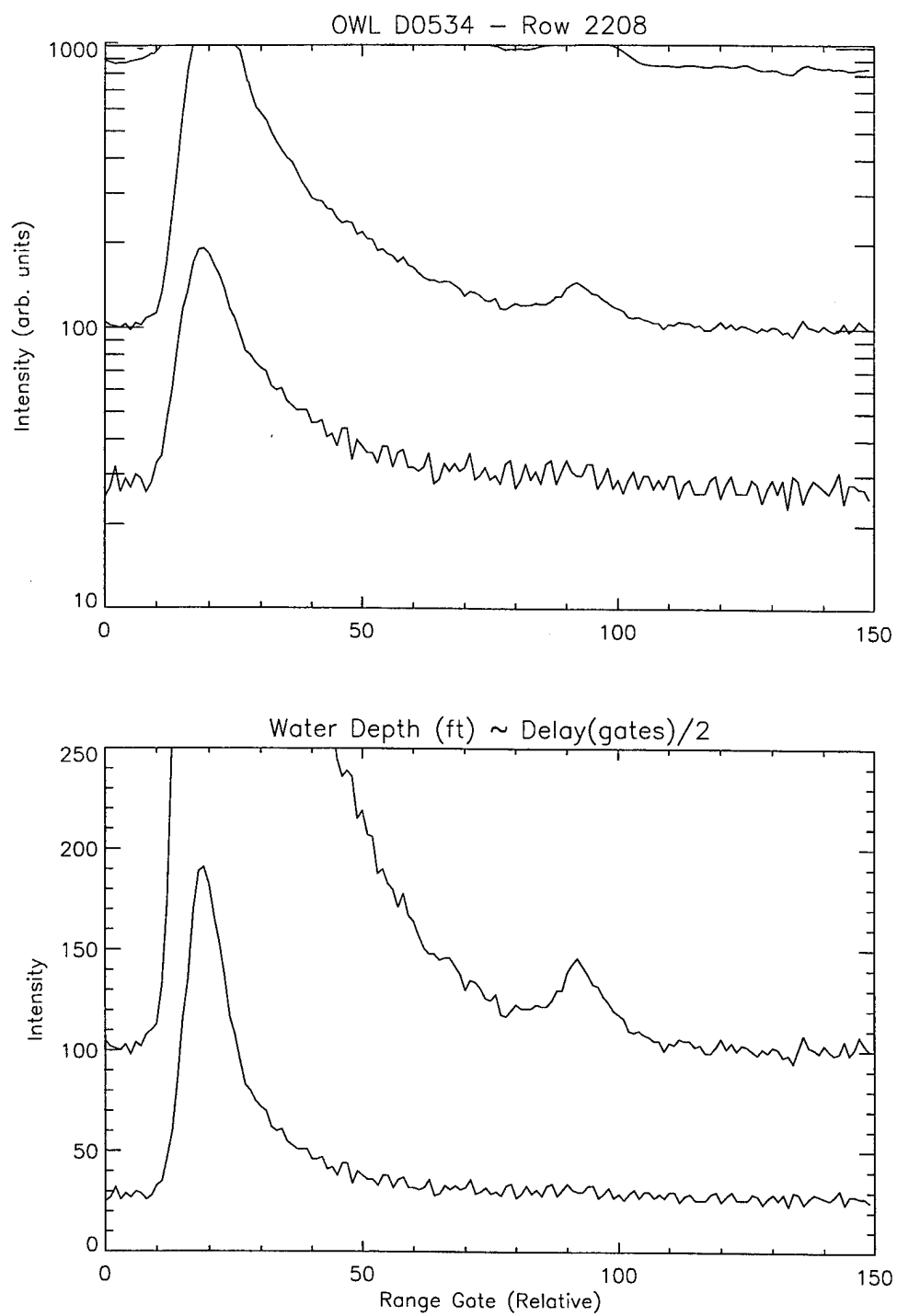
Figure 39: Line plot of row 2208, OWL data set D0534.
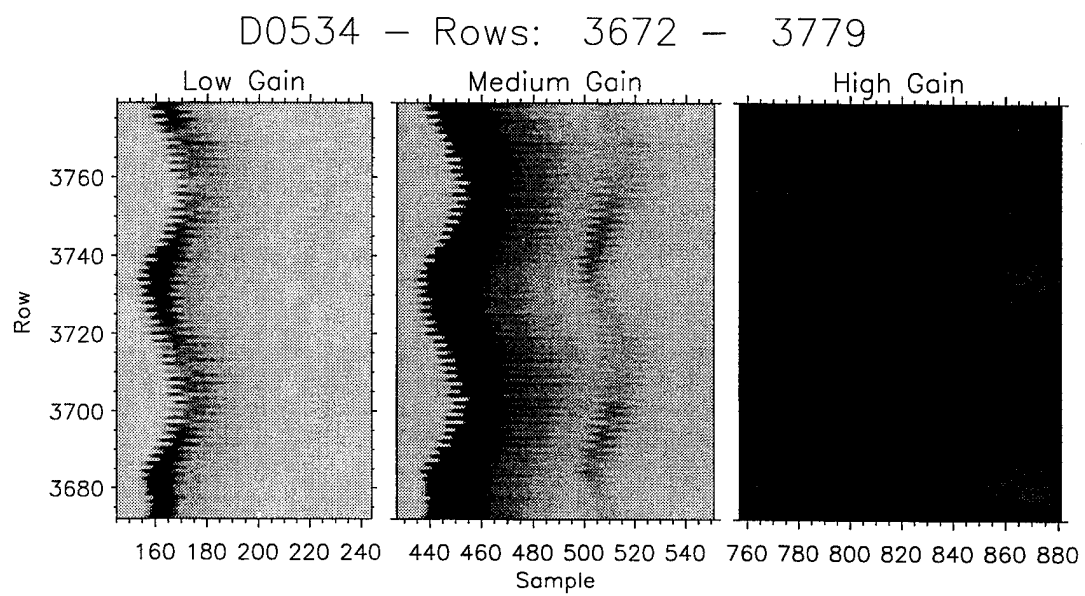
Figure 40: Panel plot of selected rows within OWL data set D0534.
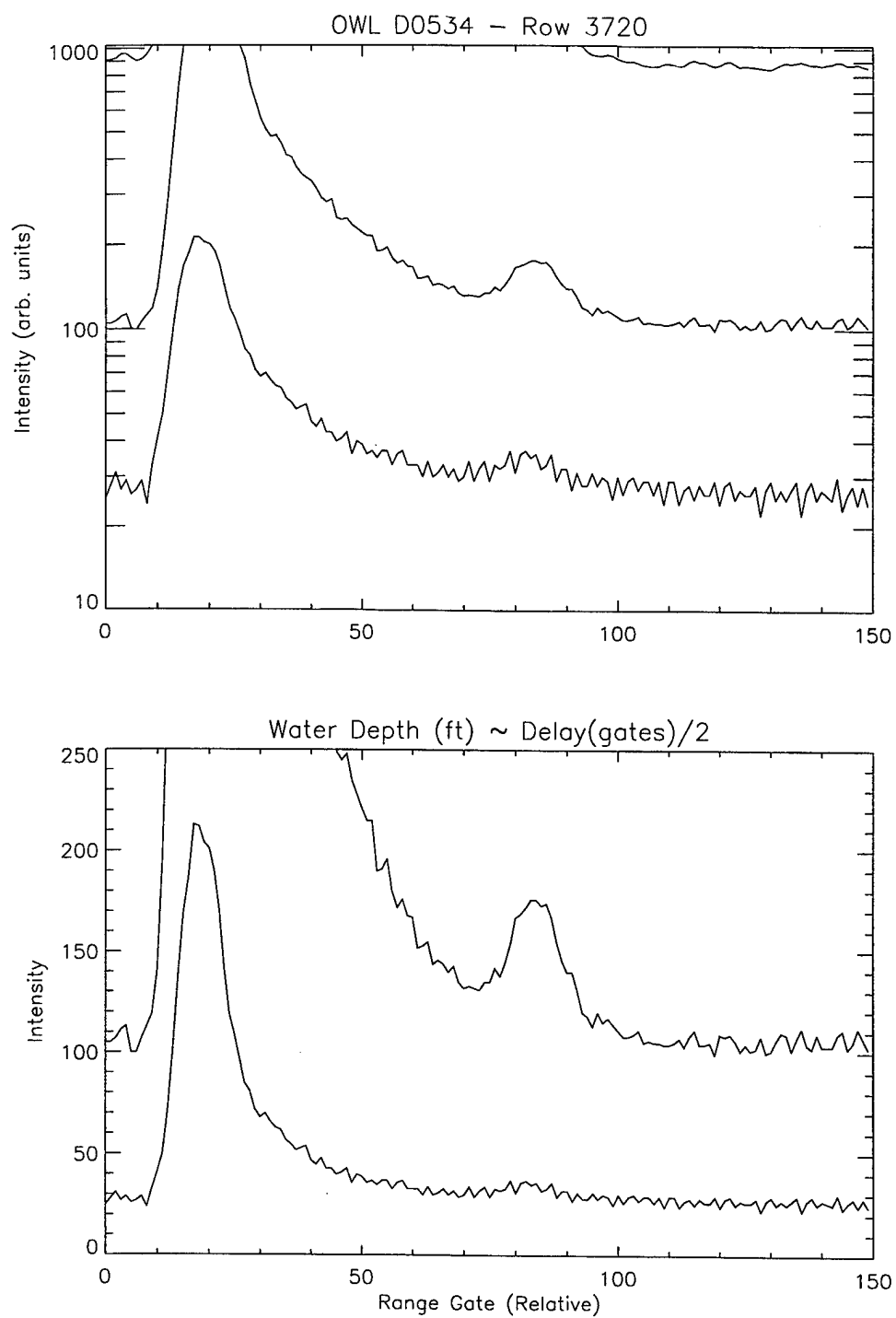
Figure 41: Line plot of row 3720, OWL data set D0534.
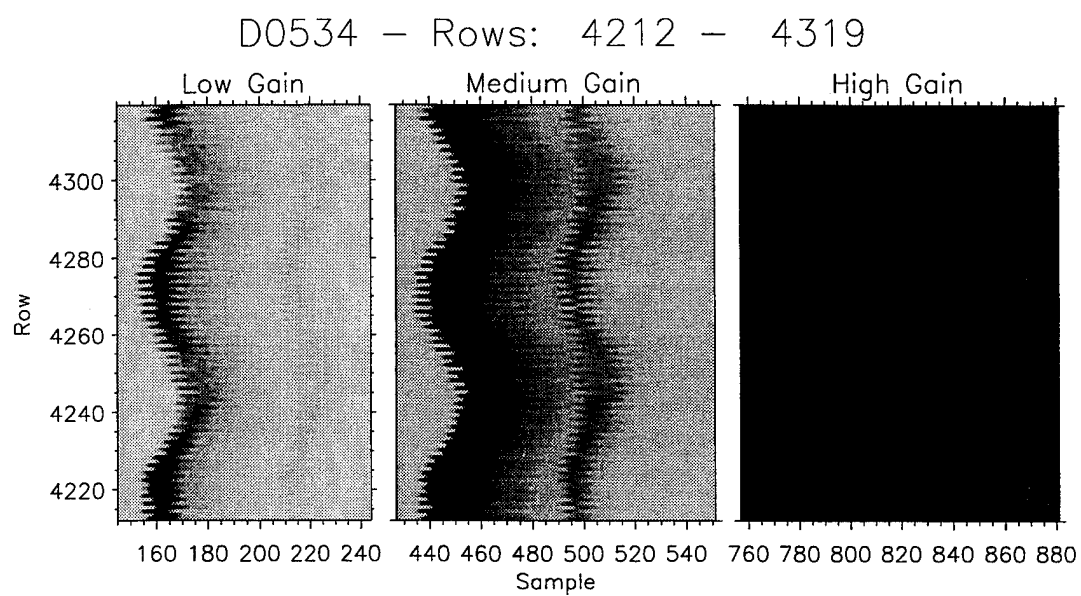
Figure 42: Panel plot of selected rows within OWL data set D0534.
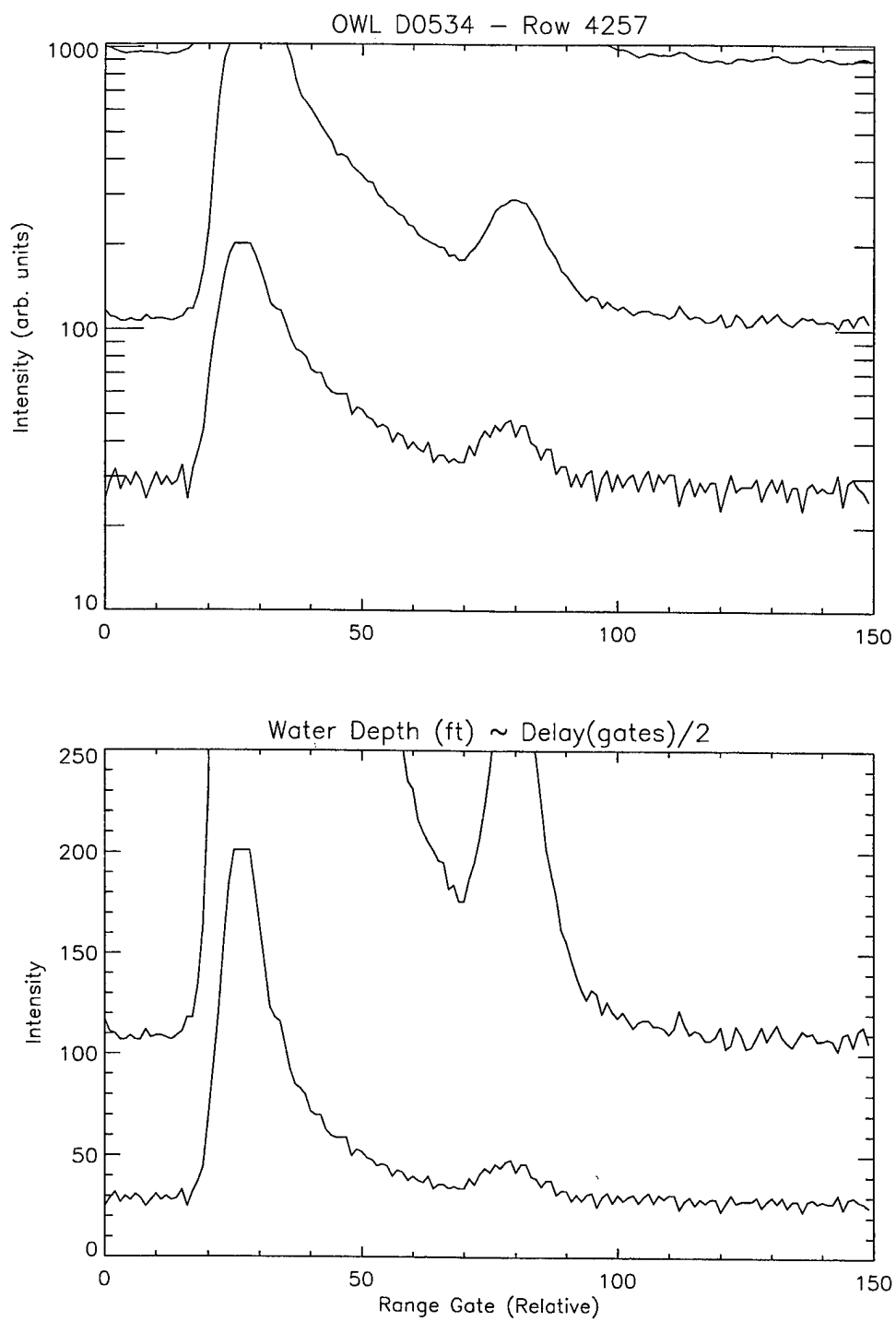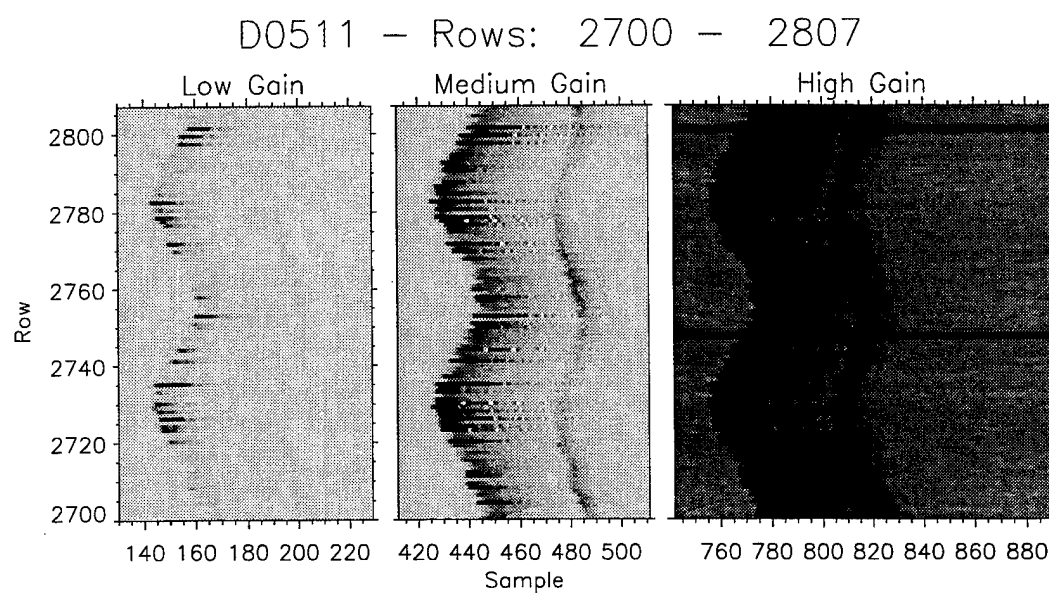
Figure 43: Line plot of row 4257, OWL data set D0534.
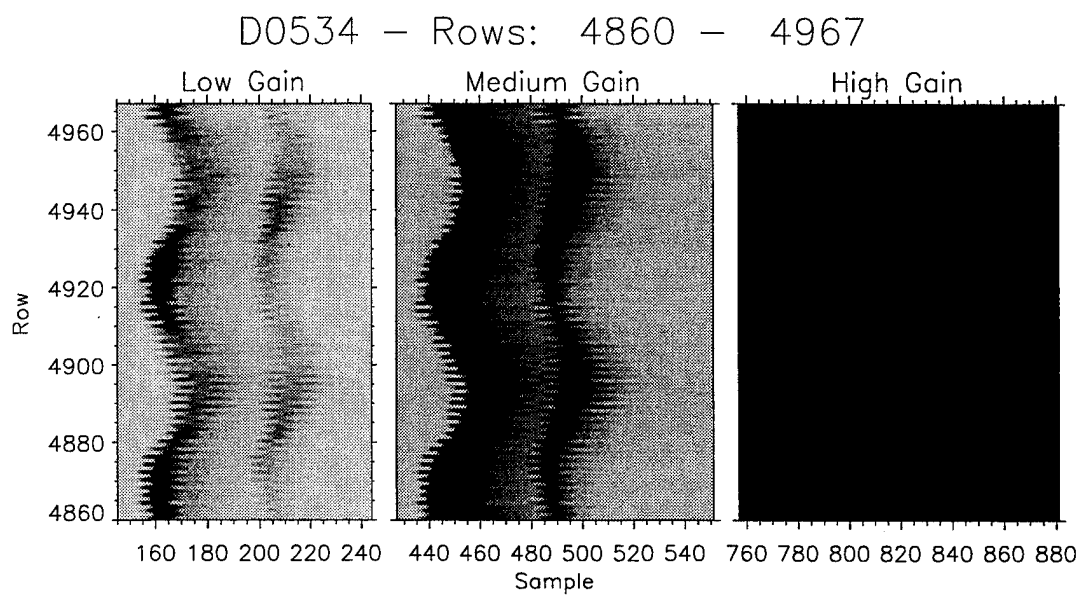
Figure 44: Panel plot of selected rows within OWL data set D0534.
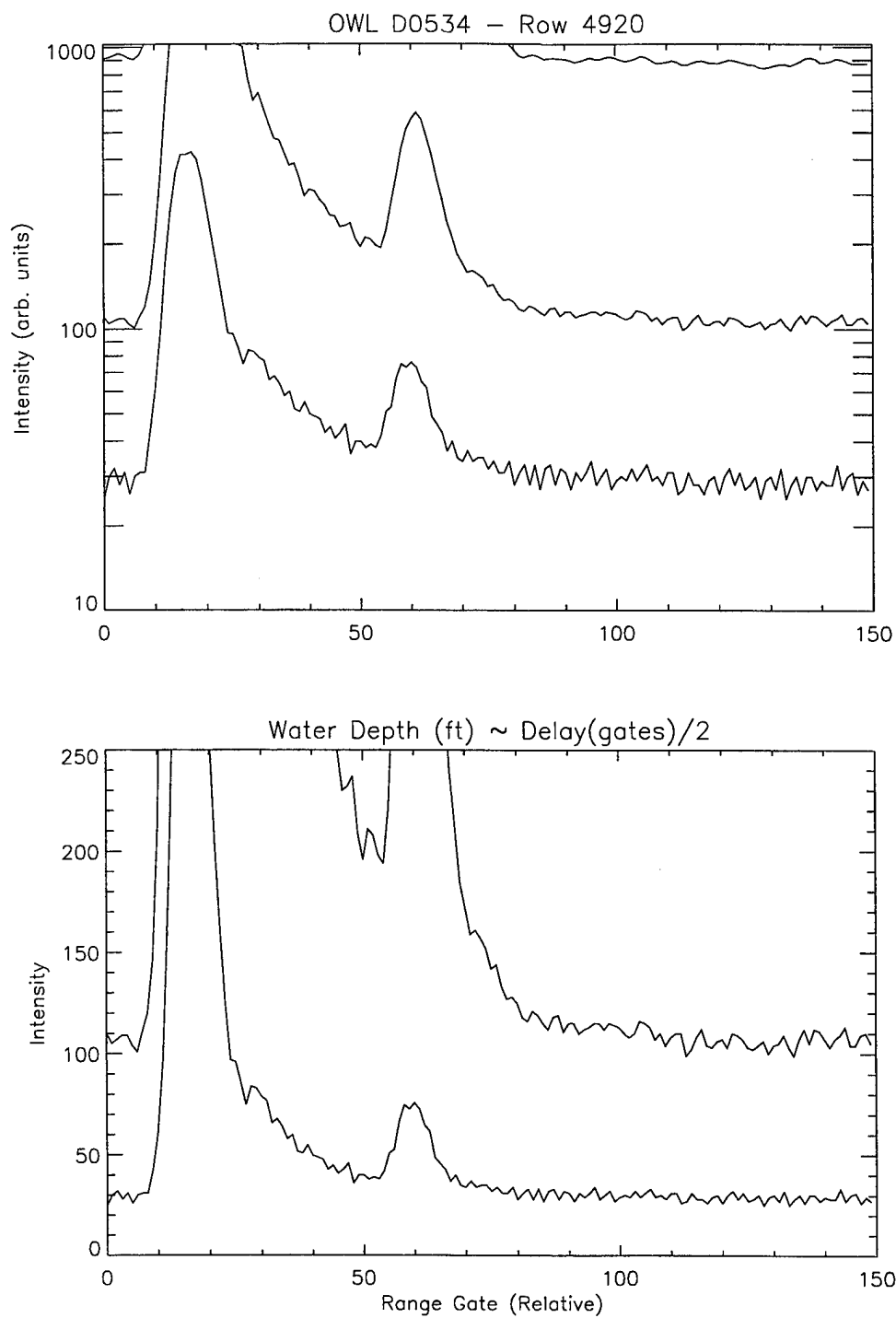
Figure 45: Line plot of row 4920, OWL data set D0534.
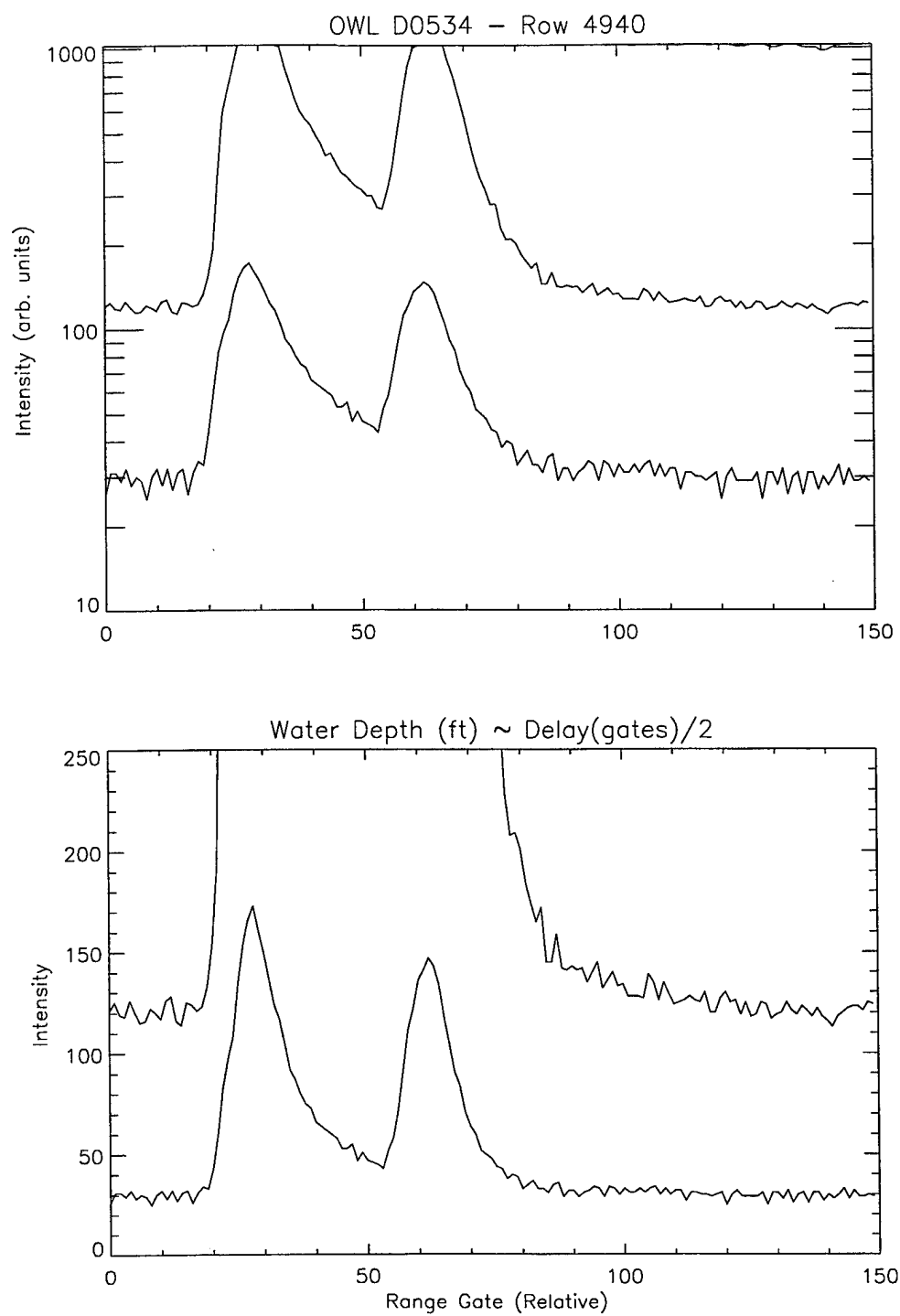
Figure 46: Line plot of row 4940, OWL data set D0534.
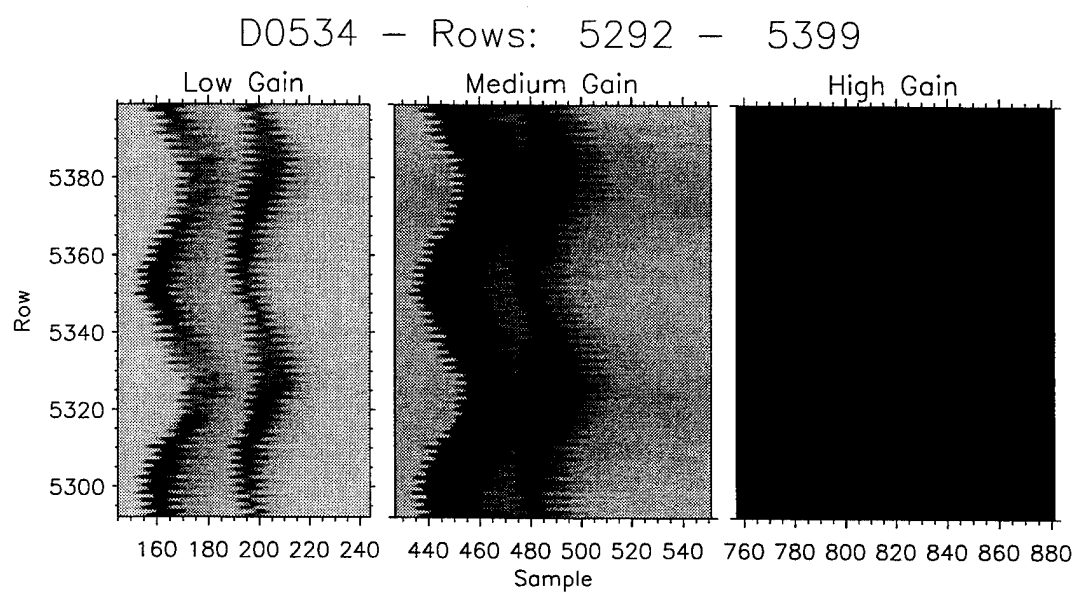
Figure 47: Panel plot of selected rows within OWL data set D0534.
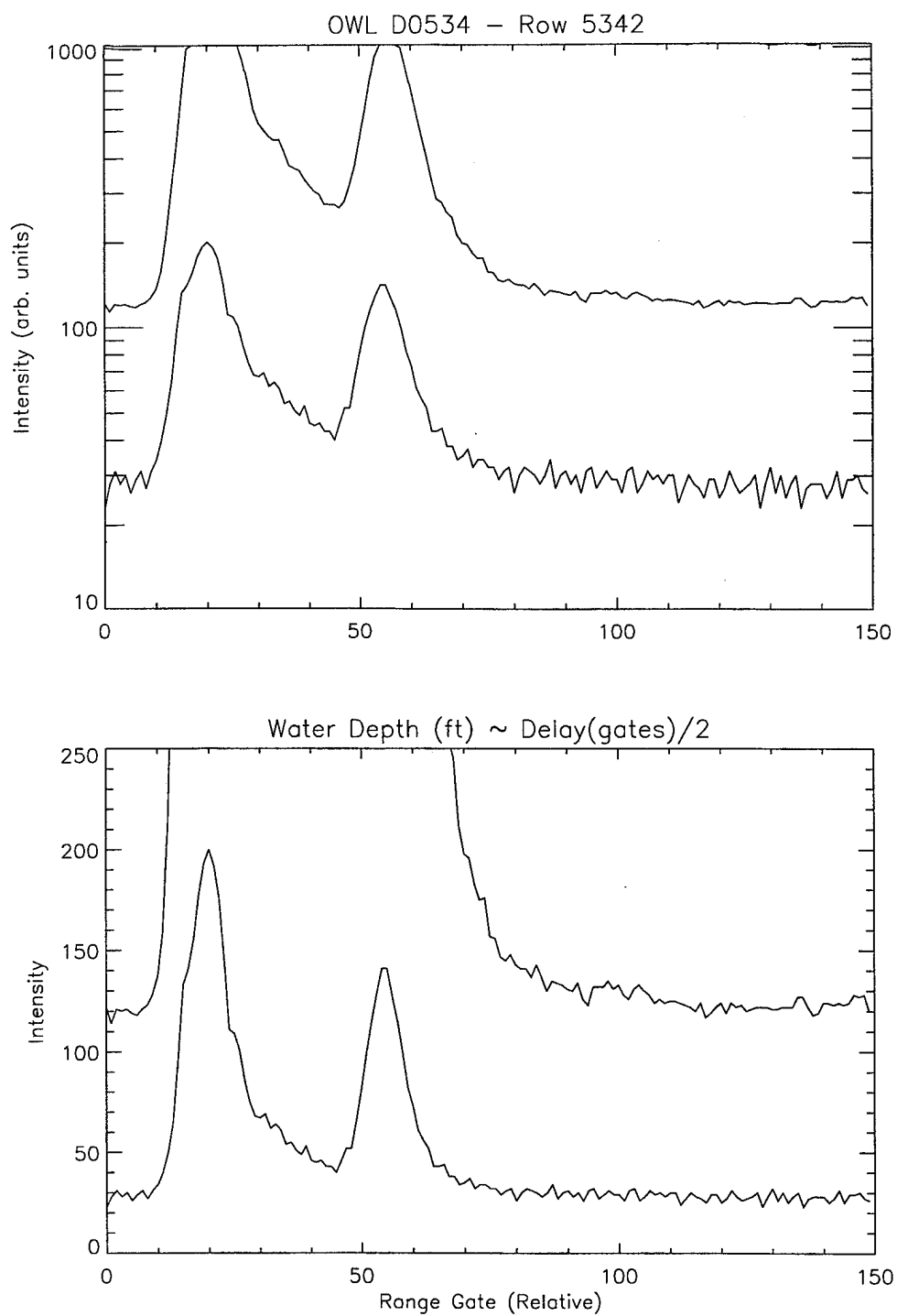
Figure 48: Line plot of row 5342, OWL data set D0534.

D0534 − Rows: 5616 − 5723
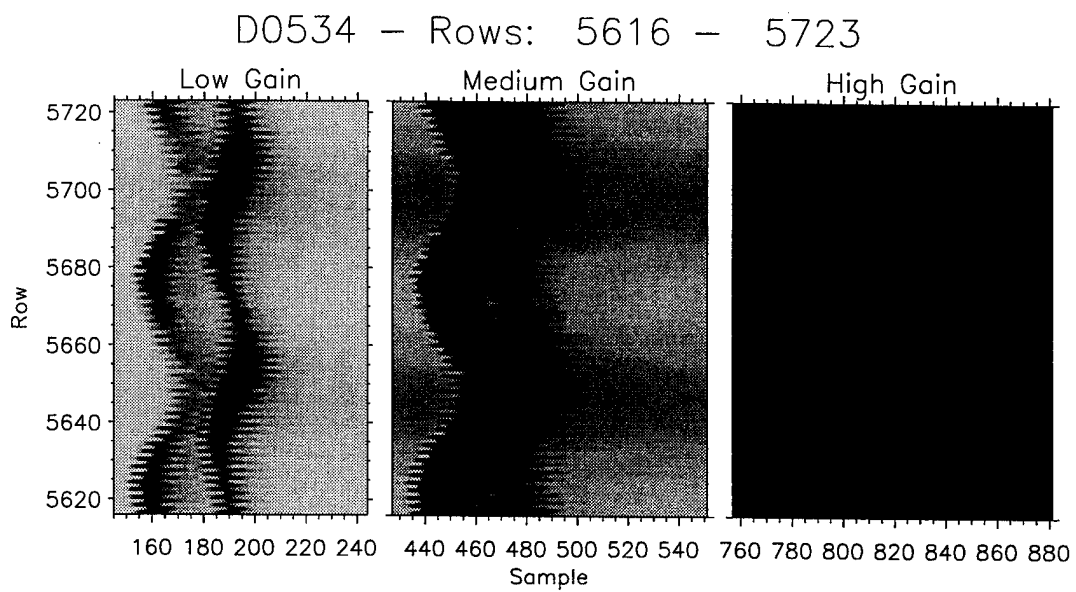
Figure 49: Panel plot of selected rows within OWL data set D0534.

Figure 50: Line plot of row 5664, OWL data set D0534.

Figure 51: Overview plot of OWL data set D0511.

Naval Postgraduate School Run on: 31-Aug-1995

119

Figure 52: Panel plot of selected rows within OWL data set D0511.
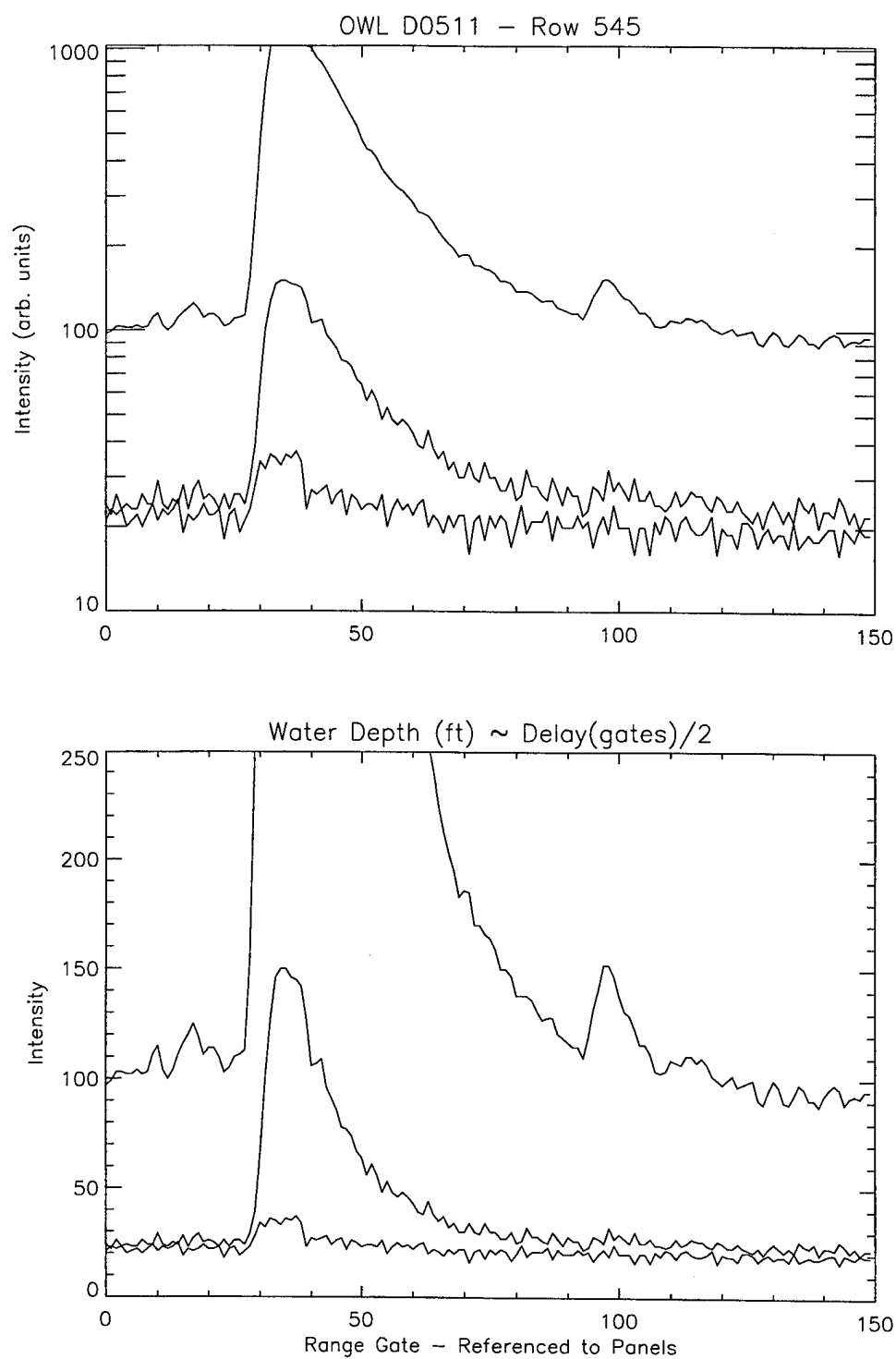
Figure 53: Line plot of row 545, OWL data set D0511.

Figure 54: Panel plot of selected rows within OWL data set D0511.
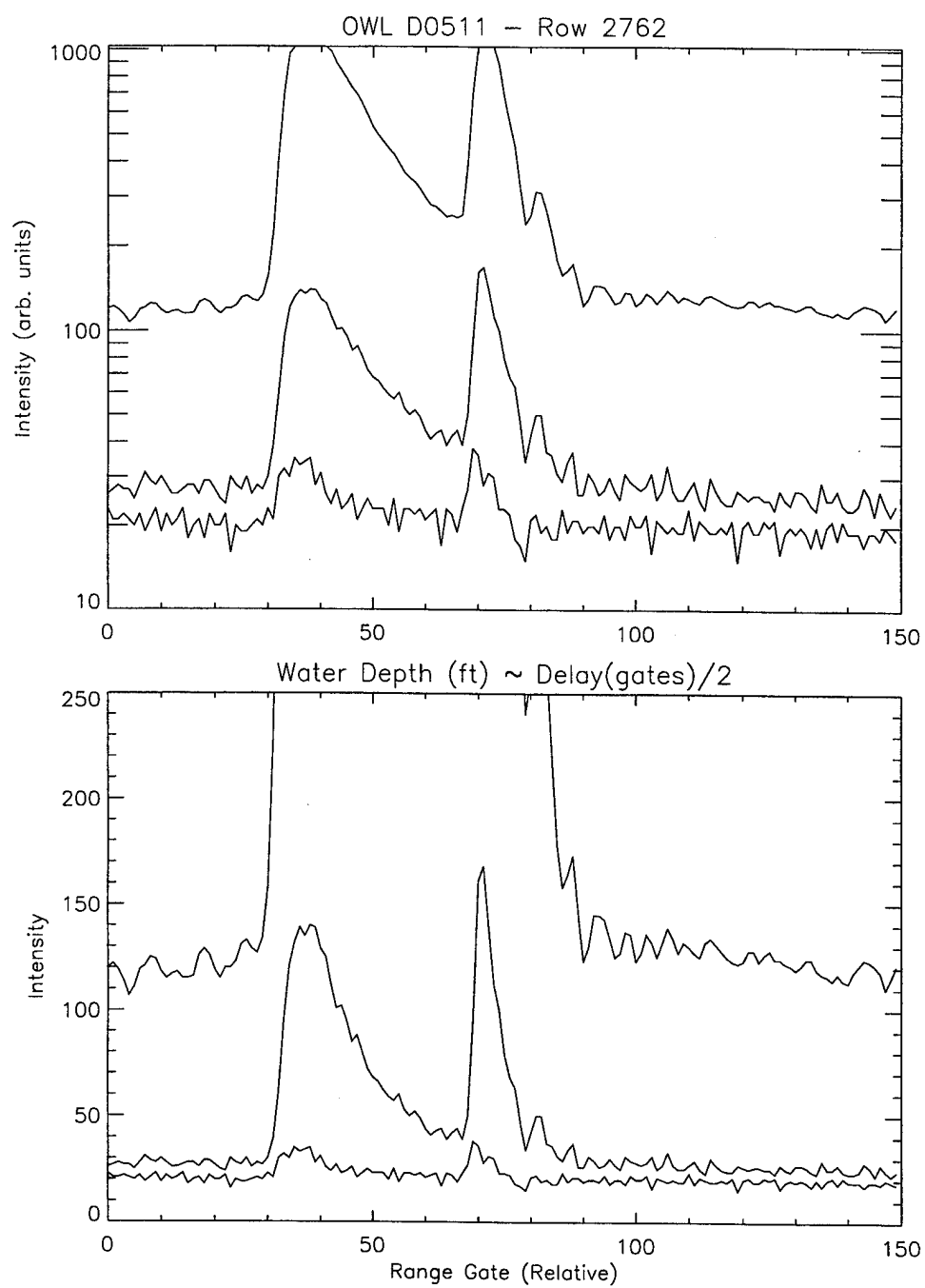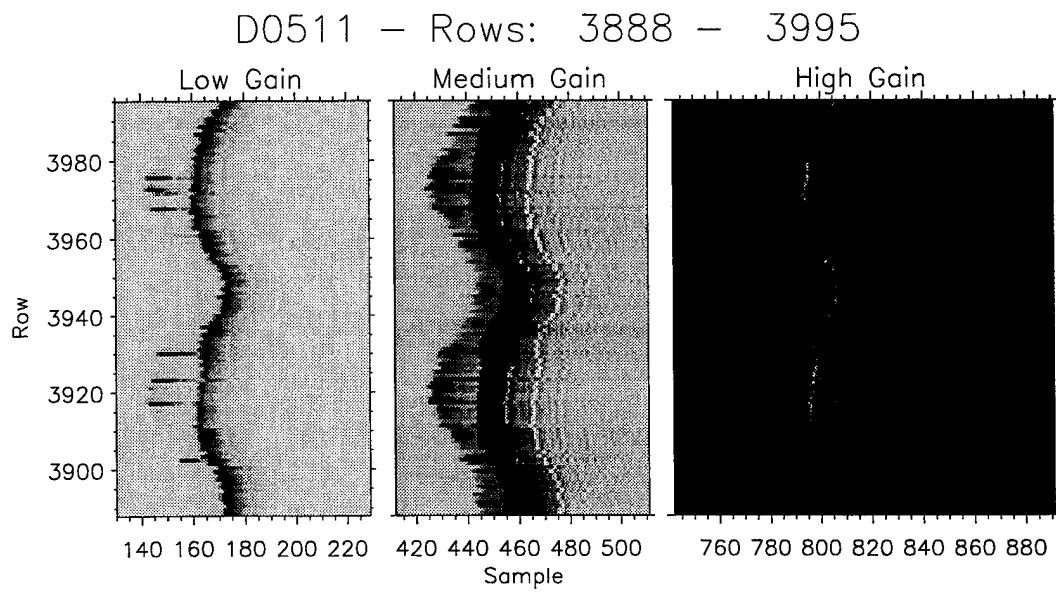
Figure 55: Line plot of row 2762, OWL data set D0511.
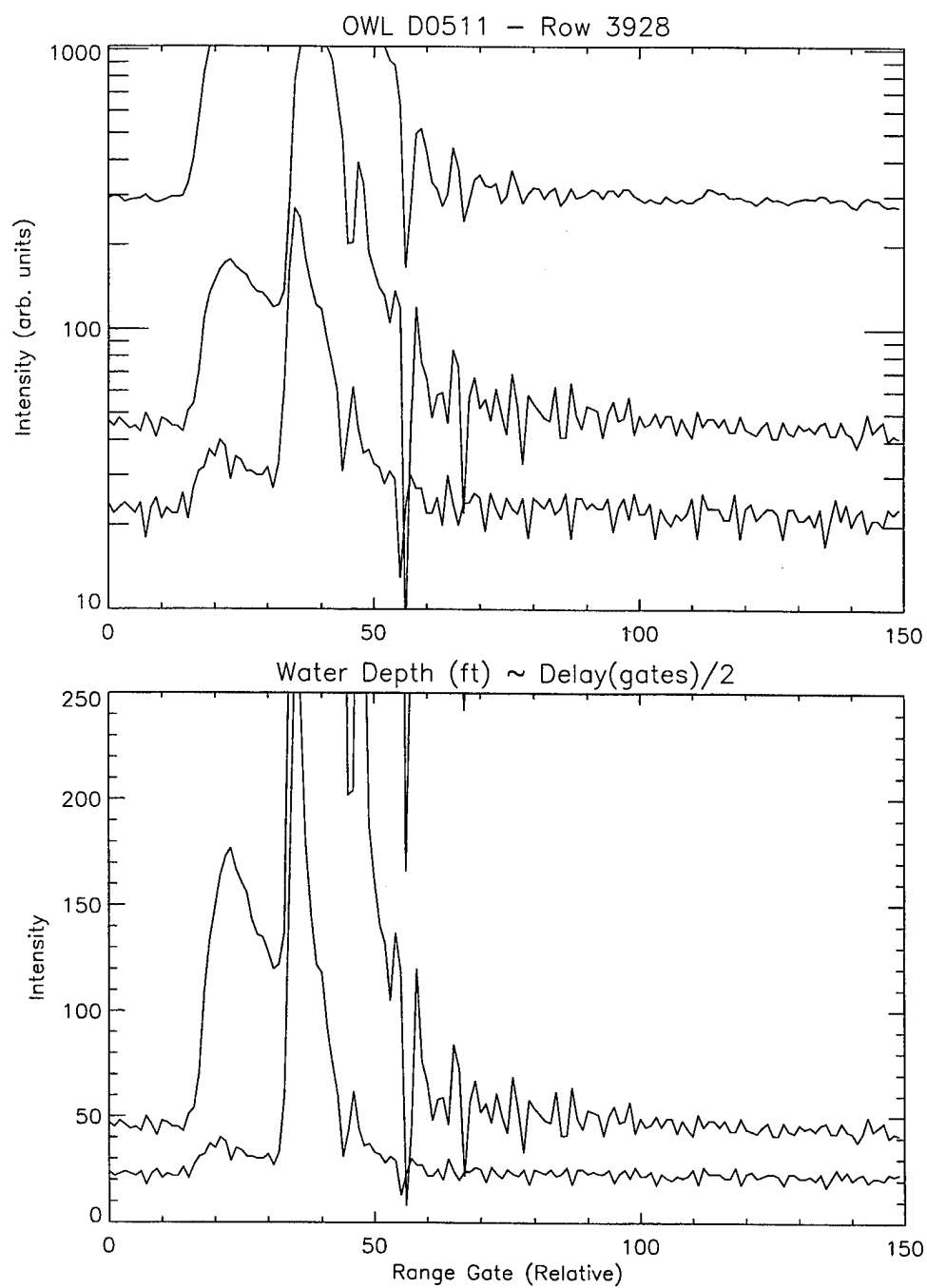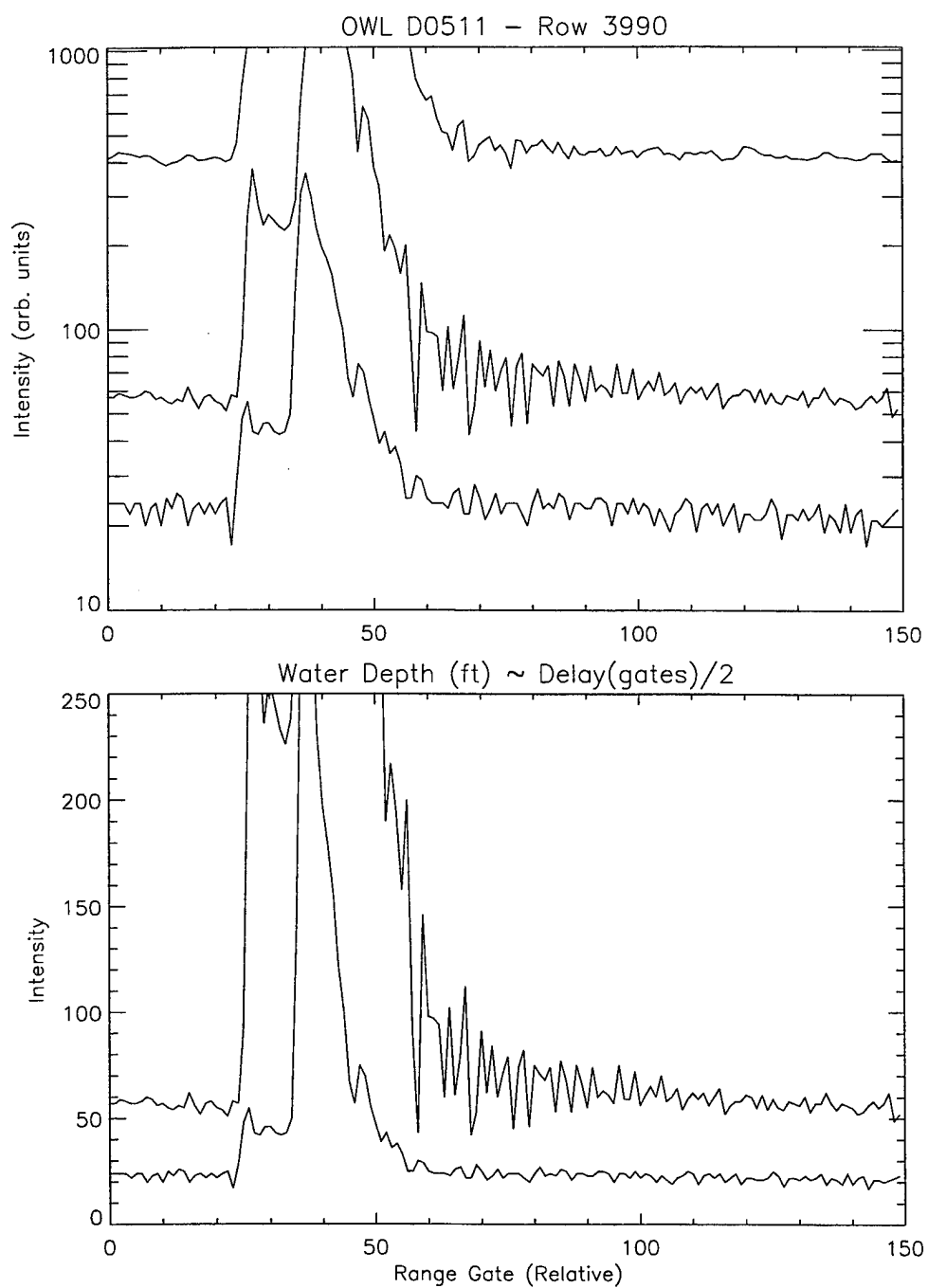
Figure 56: Panel plot of selected rows within OWL data set D0511.

OWL D0511 — Row 3928

Figure 57: Line plot of row 3928, OWL data set D0511.

Figure 58: Line plot of row 3990, OWL data set D0511.
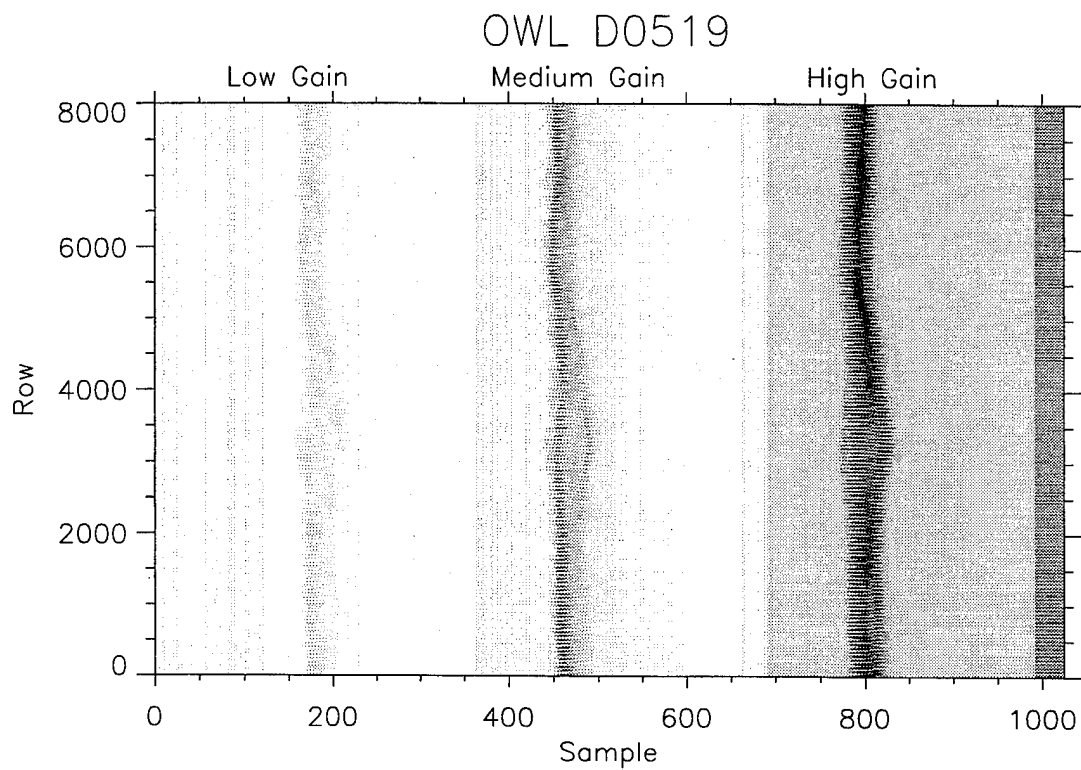
Figure 59: Overview plot of OWL data set D0519.

Figure 60: Panel plot of selected rows within OWL data set D0519.
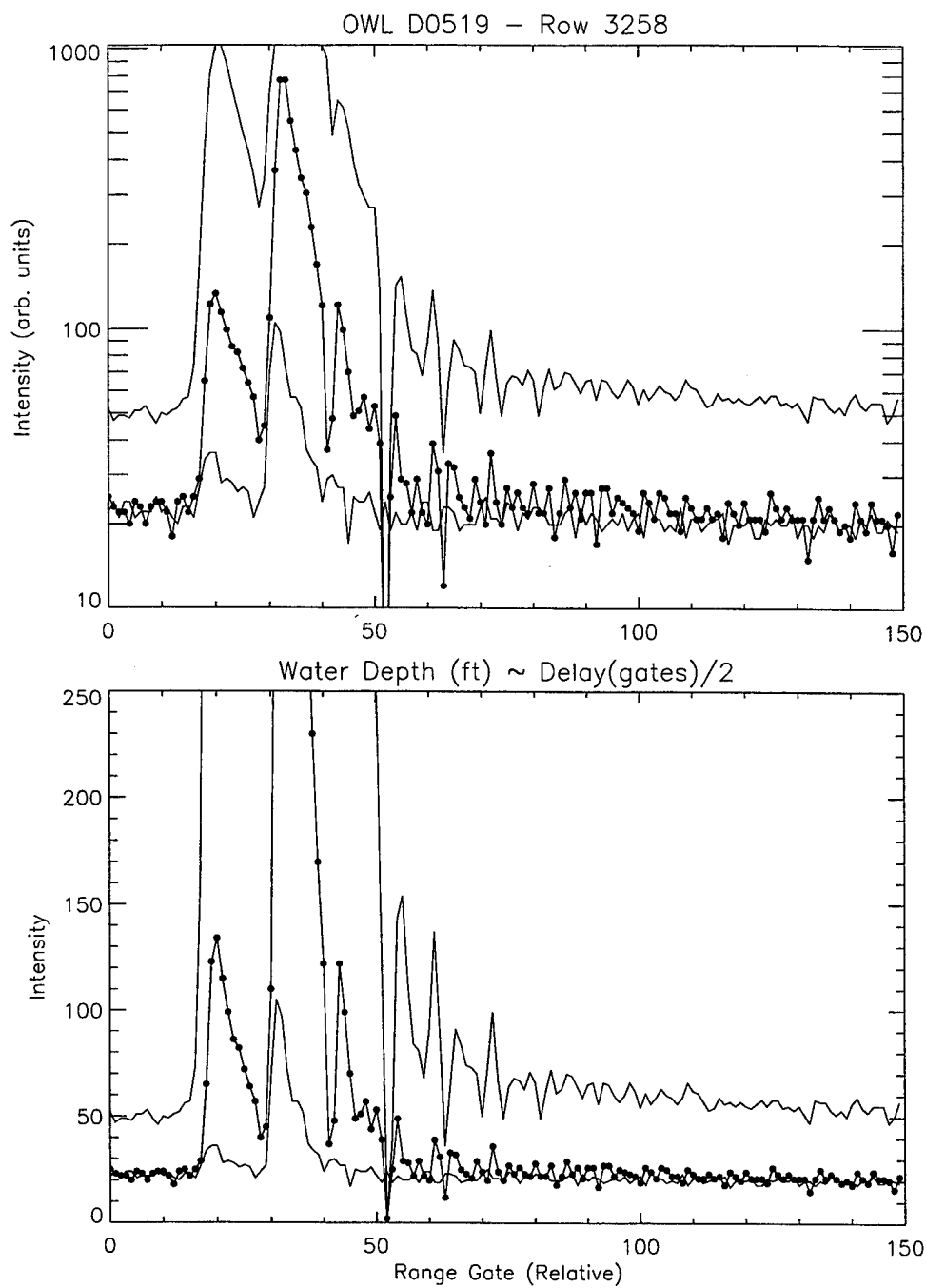
Figure 61: Line plot of row 3258, OWL data set D0519.

D0519 – Rows: 4212 – 4319
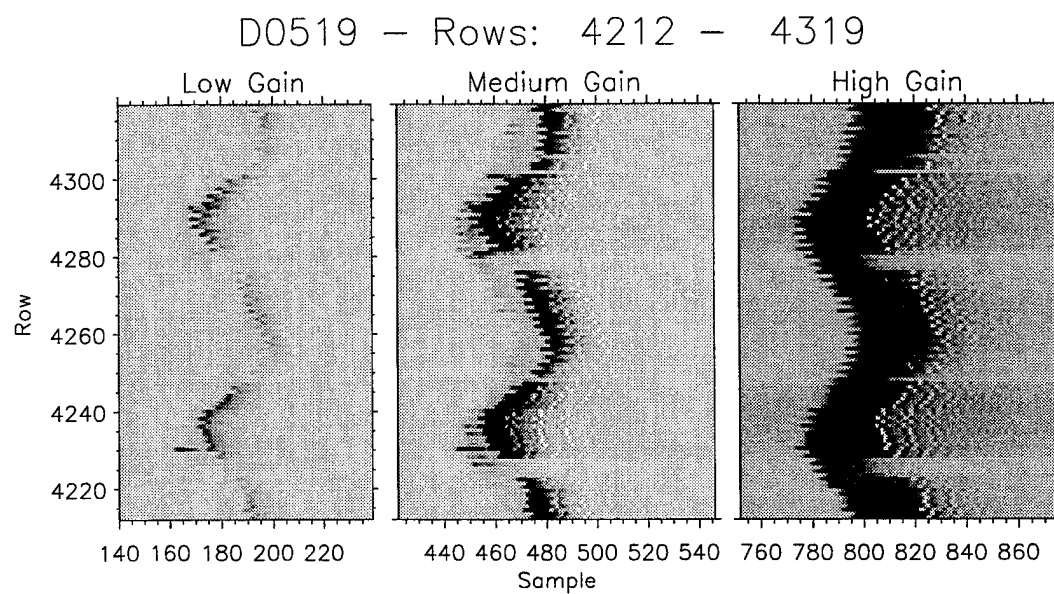
Figure 62: Panel plot of selected rows within OWL data set D0519.
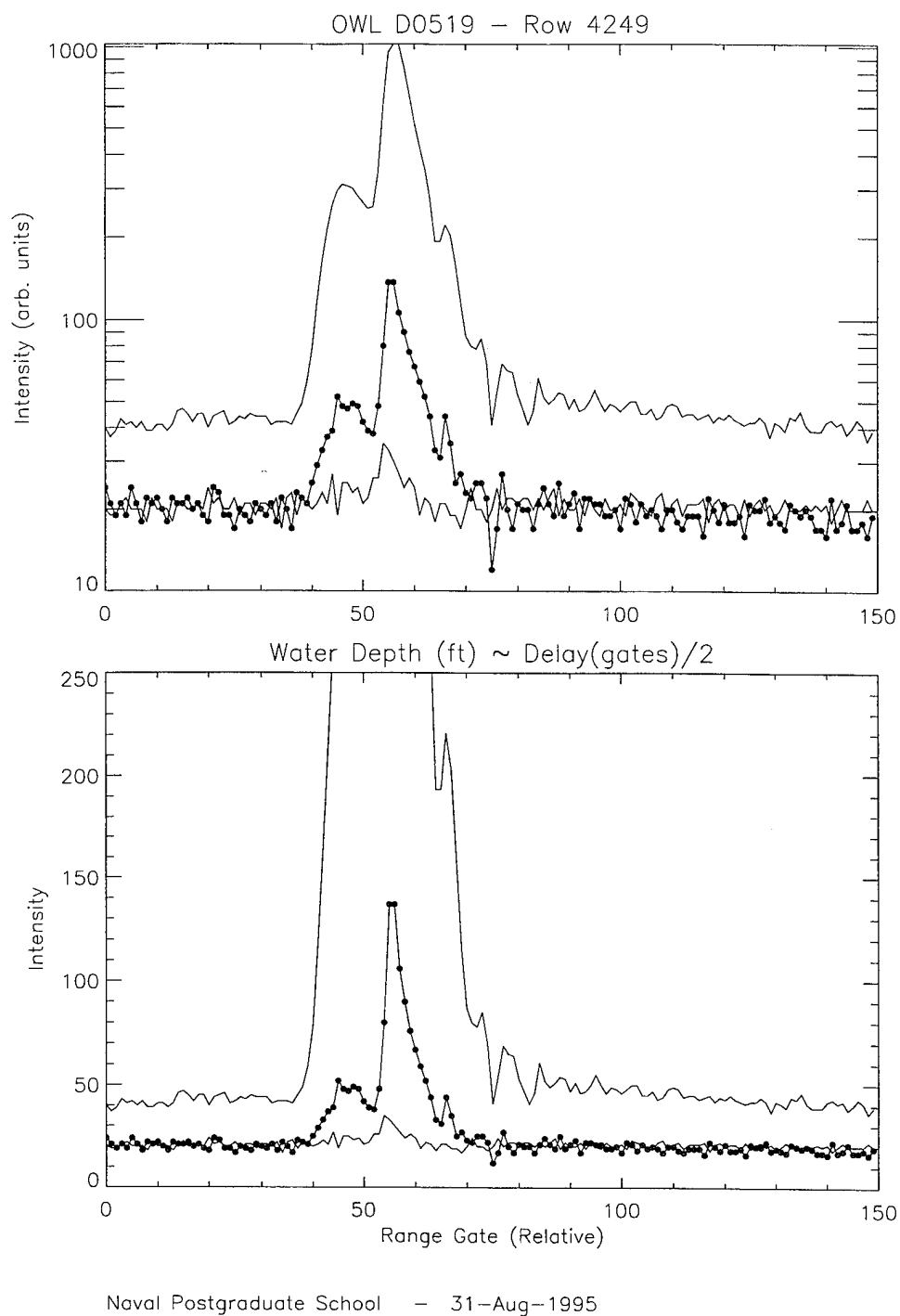
Figure 63: Line plot of row 4249, OWL data set D0519.
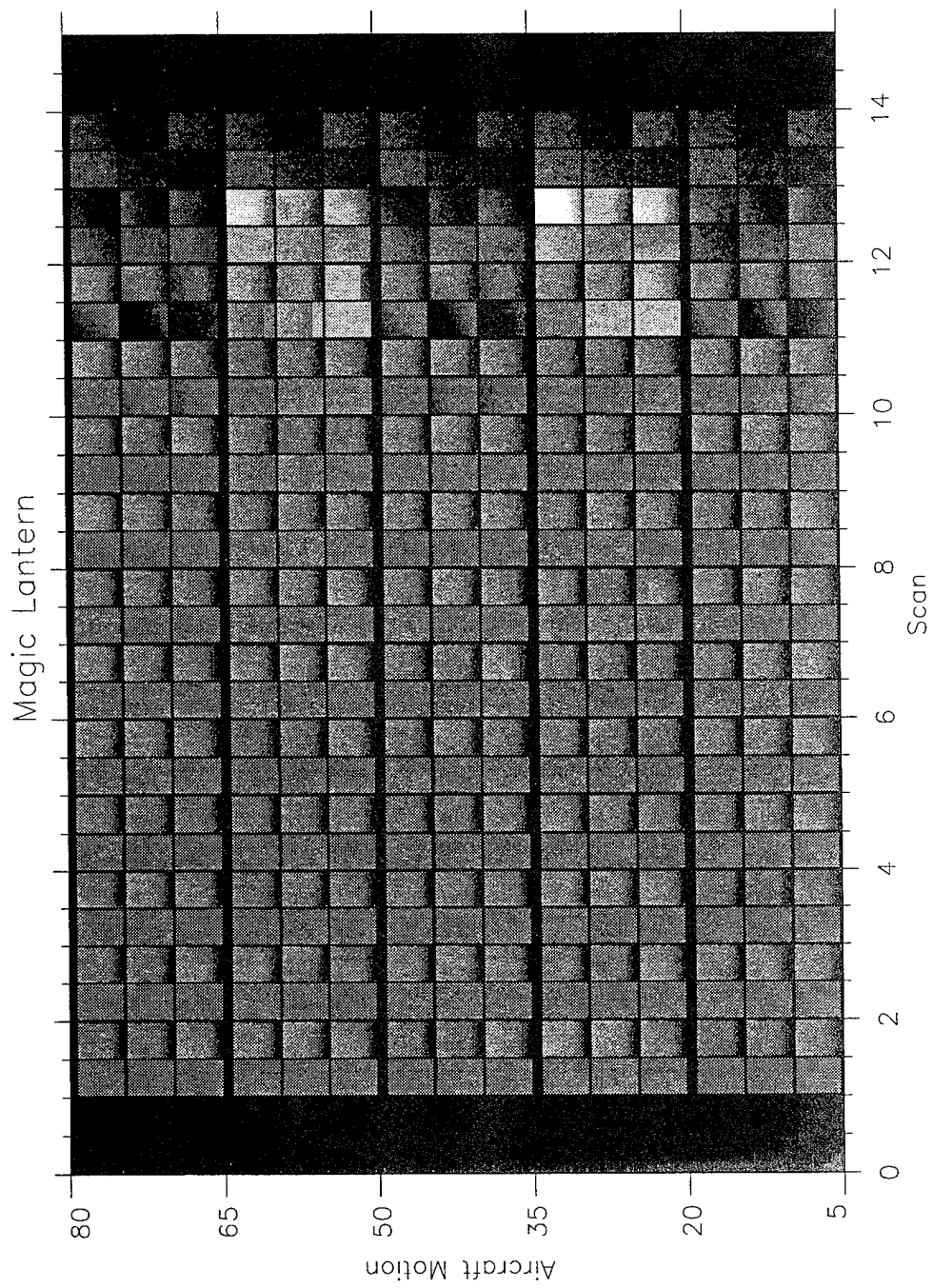
Figure 64: Overview plot of ML(A) scan data.

Magic Lantern
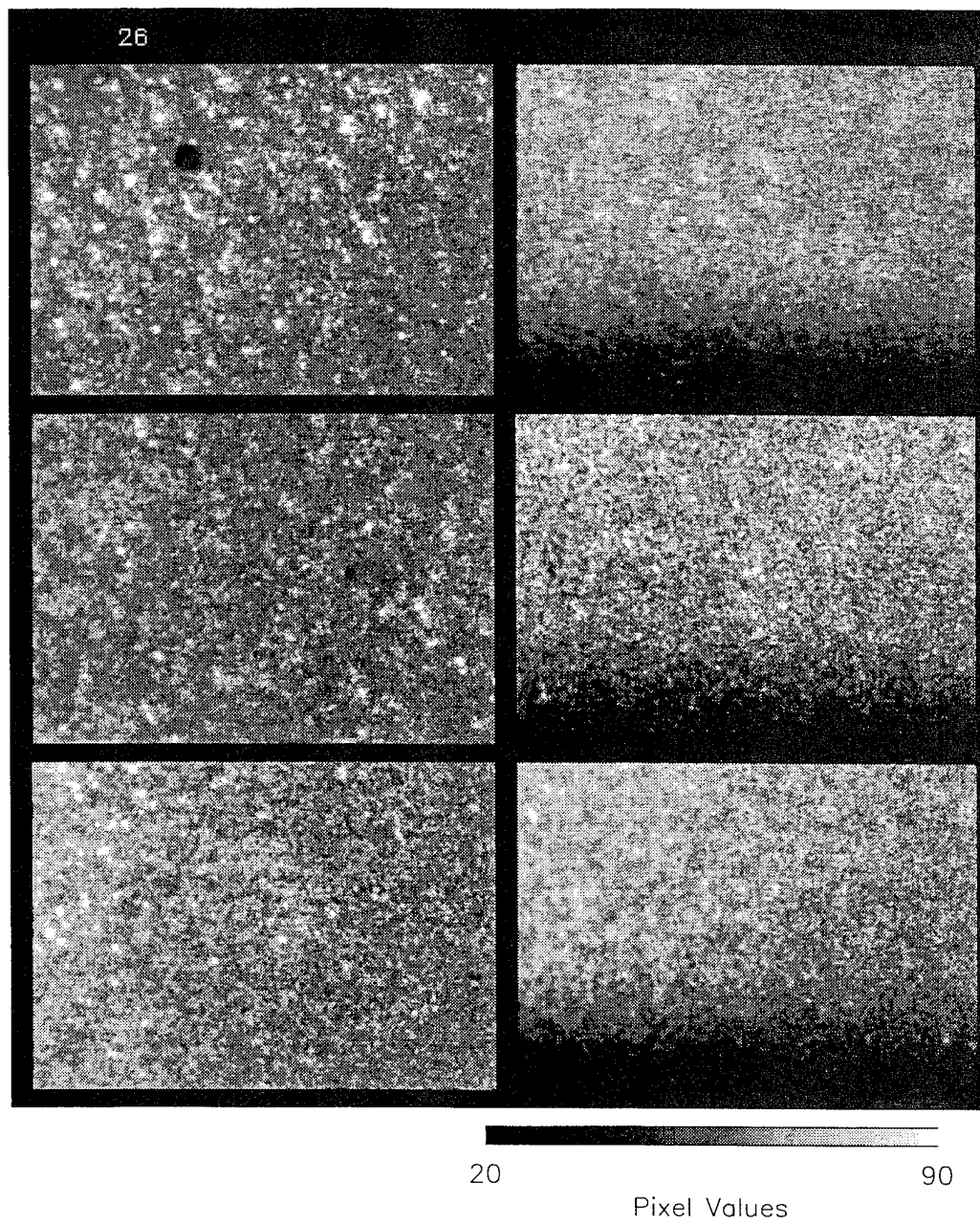
Figure 65: Enlarged plot of six-tiled ML(A) system footprint for scan 26.

133

Magic Lantern

20   90
Pixel Values
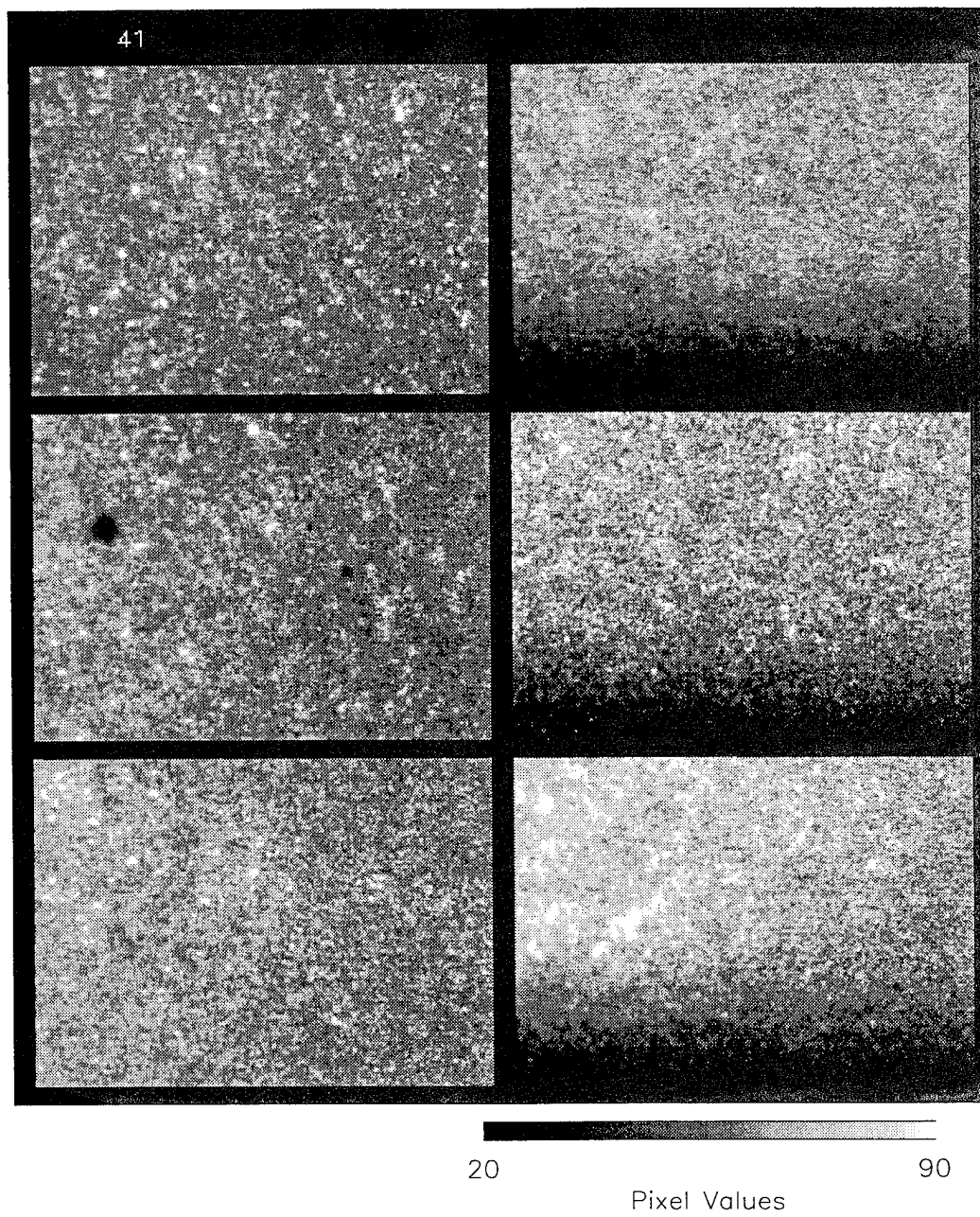
Naval Postgraduate School 1—Sep—1995

Figure 66: Enlarged plot of six-tiled ML(A) system footprint for scan 41.

134

Magic Lantern — Panel 26

Camera 2 — Row 130
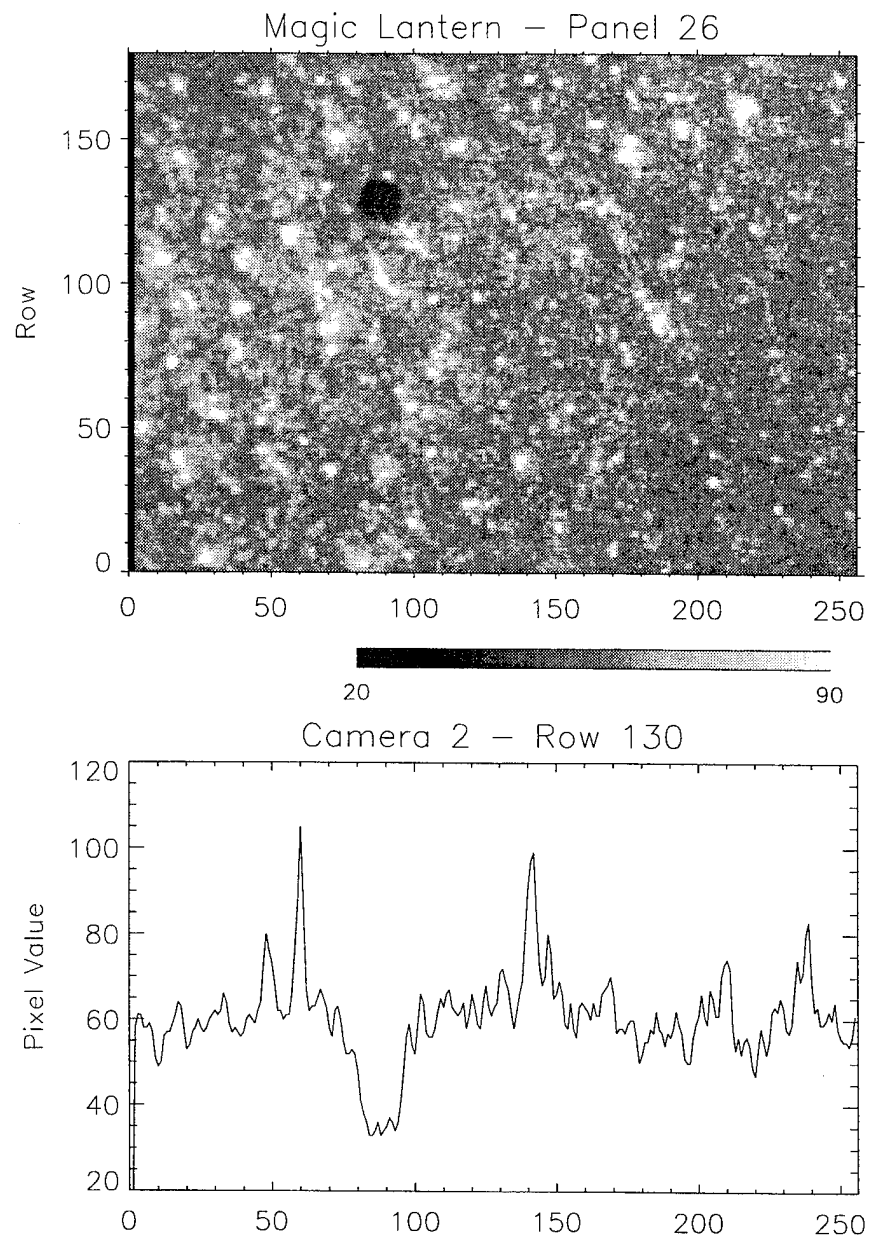
Naval Postgraduate School 1–Sep–1995

Figure 67: ML(A) single camera image and associated line plot for camera two of scan 26.

135

Figure 68: ML(A) single camera image and associated line plot for camera four of scan 41.

LIST OF REFERENCES

Banic, John, and Sebastian Sizgoric, *Scanning Lidar Bathymeter for Water Depth Measurement*, Optech Incorporated, 701 Petrola Road, Downsview, Ontario, Canada M3J 2N6 and Robert O'Neil, Canada Centre for Remote Sensing, Ottawa, Ontario, Canada K1A 0Y7, SPIE Volume 663, Laser Radar Technology and Applications, 1986.
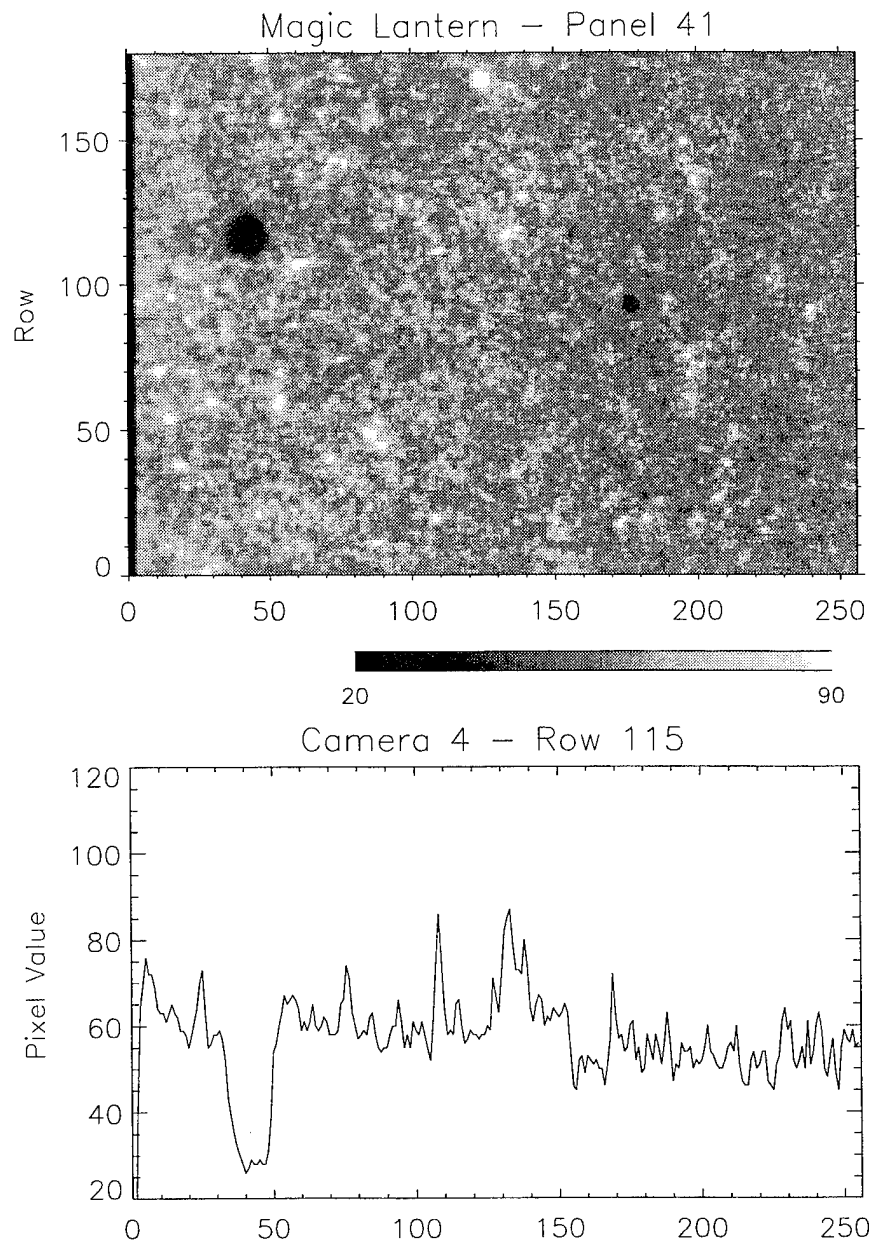
Curran, T., T. Keck, V.M. Contarino (NAVAIRDEVCEN); M.M. Harris, S.P. Haimbach (NORDA), *Digital ABS Laser Sounder Bathymetry*, Naval Air Development Center, Lasers and Magnetics Branch, Code 5012, Warminster, Pennsylvania 18974, Naval Ocean Research Development Activity, Advanced Sensors and Survey Systems, Code 352, NSTL Station, Bay St. Louis, Mississippi 39529, SPIE Volume 925, Ocean Optics, 1988.

Department of the Navy, *Forward...From the Sea*, 1994.

Gibbons, Jack, Mark Hryszko, and Stephen Haimbach, *Hamlet's Cove Ocean Water Lidar Bathymetry Data Report*, Naval Air Warfare Center, Aircraft Division, Code 455610R07, P.O. Box 5152, Warminster, Pennsylvania 18974-0591, Pacific-Sierra Research Corporation, Suite 103, 600 Louis Drive, Warminster, Pennsylvania 18974.

Hecht, Jeff, and Dick Teresi, *Laser: Supertool of the 1980's*, Tickner and Fields, New Haven and New York, 1982.

Janesick, James R., and Morley Blouke, *Scientific Charged-Coupled Devices: Past, Present, and Future*, Optics & Photonics News, April 1995 Volume 6 Number 4, Optical Society of America, 2010 Massachusetts Avenue, N.W., Washington D.C. 20036

Jelalian, Albert V., *Laser Radar Systems*, Artech House, Boston and London, 1992.

Kaman Aerospace Corporation, *ML(A) Concept Review*, 21 July, 1993.

Kaman Aerospace Corporation, *ML(A) Technical Design Review*, 09 September, 1993.

Kaman Aerospace Corporation, *Trainee Guide for the Magic Lantern Advanced Development Model*, 01 June, 1994.

Keeler, R.N., and B.L. Ulich, *Some Aspects of Wide Beam Imaging Lidar Performance*, SPIE Proceedings 2258, Ocean Optics XII, SPIE, Bellingham Washington, Jules Jaffe ed. 1994, p.480.

Kervern, Gilles, and Andre LeGall, *Imaging Through Scattered Media: Performances and Technical Cocerns of Range Gated Equipments*, Thomson Sintra ASM, Route de Ste Anne du Portzic, 29601, Brest, France, SPIE Volume 1714, Lidar For Remote Sensing ,1992.

Kervern, Gilles, and Andre LeGall, and Bernard Toullec, *Airborne Laser Bathymetry: A Novel Technique for Shallow Water Monitoring*, Thomson Sintra Activities Sous-Marines, Route de Sainte Anne du Portzic, 29601, Brest Cedex, France, SPIE Volume 1714, Lidar for Remote Sensing, 1992.

Laurence, Clifford L., *The Laser Book: A New Technolgy of Light*, Prentice Hall Press, New York, 1986.

Pacific-Sierra Research Corporation, *Emerald Airborne Lidar System Description and Calibration*, Naval Air Warfare Center, Aircraft Division, Warminster, Pennsylvania, June 1995.

Shamanaev, Vitalli S., and Margarita M. Krekova, *Effect of the Atmosphere on Signal Shaping in Sea Water Sounding With an on Board Lidar System*, Institue of Atmospheric Optics, Tomsk, Russia, and Georgi M. Krekov, Siberian Medical University, Tomsk, Russia, SPIE Volume 2310, Lidar Techniques for Remote Sensing, 1994.

INITIAL DISTRIBUTION LIST

1. Defense Technical Information Center.. 2
   Cameron Station
   Alexandria, Virginia 22304-6145

2. Library, Code 52... 2
   Naval Postgraduate School
   Monterey, California 93943-5101

3. Prof. R.C. Olsen.. 5
   Physics Department
   Code PH/OS
   Naval Postgraduate School
   833 Dyer Road, Room 104
   Monterey, California 93943-5117

4. Prof. D.L. Walters... 2
   Physics Department
   Code PH/OS
   Naval Postgraduate School
   833 Dyer Road
   Monterey, California 93943-5117

5. Captain William G. Arnold.. 1
   Department of the Navy
   Project Management Office, Mine Warfare
   2531 Jefferson Davis Highway
   Arlington, Virginia 22242-5167

6. Mr. Brett Cordes... 1
   Code 2210
   Coastal Systems Station Dahlgren Division
   Naval Surface Warfare Center
   6703 West Highway 98
   Panama City, Florida 32407-7001

7. Mr. Jack Gibbons... 1
   Naval Air Warfare Center
   Aircraft Division
   Code 455610R07
   P.O. Box 5152
   Warminster, Pennsylvania 18974-0591

8. Dr. Norris Keeler... 1
    Kaman Aerospace Corporation
    1111 Jefferson Davis Highway, Suite 700
    Arlington, Virginia 22202-3225

9. Mr. Mark Yokley.. 1
    Kaman Aerospace Corporation
    3480 East Britannia Drive
    Tucson, Arizona 85706

10. Dr. Stanley Fugimara.. 1
    Pacific-Sierra Research Corporation
    2901 Twenty Eighth Street
    Santa Monica, California 90405

11. Lt. C.J. Cassidy... 1
    5224 South West Tenth Avenue
    Cape Coral, Florida 33914